Transverse Forcing by Acoustic Excitation

for friction drag reduction in a turbulent boundary layer

AE5122: Masters Thesis Project
S.H. Schaafsma

TUDelft

Transverse Forcing by Acoustic Excitation

for friction drag reduction in a turbulent boundary layer

by

S.H. Schaafsma

to obtain the degree of Master of Science

at the Faculty of Aerospace Engineering

of the Delft University of Technology,

to be defended publicly on Friday July 18, 2025

An electronic version of this thesis is available at `http://repository.tudelft.nl/`.

TUDelft

Preface

This document summarises almost a year of research with which I conclude my journey as a student. I learned many things in this process and it was enjoyable to put the knowledge gained over the years to practise.

I would like to thank Dr. Woutijn Baars for sharing his experience in experimental flow control, his many useful insights during our weekly meetings and for explaining how to operate the experimental equipment. I am also grateful for the insights of Dr. Marios Kotsonis, which sparked new ideas and improved the quality of this research.

I also want to thank Emiel Langedijk for his practical knowledge and feedback on my design, and for assisting in the procurement of components. My fellow master thesis students in the Low Speed Laboratory have also provided me with crucial knowledge on topics such as the software used and the pitfalls to avoid.

Finally I would like to acknowledge my friends and family who supported me throughout this period, even though they had to endure my many stories about this research.

S.H. Schaafsma
Delft, June 2025

Abstract

This research investigates the application of acoustic excitation as a novel method for transverse forcing to achieve friction drag reduction in a turbulent boundary layer. Traditional transverse wall motion, while effective in reducing drag, poses experimental challenges due to mechanical complexity and limitations at high Reynolds numbers. This study explores an alternative approach where transverse velocity gradients are induced through oscillatory acoustic fields rather than wall motion. An experimental setup was developed at the Delft University Boundary Layer Facility (DUBLF), incorporating a system of phase-synchronized speakers to generate controlled transverse acoustic forcing. Particle Image Velocimetry (PIV) was used to characterize the boundary layer and assess the effect of forcing across a range of Reynolds numbers. Results show measurable reductions in friction drag, with the optimal configuration achieving up to 6.02% drag reduction at $Re_\tau = 1847$. The study further reveals that the induced transverse velocity fields modulate near-wall turbulence structures, contributing to reduced turbulent kinetic energy and Reynolds stresses. This method provides a mechanically simpler and potentially scalable alternative for active flow control, with the potential to provide new insights into the mechanisms of transverse forcing in turbulent boundary layers.

Contents

List of Figures

List of Tables

List of Abbreviations and Symbols

Abbreviations

Abbreviation	Definition
BL	Boundary Layer characterization
CFD	Computational Fluid Dynamics
DAQ	Data Acquisition
DNS	Direct Numerical Simulation
DUBLF	Delft University Boundary Layer Facility
FoV	Field of View
HWA	Hot-wire Anemometry
int. win.	Interrogation window
LFoV	Large Field of View measurements
PDF	Probability Density Function
PIV	Particle Image Velocimetry
PTU	Pulse Timing Unit
REYN	Constant T^+ and W_m^+ with varying Re_τ run
SPIV	Stereo Particle Image Velocimetry
SS	Speaker synchronization using microphone
StTW	Streamwise Traveling Waves
TKE	Turbulence Kinetic Energy
TS	Thiele-Small
WP	Wall-Parallel measurements

Symbols

Symbol	Definition	Unit
A_{in}	Speaker input amplitude	
B	Log-law constant	4.17
Bl	Product of magnetic flux density and the voice coil gap	[Tm]
c	Speed of sound	[m/s]
C_f	Friction coefficient	
C	TKE Transport equation - Turbulent convection	
C_{ms}	Compliance of speaker suspension	[m/N]
D	TKE Transport equation - Turbulent diffusion	
f	Frequency	[Hz]
f_{DAQ}	Data acquisition frequency	[Hz]
f_{PIV}	PIV capture frequency	[Hz]
f_{plate}	Frequency of plate vibration	[Hz]
f_s	Resonant frequency	[Hz]
k	Turbulence kinetic energy	[m^2/s^2]
M	TKE Transport equation - Mean flow convection	
M_{ms}	Moving mass of speaker	[kg]
N_{im}	Number of PIV image pairs	
P	TKE Transport equation - Production	
p_{act}	Average pressure amplitude over actuator	[Pa]
p_{mic}	Measured pressure by microphone	[Pa]

Symbol	Definition	Unit
P_{req}	Required power	[W]
P_s	Speaker power	[W]
r_{att}	Velocity attenuation rate	
$\mathcal{R}$	Drag reduction	
R_e	Coil DC resistance	[Ω]
Re_τ	Friction Reynolds number	
S_d	Equivalent piston area of speaker	[m^2]
t	Time	[s]
T	Period	[s]
U	Velocity magnitude	[m/s]
U_∞	Freestream velocity	[m/s]
u_i	Velocity component (u, v, w)	[m/s]
u_{act}	Actuator / speaker driver velocity	[m/s]
u_τ	Friction velocity	[m/s]
u_{τ_0}	Reference friction velocity	[m/s]
V	Amplifier input voltage	[V]
W_m	Transverse velocity amplitude	[m/s]
x	Streamwise coordinate	[m]
x_{gap}	Speaker voice coil gap	[m]
x_{max}	Maximum speaker displacement	[m]
y	Wall-normal coordinate	[m]
z	Transverse coordinate	[m]
δ	Boundary layer thickness	[m]
$\Delta\varphi$	Phase offset between speaker driver input signals	
ε	TKE Transport equation - Dissipation	
η_0	Reference efficiency	
κ	Von-Karman constant	0.384
θ	Plate angular deviation	
ν	Kinematic viscosity	[m^2/s]
Π	TKE Transport equation - Pressure transport	
ρ	Density	[kg/m^3]
φ	Phase	
A subscript	Concerning speaker driver A	
B subscript	Concerning speaker driver B	
$+$ superscript	Non-dimensionalised using reference friction velocity u_{τ_0}	
$\langle\cdot\rangle$	Time or phase averaging operator	

1

Introduction

The behaviour of turbulent flow has been an active area of research for hundreds of years [1]. The term 'turbulence' as we now know it was introduced in 1887 by William Thomson [2]. Turbulent flow is chaotic in nature, with a large separation in scales of length and time. This makes it difficult to model and thus to study.

1.1. The importance of drag reduction
The most important topic of research in the aviation industry currently is the reduction of fuel consumption. The importance of reducing CO_2 emissions from air travel is being stressed in the many reports from the Intergovernmental Panel on Climate Change [3]. Aircraft spend most of their time in cruise conditions, therefore, finding ways to reduce drag in cruise conditions is of utmost importance. The drag on a typical modern airplane consists of 55% friction (viscous) drag, 35% lift induced drag and 10% other drag forms [4]. Even a marginal reduction in the friction drag would therefore result in enormous environmental and financial saving globally. Most of the friction drag is on surfaces experiencing turbulent flow.

1.2. Transverse forcing
Fundamental research on the reduction of turbulent friction drag has shown that the drag on a flat plate can be reduced by introducing a transverse oscillating motion of the wall, also described as a transverse forcing of the flow. A definitive explanation on the mechanism behind this drag reduction has yet to be found. The turbulent friction drag reduction has been proven in simulations [5] and experimentally [6]. Both of these methods have their limitations regarding the analysis of the flow. Simulations are generally constricted to low Reynolds Numbers, as their cost increases with the Reynolds number [7]. Experiments are often limited to only a few specific conditions [8] and have difficulties visualizing the flow close to the surface, due to the moving walls. Studies thus far have focussed on canonical flows, such as pipe flow, channel flow and flat plate boundary layer flow.

This research will investigate a novel way of achieving the drag reduction effect on a flat plate turbulent boundary layer flow. The reference frame in which the forcing is applied will be swapped, the transverse velocity gradient will be introduced by means of oscillating the body of air, instead of moving the wall. Changing the reference frame will have several advantages. It reduces mechanical difficulties in replicating the same scaled oscillation conditions at different Reynolds number. It will also result in easier visualisation of the flow, moving walls make the measurement of the spatio-temporal evolution of the flow in the laminar sublayer challenging. This provides a useful tool for future research into the mechanisms behind the drag reduction caused by transverse forcing.

1.3. Research objectives

Extensive analysis of the current body of knowledge in this area has led to the formulation of the following research question:

How can the friction drag reduction in a turbulent boundary layer, from transverse forcing through oscillatory wall motion, be replicated by forcing the flow using acoustic excitation?

Further subdivided into three sub-questions:

1. How can an oscillatory flow field be generated using acoustic excitation?
2. How can the change in friction drag from the forced case be quantified relative to the unforced case?
3. What mechanisms cause the change in friction drag when the flow is forced?

This document describes the answers to the first two sub-questions and an attempt is made to identify the link between the flow control and the friction drag reduction. The document also contains a description of the process leading up to these answers.

1.4. Document structure

This document will start by explaining the background information to this research in Chapter 2. This chapter is divided into three main parts, general information on turbulent boundary layers in Section 2.1, an outline of previous work on transverse forcing in Section 2.2 and background knowledge on acoustics in Section 2.3.

Chapter 3 documents the experiment methodology, from the preliminary calculations in Section 3.1 and the experimental setup in Section 3.2 to the flow measurement techniques used in Section 3.3. The speaker performance was characterized using a test and this is documented in Section 3.4. The experiment procedure is detailed in Section 3.5.

The results of the experimental campaign are discussed in Chapter 4, where first the boundary layer is characterized in Section 4.1. The main results of the experiment are summarised in Section 4.2, and Section 4.3 contains more detail on the effect of the forcing on the flow.

A discussion of the assumptions and shortcomings of this research is found in Chapter 5 and the conclusions are summarised in Chapter 6. The document concludes with recommendations for future research in Chapter 7.

Appendix A contains the test matrices of the experimental campaign and the characterization test. The data processing workflow is outlined in Appendix B and Appendix C contains more results from the Particle Image Velocimetry (PIV) data acquisition. The process of selecting a speaker is documented in Appendix D.

2

Background information

This chapter describes the theoretical framework on which the current work is based. It starts with theory on turbulent boundary layers in Section 2.1, continues with a collection of prior work on transverse forcing in Section 2.2 and concludes with a short summary on acoustics in Section 2.3 with a focus on the current application.

2.1. Turbulent boundary layer theory

Flow along a surface will develop a boundary layer due to viscous losses. This section will consider the boundary layer developing along a flat surface with zero pressure gradient in the streamwise direction. The Reynolds number along the plate is determined using the x-distance from the start of the plate, defined as $Re_x = \frac{xU_\infty}{\nu}$, where U_∞ is the freestream velocity and ν is the kinematic viscosity. Generally, the boundary layer will start with a laminar flow regime. Along the streamwise direction it will lose energy after which it will transition into turbulence. This occurs at the critical Reynolds number $Re_{x_{crit}}$. For zero pressure gradient flow this is generally at $Re_{x_{crit}} = 500.000$ [9]. A schematic overview of the flow along a flat plate is shown in Figure 2.1. Small perturbations are always present in the flow, caused by various sources such as surface discontinuities, curvature or sound, external or generated by the freestream.

In the laminar region, these perturbations are damped by viscous forces and eventually dissipate. In the transition region, the ratio of inertial forces to viscous forces has grown, and this damping effect is suppressed, causing the perturbations to grow and will generally lead to Tollmien-Schlichting waves [10]. These semi-turbulent structures will grow and eventually break down into fully turbulent flow. Transition can occur at lower Re_x if the flow is tripped by instabilities that are large enough, for example from the effects of roughness. The larger instabilities overcome the viscous damping effects.
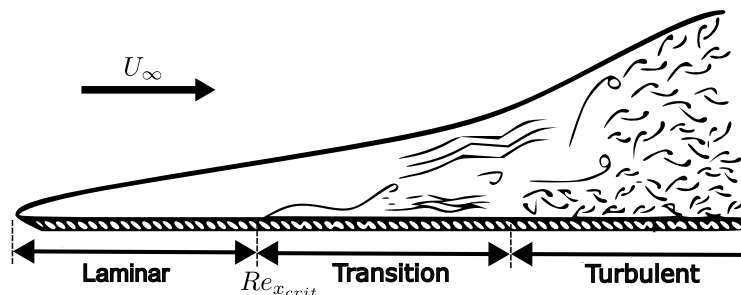
Figure 2.1: Schematic of turbulent boundary layer flow regimes on a flat plate with a zero pressure gradient. The flow starts laminar and at the critical Reynolds number it transitions into turbulence.

3

2.1.1. Friction velocity

The velocity profile of the boundary layer is defined as the mean streamwise velocity $\bar{u}(y)$ with y being the wall-normal axis, as shown in Figure 2.2. The wall-shear stress in the streamwise direction τ_x can be derived from this profile using

$$\tau_x = \mu \left[\frac{\partial \bar{u}}{\partial y} \right]_{y=0} \tag{2.1}$$

where μ is the dynamic viscosity of the fluid. The friction velocity u_τ is defined as $u_\tau = \sqrt{\tau_x/\rho}$ with ρ as the density of the fluid. The friction velocity is often used for non-dimensionalization of scaling parameters [11]. The friction drag coefficient C_f is given by

$$C_f = \frac{\tau_x}{\rho U_\infty^2} = \frac{u_\tau^2}{U_\infty^2} \tag{2.2}$$

Therefore the friction drag on a flat plate can be determined experimentally by measuring U_∞ and $\left[\frac{\partial \bar{u}}{\partial y} \right]_{y=0}$, which can be done in a non-intrusive manner using Particle Image Velocimetry (PIV).

The friction Reynolds number for a turbulent boundary layer is defined as

$$Re_\tau = \frac{u_\tau \delta}{\nu} \tag{2.3}$$

where δ is the boundary layer thickness and $\nu = \mu/\rho$ is the kinematic viscosity. It describes the degree of scale separation between the largest eddies, in the order of δ, to the smallest viscous eddies in the boundary layer. Contrary to Re_x this Reynolds number is not directly dependent on x location, only implicitly through u_τ and δ which are a function of x.

2.1.2. Layers of the turbulent boundary layer

The turbulent boundary layer is built up from three distinct layers, the viscous sublayer, the overlap layer and the wake region [11]. Each of these layers have distinct flow features and they interact with each other through mixing. A schematic of all the layers is shown in Figure 2.2.

Viscous sublayer

The viscous sublayer, also named inner layer or near-wall region, is the region that is closest to the wall and is influenced by it. This layer's border is defined by $y^+ \leq 350$, with $y^+ = u_\tau y/\nu$ the non-dimensionalized wall-normal distance. This layer is bounded by an upper limit that scales in viscous units. Right up to the wall there is the laminar sublayer, in this very thin zone, $y^+ \leq 5$, the wall influence is the greatest and here the flow behaves essentially laminar. The velocity profile is linear, $u^+ = y^+$, with $u^+ = u/u_\tau$ the non-dimensionalized streamwise velocity. Above this is the buffer zone where $5 \leq y^+ \leq 30$, here the flow still has laminar properties but the influence of turbulence is getting noticeable. After this the laminar properties are lost as the freestream turbulence effects increase in strength. The presence of the wall does effect the whole of the viscous sublayer. The flow in the buffer zone can not be analytically described as it has properties of both the laminar sublayer and the overlap layer.

Overlap layer

The overlap layer encompasses the transition from the viscous sublayer into the wake region. The borders of this layer are not exactly defined but it is generally taken as the region between $y^+ = 100$ and $y/\delta = 0.15$. It has properties of both the viscous sublayer and the wake region and is also called the logarithmic region because the mean velocity profile is logarithmic. This profile is given by

$$u^+ = \frac{1}{\kappa} \log y^+ + B \tag{2.4}$$

with κ as the Von-Karman constant and B is a constant. In this research the values $\kappa = 0.384$ and $B = 4.17$ are used as these are suitable for boundary layer flows [12].

Wake region

In the wake region the effect of the freestream turbulence dominates and the presence of the wall is negligible. The flow structures are chaotic in nature. This layer is also called the outer layer and the profile is determined by the flow outside of the boundary layer.
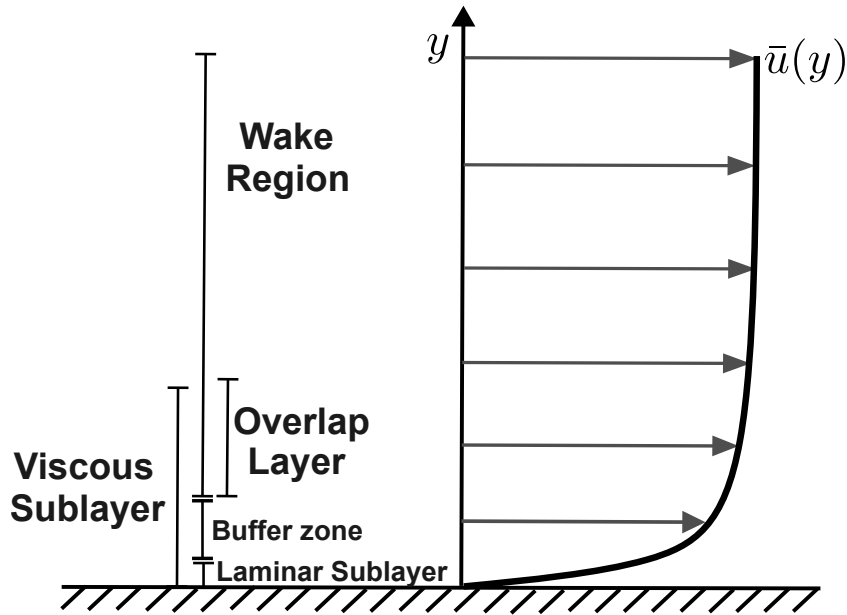
Figure 2.2: Schematic of the layers within the turbulent boundary layer.

2.1.3. Thickness metrics

The turbulent boundary layer thickness can be described using different metrics. The most commonly known one is the 99% rule, defined as the height from the surface where the average streamwise velocity is equal to $0.99U_\infty$, denoted by δ_{99}. Long measurement times are needed to get a velocity profile converged enough to determine δ_{99} accurately, because of the large time scales of the turbulent structures in the wake region. Therefore the integral metrics are more reliable.

One of these integral metrics is using the boundary layer displacement thickness. This metric is calculated by measuring the distance the streamlines in the freestream are displaced by the boundary layer. A prerequisite for this method is that the streamlines of the undisturbed flow are known, which is trivial for the flat surface case.

The boundary layer momentum thickness δ_2 describes the loss of momentum from the boundary layer when compared to an equivalent inviscid flow. It is calculated using

$$\delta_2 = \int_0^\infty \frac{u}{U_\infty}\left(1 - \frac{u}{U_\infty}\right)dy \tag{2.5}$$

It can be calculated for every incompressible boundary layer. Using a control volume the drag on a flat plate can be calculated from δ_2 using

$$D = \rho U_\infty^2 \delta_2 \tag{2.6}$$

Therefore C_f is directly related to δ_2. However, experimentally determining C_f in this manner has a large accumulation of uncertainties.

2.2. Transverse forcing

Transverse forcing is a type of flow control where a flow with a turbulent boundary layer is forced in the transverse direction in an oscillatory manner. The aim of this control is to reduce the friction drag on the surface. Transverse forcing has been studied in pipe flows, channel flows and flat plate boundary layers. All research mentioned focusses on smooth surfaces, without the effects of roughness.

The performance of a transverse forcing flow control method is usually quantified using the drag reduction $\mathcal{R}$, which is a ratio between the friction drag in the uncontrolled case and the controlled case. Another metric is the Net Power Saving (NPS). This subtracts the required input power from the power saved by the drag reduction. For active methods, such as the current research, it is generally challenging to achieve a positive NPS, only in ideal circumstances and neglecting all mechanical and electrical

losses. The main purpose of these studies is therefore not to achieve positive NPS, but to understand the mechanisms behind the drag reduction.

Section 2.2.1 will introduce the concept of Streamwise Traveling Waves of transverse wall velocity, which is a general description of this type of flow control. Section 2.2.2 and 2.2.3 describe the two extreme cases of these waves. The various conjectures on the underlying aerodynamic mechanism are summarised in Section 2.2.4, a collection of high Reynolds number studies is discussed in Section 2.2.5, the streamwise development of the drag reduction is detailed in Section 2.2.6 and finally Section 2.2.7 outlines the research gap that is the basis of the current research.

2.2.1. Streamwise traveling waves of transverse wall velocity

Quadrio et al. [13] introduced the concept of Streamwise Traveling Waves (StTW) of transverse wall velocity. These waves can be described by

$$w_w(x,t) = W_m \sin(\kappa_x - \omega t) \tag{2.7}$$

where w_w is the local transverse velocity of the wall, W_m is the peak velocity, κ_x is the wave number, ω is the frequency, x is the streamwise coordinate and t is the time. Figure 2.3 shows a schematic of a StTW.

The drag reduction is usually defined as

$$\mathcal{R} = 1 - \frac{C_f}{C_{f_0}} \tag{2.8}$$

with C_f the friction coefficient in the forced case and C_{f_0} the friction coefficient in the base flow [15]. The friction coefficient is defined as $C_f = 2\tau_x/(\rho U_\infty^2)$ with τ_x the streamwise wall shear stress, ρ the density and U_∞ the freestream velocity. This makes C_f, and thus the drag reduction, inherently Reynolds number dependent.

All Direct Numerical Simulation (DNS) flows considered in this section are fully developed internal flows with a turbulent boundary layer developing at the domain edge. The flow can be described using the friction Reynolds number, Re_τ. This completes the parameter space that encompasses the drag reduction problem, described by

$$\mathcal{R} = f\{W_m, \kappa_x, \omega; Re_\tau\} \tag{2.9}$$

For open boundary layer flows there is also a dependency in x, however, this is assumed as negligible as only a small streamwise section is considered. This gives a large space of possible combinations. Gatti and Quadrio [16] ran DNS covering a large parameter space, at low Re_τ. They found that drag is reduced for part of the domain, there are also combinations of input parameters that see a drag increase.

The main problem with DNS is that simulations get very expensive for higher Re [7]. It is therefore difficult to predict the drag reduction potential for flows with a practical Re. Gatti et al. [14] conducted DNS at higher Re_τ using a smaller domain to reduce simulation cost. They show that the $\mathcal{R}$ is reducing monotonically with increasing Re_τ up to $Re_{\tau_0} = 6000$.

2.2.2. Steady waves

A special case of StTW of transverse wall velocity occurs when $\omega = 0$. This gives a steady, standing wave of transverse wall velocity. The equation for the wall velocity reduces to

$$w_w(x) = W_m \sin(\kappa_x x) \tag{2.10}$$

Skote [17] shows in a DNS study using purely spatial forcing a drag reduction up to 50%. The drag reduction is reported to be at its maximum where the wall velocity is greatest. However, more power is required to drive the forcing than the power gained through drag reduction. Yakeno et al. [18] used DNS to investigate the effect of κ_x on the drag reduction. They performed various simulations at $Re_\tau = 150$ and their results are shown in Figure 2.4. They found an optimal wavelength $\lambda_x^+ = 1000$, which relates to the wavenumber with $\lambda_x^+ = \frac{2\pi}{\kappa_x^+}$. If converted using the typical convection velocity this results in a period $T^+ = 100$, which corresponds to the optimal value found by Quadrio et al. [5] for spatially uniform
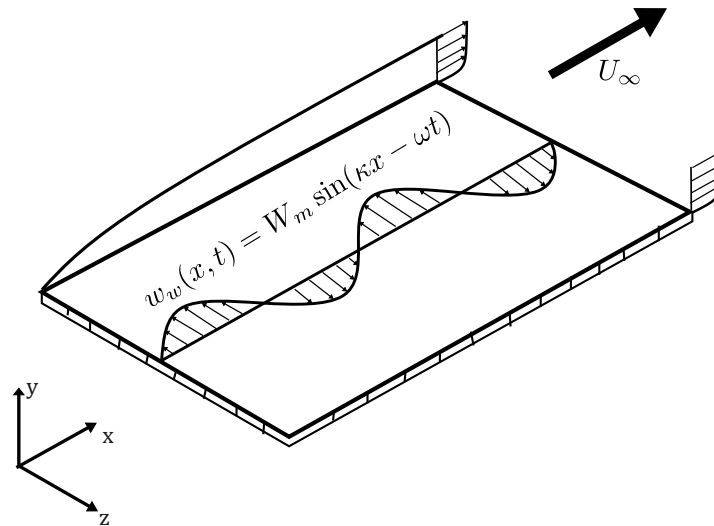
Figure 2.3: Schematic of a Streamwise Traveling Wave of transverse wall velocity. Based on Figure 1 of [14].

forcing, described in Section 2.2.3. In the same study they investigated spatially uniform forcing and they concluded that steady forcing is more effective.

Other waveforms than pure sine waves have also shown potential for drag reduction. Square waves have been shown to reduce friction drag [19]. Mishra and Skote [20] propose to use a half-wave, saving power on driving the actuators. They found a net energy saving of 18% at the optimal oscillation parameter. Square waves have also been investigated experimentally. Knoop et al. [21] realized this waveform by using a series of running belts in the transverse direction. They found a drag reduction of up to 20% with a positive trend with increasing wave amplitude.

2.2.3. Spatially uniform waves
Another special case of StTW of transverse wall velocity is with $\kappa_x = 0$. The equation for the wall velocity reduces to

$$w_w(t) = W_m \sin(\omega t) \tag{2.11}$$

Here the wall moves as a single entity and thus there is no variation in forcing velocity along the streamwise direction at a single time instant.

Early DNS research performed by Jung et al. [22] in 1992 showed that the oscillating wall could reduce the turbulent friction drag by 10% to 40%, with a $T^+ = 100$ as the optimal oscillation period. This corresponded to a reduction in turbulence intensity and the Reynolds shear stress. They compared moving the wall to inducing an oscillating cross-flow with a transverse pressure gradient and the results were the same. Most DNS research is conducted using a channel flow with a symmetry imposed on the centerline [23]. Skote et al. [24] did 3 simulations at different Reynolds number of a true boundary layer flow. These simulations are more expensive than symmetric channel flows since the domain height must be greater. The domain length is also usually larger for boundary layer flows, as the channel flow can reuse the outflow for its inflow with a periodic boundary condition, boundary layer flows grow and therefore this is not as trivial. One of the simulations replicated an experiment by Ricco and Wu [25] and showed nearly identical results.

There have been multiple instances of experimental research into the spatially uniform wave as this case of StTW is the least complex. Laadhari et al. [6] constructed an oscillating wall on bearing slides driven by a crankshaft system. This fixed the motion amplitude while the period could still be changed. They reported a reduction in turbulence but did not measure the effect on friction drag. Choi et al. [8] sought to confirm the results of DNS studies performed earlier. They found friction drag reduction of up to 45% with their experimental setup. They measured the boundary layer profile using Hot-Wire
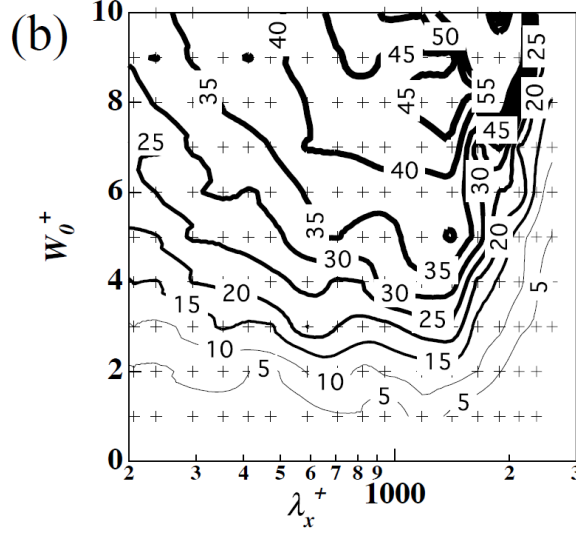
Figure 2.4: Drag reduction as a function of wavelength $\lambda_x^+ = \frac{2\pi}{\kappa^+}$ and amplitude ($W_0^+ = W_m^+$), taken from Yakeno et al. [18]

Anemometry (HWA) and visualised the flow using smoke. They conclude that the mechanism of the drag reduction is strongly related to the transverse vorticity generated by the periodic Stokes Layer induced by the oscillation. In a more recent study Kempaiah et al. [26] analysed the flow behaviour at the oscillating wall using 3-dimensional PIV at $Re_\tau = 570$. They found a maximum drag reduction of 15% together with a significant reduction of turbulent stresses. They hypothesize that the observed drag reduction is a result of the reduction of the number of hairpin vortices when the wall is oscillated. A common problem in most experimental setups is that the amplitude of the motion is fixed, and thus W_m^+ can not be chosen independently from T^+. This limits the part of the parameter space that each experiment can investigate.

Gouder et al. [27] use an actuator based on electroactive polymers. Their setup features a plate on an air bearing for minimal friction. Their method of actuation allows them to vary the amplitude of the oscillation, for a fixed period. They measured drag reduction of up to 16% using HWA and Particle Image Velocimetry (PIV).

Skote [28] compared forcing using steady waves to spatially uniform waves with DNS. Steady wave simulations were performed that matched the scaling parameters of earlier spatially uniform wave simulations. It was found that steady waves give a higher drag reduction for the same conditions. This corresponds to a higher energy saving.

Scaling parameters
Spatially uniform waves can entirely be characterized by their amplitude W_m and frequency ω or period $T = 2\pi/\omega$. These parameters can be non-dimensionalized using the reference, unforced wall units, indicated with the $+$ superscript. This gives $W_m^+ = W_m/u_{\tau_0}$ and $T^+ = Tu_{\tau_0}^2/\nu$, with u_{τ_0} the friction velocity in the base flow and ν is the kinematic viscosity [13]. Another scaling method is using the actual friction velocity u_τ. This is denoted with the $*$ superscript and gives $W_m^* = W_m/u_\tau$ and $T^* = Tu_\tau^2/\nu$ [29]. It is important to choose the correct scaling method for the case under consideration as it can introduce unintended Re_τ effects [16].

The non-dimensional acceleration of the wave, defined as $a^+ = W_m^+/T^+$ was proposed as a scaling parameter by Ding et al. [30]. They argue that the functional relationship of $\mathcal{R}$ as indicated in Equation 2.9 reduces to

$$\mathcal{R} = g(a^+) \tag{2.12}$$

for higher Re_τ and thus has a much simpler parameter space. Their experiment data collapses onto itself when plotted on a $a^+ - \mathcal{R}$ graph. These experiments are using pipe flow with $1356 \le Re_\tau \le 6851$ and an oscillating section as the test case. A review of simulation data of channel and boundary layer

flows at $Re_\tau \approx 1000$ and $Re_\tau \approx 2000$ from various sources [31, 32, 33, 27, 14] does not convincingly show this collapse, see Figure 2.5.

Reynolds number dependence

Most DNS studies are performed at low Re_τ because the cost of the simulation is proportional to this number, generally with $Re_\tau < 2000$. Typical values for Re_τ in practical applications are 4000 on a wind-turbine blade, 6000 mid-span on a Boeing 787 wing and 10.000 to 100.000 along a Boeing 787 fuselage during cruise [34]. It is therefore important to investigate the effect of Re_τ on the drag reduction to predict the feasibility of real world applications.

There have been multiple studies about the Re_τ effect, the general consensus is that the drag reduction decreases for higher Re_τ. These studies do not agree on how much it decreases. Yao et al. [33] summarizes a number of these studies into the Re_τ effect, their results shown in Figure 2.6.

From this summary it seems that the drag reduction has a logarithmic relation to Re_τ. There is a large spread between the studies investigated however.

Gatti et al. [14] argue that the main effect of the StTW is to change the additive constant ΔB^* in the logarithmic law for the mean velocity profile

$$u^*(y^*) = \frac{1}{k} \ln y^* + B_0^* + \Delta B^* \tag{2.13}$$

with B_0^* as the additive constant in the reference unforced flow and $B^* = B_0^* + \Delta B^*$ is the additive constant in the forced case. They performed DNS studies up to $Re_\tau = 6000$ to investigate the Re_τ effect. The data is used to confirm the GQ-model, proposed by Gatti and Quadrio [16]. The GQ-model is given by

$$\Delta B^* = \sqrt{\frac{2}{C_{f_0}}} \left((1 - \mathcal{R})^{-1/2} - 1 \right) - \frac{1}{2k} \ln(1 - \mathcal{R}) \tag{2.14}$$

with k as the von Kármán constant, C_{f_0} as the friction coefficient in the unforced case and $\mathcal{R}$ as the drag reduction. The DNS simulations showed a similar trend as predicted by the model, which gives a monotonically decreasing drag reduction rate.

Marusic et al. [34] did an experimental study where a StTW was discretized into finite length segments, each having their own oscillating wall section. Their experiment went up to $Re_\tau = 12800$ and they found that for $T^+ \approx 100$ their results followed the GQ-model when compared to Large-Eddy Simulations (LES) for the lower Re_τ. Oscillation in the $T^+ = 100$ region is targeted at the near-wall streaks, which have a similar period. They argue that for higher Re_τ it is more beneficial to target larger eddies higher up in the boundary layer, which have a larger period. For $T^+ > 350$ they found a lower drag reduction but with an upwards Re_τ trend, and the lower oscillation frequency resulted in a positive Net Power Saving (NPS). It must be noted that the amplitude of oscillation increased from $W_m^+ = 4.6$ at $Re_\tau = 9000$ to $W_m^+ = 5.7$ at $Re_\tau = 12800$ due to physical constraints of the actuator [14]. This could be the reason behind the increasing drag reduction trend.

2.2.4. Flow mechanisms

Currently there is no generally accepted physical mechanism behind the drag reduction observed when applying transverse forcing. Various studies have been performed on the subject, most focus on the turbulence statistics and how they change when subjected to transverse forcing. Others are focussed on the instantaneous flow features and their development. Six conjectures that attempt to explain the drag reduction mechanism from these studies are covered in this section, some of these support each other, while others conflict [23].

Reduced turbulence production

The wall oscillation has an effect on the transport equation for the streamwise Reynolds stress $\overline{uu}$. The turbulence production in the buffer layer is reduced greatly. As is the dissipation in the viscous sublayer is directly linked to the energy budget created by the turbulence production, this is also reduced [31]. The transverse forcing also reduces the pressure-velocity term. While this is a minor contributor in the viscous sublayer, a reduction of up to 75% was seen by Touber and Leschziner [31]. The reduction of
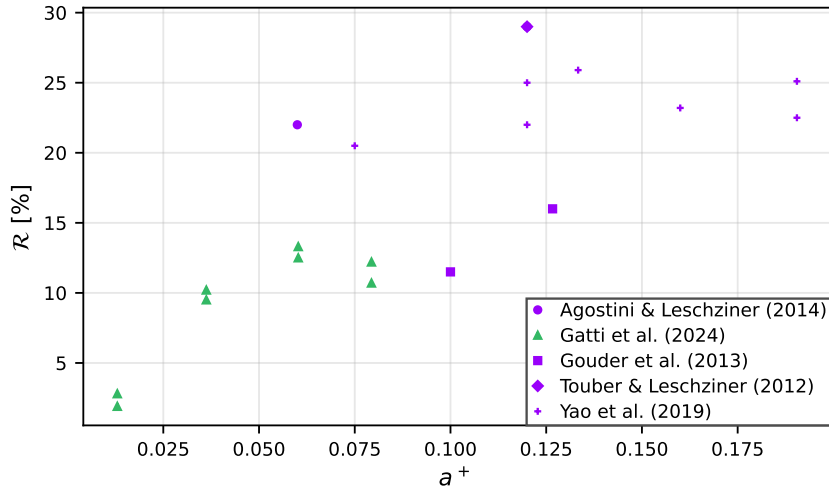
Figure 2.5: High Re_τ simulation and experimental data from various sources, scaled using non-dimensional acceleration. Green icons correspond to $Re_\tau \approx 1000$, purple icons to $Re_\tau \approx 2000$.

this term in the outer region results in a decline of turbulent diffusion, which transports energy from the wake region into the viscous sublayer. This is confirmed by simulation data from Touber and Leschziner [31], shown in Figure 2.7. The causality of this theory is still under debate, it is unclear if the observed reduction in turbulence production is the cause of the drag reduction or the other way around.

Rising dissipation

Ricco et al. [37] conducted a DNS study where they investigated the turbulent energy budget. The use of a constant pressure gradient caused the mass flow to increase with reduced drag, giving uniquely defined inner scaling.

The energy spend to drive the wall motion coincided to the viscous dissipation due to the oscillating transverse layer. The increased energy intake due to the higher mass flow rate is balanced by the increase in dissipation, both the dissipation caused by the mean streamwise velocity profile and the turbulent dissipation. This led them to conclude that an increase in dissipation is the driving factor behind the drag reduction mechanism.

Agostini et al. [32] argue that the variation in Reynolds stresses are caused mainly by the fluctuations in turbulence production which are balanced by the pressure-velocity interaction, with the dissipation being of less importance. This leads to the conclusion that an increase in dissipation is not the driving force behind the drag reduction, but rather the decrease in turbulence production, this is shown in Figure 2.8.

Interactions with the turbulent enstrophy components

Agostini and Leschziner [32] found in their DNS study of a turbulent channel flow that the turbulent enstrophy tensor experiences only modest variation across the phase. However, its components $\overline{w_i w_j}$ showed substantial deviations and phase shifts. A more recent channel flow DNS study by Yuan et al. [38] complements this by saying that the components in the wall-normal $\overline{w_y w_y}$ and transverse $w_z w_z$ direction showed a phase shift of a quarter of an actuation period . Their respective production rates had the same effect. This causes a tilting of the wall-normal vorticity in the transverse direction increasing the skewness near the wall, resulting in a reduction of the wall-normal vorticity, which in turn reduces the strength of the near-wall streaks, Agostini et al. [39] concluded.

Hysteresis effect

During one actuaction cycle the induced transverse Stokes layer has an opposite vorticity sign in each half of the cycle. When the Stokes layer has the same sign as the quasi-streamwise vortices in the outer layer high speed flow under the vortices is pulled towards the wall. In the other half of the actuation there is low speed flow being dragged towards the wall. However, because the sign of the vorticity between
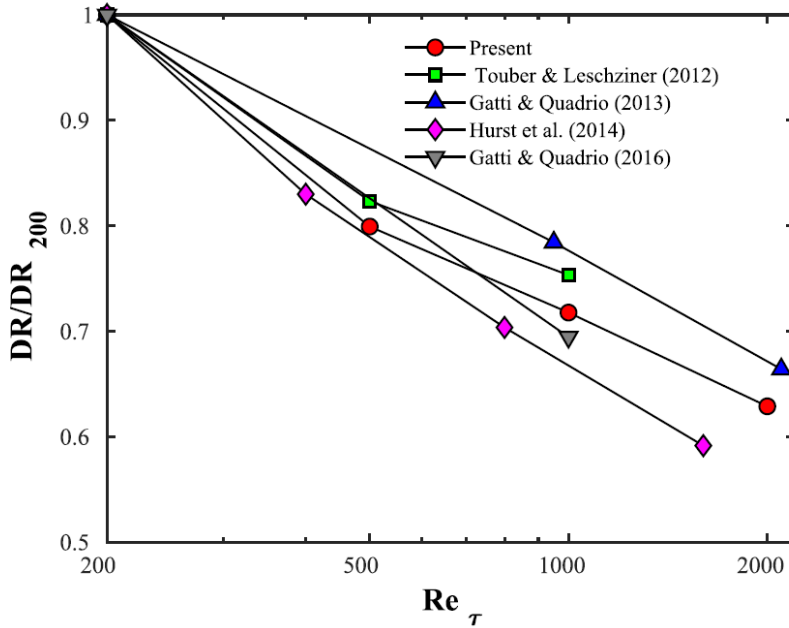
Figure 2.6: Drag reduction versus Re_τ from various sources, scaled with the result from the $Re_\tau = 200$ case. Oscillation amplitude $W_m^+ = 12$ for all cases, oscillation period is $T^+ = 100$ for the present case, Touber and Leschziner [31] and Gatti and Quadrio [16], $T^+ = 90$ for Gatti and Quadrio [35] and $T^+ \approx 105$ for Hurst et al. [36]. Taken from Yao et al.[33].

the Stokes layer and the quasi-streamwise vortices now is opposite, this effect is less pronounced. This inherent assymmetry results in a net drag reduction [40].

However, for every quasi-streamwise vortex with a certain sign there should be another with the opposite sign, it is therefore not entirely clear why this should give a drag reduction [23].

Velocity skewness, the wall-normal gradient of the velocity vector direction, is proposed by Agostini et al. [32] as a driving factor in the damping of the near-wall streaks in the viscous sublayer. They ran a DNS study on a flow with $Re_\tau = 1000$ with sub-optimal period $T^+ = 200$. This resulted in a part of the oscillation phase reducing drag and another part increasing the drag. A phase-wise asymmetry in the skewness is proposed as the cause of hysteresis in the drag altering mechanisms, resulting in the drag-reducing condition taking up a greater part of the actuation cycle. This is caused by the time scale of the streaks reforming being $t^+ \approx 50$, which also explains why a $T^+ \approx 100$ gives the optimal drag reduction. Their results are shown in Figure 2.9, confirming this theory.

Reduction of sweep and ejection events
The numerical results of Touber and Leschziner [31] show that there is a significant reduction in wall-normal stresses when forcing is applied at the optimum period. This reduction is up to 80% in the viscous sublayer, shown in Figure 2.10. The wall-normal stress is also responsible for the production of near-wall Reynolds shear stresses $\overline{uv}$, which then also reduces along with the drag [38]. This indicates that the ejection and sweep events near the wall are significantly damped. This damping is somewhat weaker than the damping of the low-speed streaks and the quasi-streamwise vortices [23]. This indicates that the drag reduction mechanism is more complex than the simple damping of all near-wall structures. Quadrio and Ricco [41] even report a slight increase in the quasi-streamwise vorticity.

Hairpin vortices form near the wall in a turbulent boundary layer due to the interaction between the low-speed streaks and the surrounding flow. These hairpins contribute to the sweep and ejection events, increasing turbulence intensity. Gouder et al. [42] theorize that hairpins form in packets, which in turn trigger the auto-generation of more hairpin vortices. A reduction in hairpin formation therefore escalates and requires the remaining hairpin vortices to be stronger to trigger auto-generation. The formation of these packets is reduced by the transverse forcing. Kempaiah et al. [26] state that the packets form
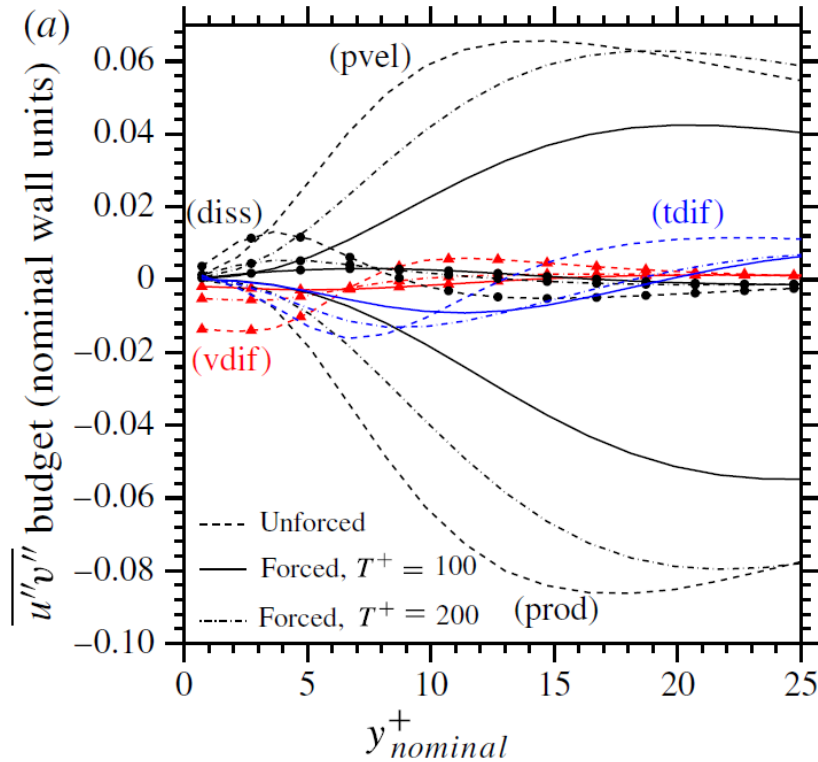
Figure 2.7: Second-moment turbulence budget with (tdif) turbulent diffusion, (pvel) pressure-velocity interaction, (prod) turbulence production, (diss) dissipation and (vdif) viscous diffusion, taken from [31]

because the low-speed streaks have sufficient streamwise length for multiple hairpin vortices. The rapid lateral shift introduced by the forcing shears the low-speed streak, disturbing the alignment and interaction between the downstream hairpins. This results in more isolated hairpin vortices, with less ejection of low-speed fluid and therefore a reduction in skin-friction drag.

Vortical near-wall motions

In a turbulent boundary layer near-wall streaks of vorticity form that extend in the streamwise direction. These interact with the quasi-streamwise vortices in the outer layer. When introducing a transverse flow the streaks move relatively to the vortices, which causes interaction between these mechanisms is disturbed, weakening the streaks [43].

Baron and Quadrio [44] argue that the Stokes layer will always have as many streaks as possible without displacing the quasi-streamwise vortices. Based on this they estimated the optimal oscillation period to be $T^+ \approx 100$ using the laminar-flow solution given by Stokes [45]:

$$w(y,t) = W_m e^{-y\sqrt{\pi/\nu T}} \cos\left(\frac{2\pi t}{T} - y\sqrt{\frac{\pi}{\nu T}}\right) \tag{2.15}$$

For this optimal period the unsteady transverse Stokes layer has a thickness of $y^+ \approx 15 - 20$, which coincides to the thickness of the viscous sublayer. If T^+ is increased further the Stokes layer will continue into the buffer layer and the wake region. Here it will increase the turbulent production, which has a negative impact on the friction drag. This optimal period was confirmed using DNS studies by Quadrio [41]

Akhavan et al. [46] explain the displacement and the subsequent broken interaction of the near-wall streaks due to the oscillating flow using a pressure gradient in the transverse direction. However, later research, including Baron and Quadrio [44] say the streaks are displaced due to the transverse shear stress as a result of the wall motion. Jimenez and Pinelli [47] performed a DNS study where they
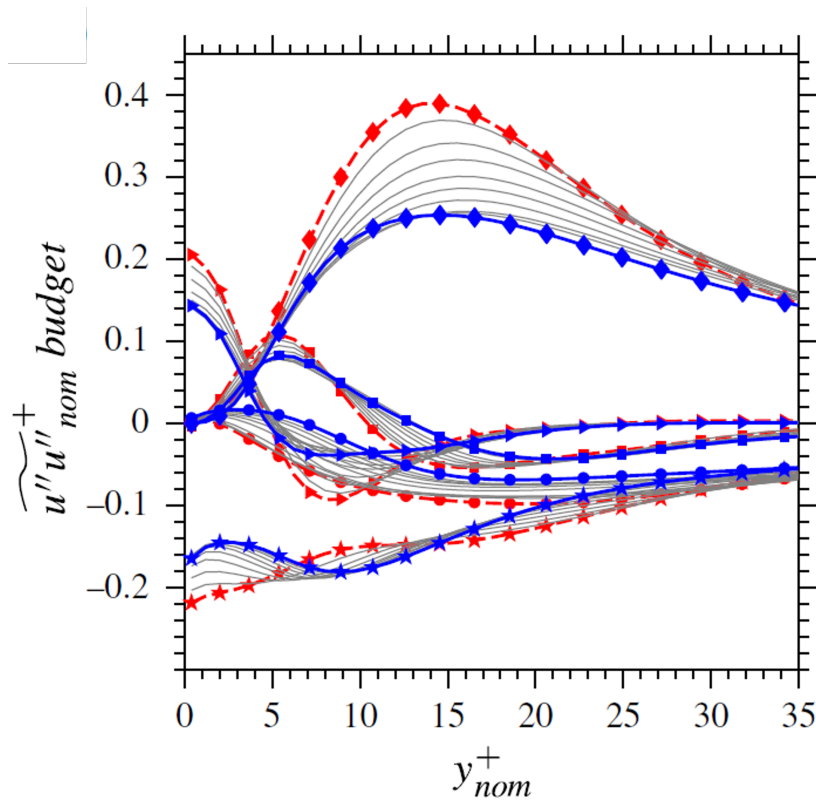
Figure 2.8: Second-moment turbulence budget contributions taken from the drag-reduced state in the simulation ran by Agostini et al. [32]. The red lines correspond to the maximum skin-friction value, the blue lines to the minimum skin-friction value, the thin lines correspond to the intermediate values. With ■ turbulent diffusion, ● pressure-velocity interaction, ◆ production, ★ dissipation and ▲ viscous diffusion.

oscillated the viscous sublayer using body forces, which removes the Stokes layer. They observed a decrease in streak vorticity due to the reduced interaction with the quasi-streamwise vortices.

This displacement results in a rotation on the vorticity vector at both sides of the actuation. This rotation gives a net reduction in the mean transverse vorticity, this is illustrated in Figure 2.11. The mean transverse vorticity induces drag through the downwash of high-momentum flow towards the surface, causing friction drag. A reduction of this vorticity thus causes a reduction in drag [40].

2.2.5. High Reynolds cases
Using experimental methods to investigate the effects on turbulent boundary layers will naturally lead to higher friction Reynolds number Re_τ compared to DNS simulations. The Delft University Boundary Layer Facility (DUBLF), the wind tunnel used in this research, is characterized for $Re_\tau \geq 1000$. Most numerical research is performed at lower Re_τ because of the cost involved in high Re_τ DNS. The results of several high Re_τ DNS simulations are collected and shown in Figure 2.12.

2.2.6. Streamwise development
From the moment the transverse forcing is applied the drag reduction will gradually converge to its maximum along the streamwise direction. Ricco and Wu [25] studied the streamwise development of C_f experimentally using a water channel and found that the drag reduction will stabilize after $x/\delta \approx 3$. Upstream of this the drag reduction will be present, but not at its maximum value. Directly downstream of the forced area the drag reduction effects disappear within $x/\delta \approx 2$.

The work of Knoop et al. [48] reinforces these findings and argues that C_f is strongly reduced within $x/\delta \approx 1.5$. The attenuation of the $\langle u'u' \rangle$ and $\langle u'v' \rangle$ Reynolds stress tensor components stabilizes within a shorter distance, in the order of $x/\delta = 0.1$. The skin friction coefficient remains in the reduced state for the entire streamwise length of the forced area, which for this study was up to $x/\delta = 11.5$.
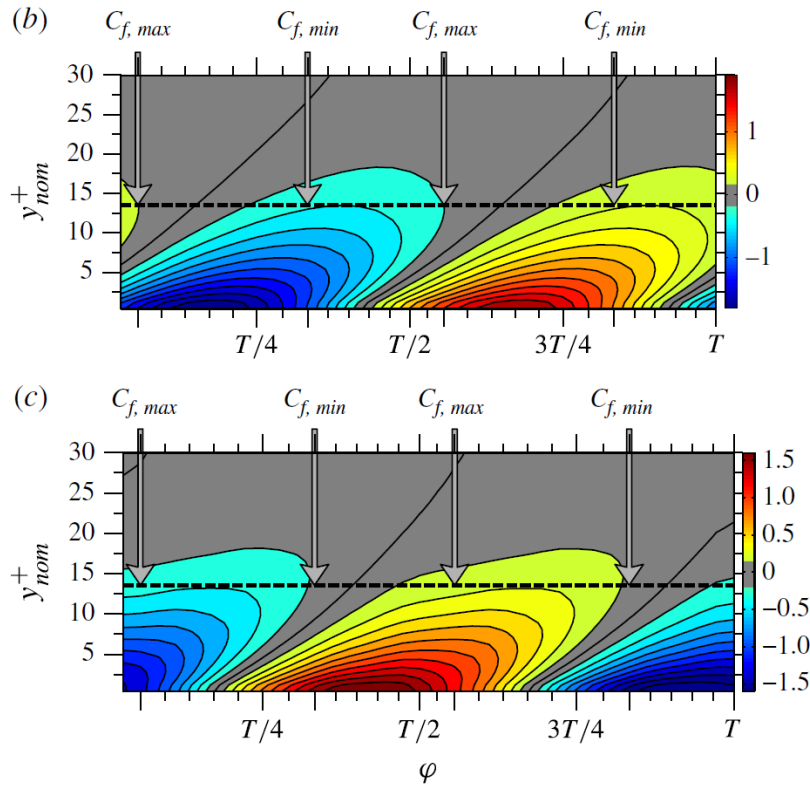
Figure 2.9: Comparison between contours of the Stokes strain $(\partial \tilde{W}/\partial y)$ and contours of the phase-wise derivative of the Stokes strain, all at $T^+ = 200$, taken from [32]

2.2.7. Research gaps

All research done so far has been using either DNS or experimentally, and as discussed in previous sections both have their limitations. DNS is very costly for higher Reynolds numbers, thus can only simulate a limited part of the parameter space given in Equation 2.9. Experiments can reach higher Reynolds number, however often the amplitude and period of oscillation can not be independently varied due to mechanical constrains. Experiments are also limited in the waveforms they can simulate. An opportunity therefore arises to develop an experimental setup that can vary W_m^+, T^+ and Re_τ independent from each other, providing means to single out the effect of changing one of the parameters. Finding the relation between Re_τ and the drag reduction is an important step in predicting the real-world application potential.

One could achieve this effect by flipping the reference frame, instead of oscillating the wall to create the forcing effect keep the wall stationary and oscillate the flow. Measurements could be taken using a stationary measurement volume, with the flow oscillating the effect on the entire phase of the oscillation can be sampled in a single run.
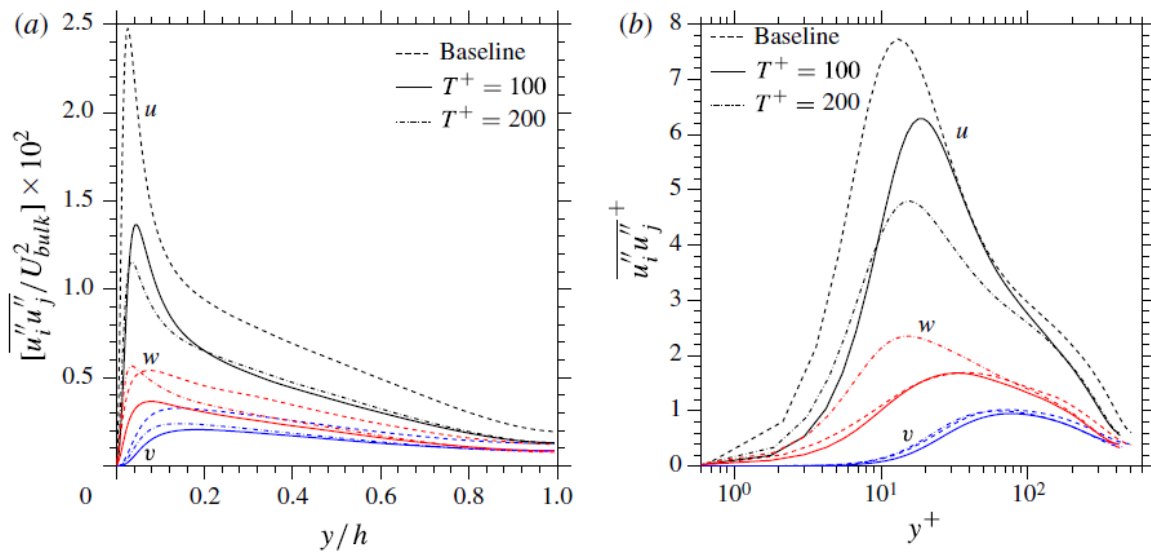
Figure 2.10: Reynolds normal stresses from simulation data with $Re_\tau = 500$, (a) outer-scale units, (b) inner-scale units. Taken from [31].
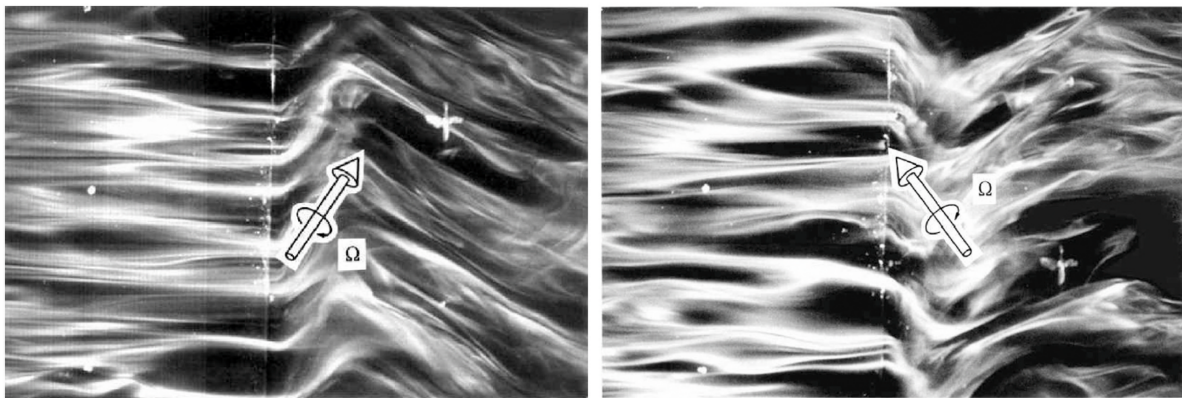
Figure 2.11: Flow visualised using smoke by Choi et al. [8]. The leading edge of the oscillating wall is visible in the image, moving up in the left picture and down in the right. The flow comes from the left edge. The arrow indicates the vorticity vector, tilted in both cases up in the transverse direction, during both phases of the oscillation. This creates a net transverse tilting of the vorticity, modifying the streamwise velocity profile. Taken from [8].
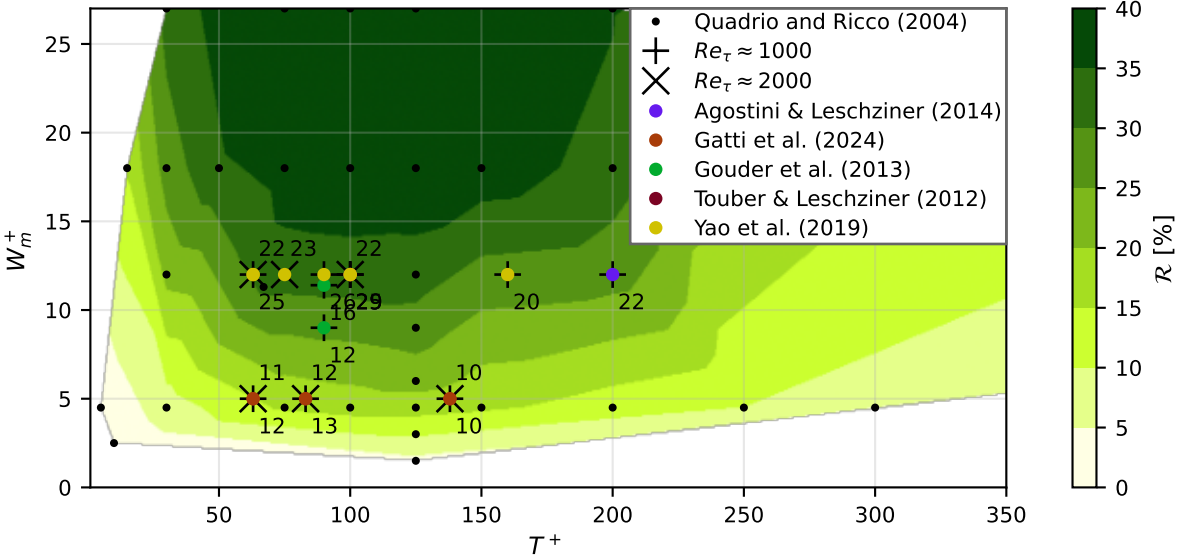
Figure 2.12: Collection of high Re_τ DNS research results, the numbers next to the datapoints denote the drag reduction found in [%], above the point corresponds to $Re_\tau \approx 2000$ and below $Re_\tau \approx 1000$. Data taken from [5], [32], [14], [27], [31] and [33].

2.3. Acoustics

Acoustic forcing is driving the flow in an oscillatory manner using acoustics, generated by a speaker driver. Acoustics are usually discussed in the context of sound waves propagating through a domain, however, for this research the near field aerodynamic effects are of particular interest.

2.3.1. Thiele-Small parameters

A speaker driver can be characterized using the Thiele-Small (TS) parameters. The basic TS parameters that manufacturers provide for a speaker driver are: the equivalent piston area of the diaphragm S_d, moving mass including the acoustic load M_{ms}, the compliance of suspension C_{ms}, the mechanical resistance of suspension R_{ms}, the coil inductance L_e and Direct Current (DC) resistance R_e and the product of magnetic flux density and wire length Bl [49]. These parameters can be used to calculate the resonant frequency f_s of a speaker driver

$$f_s = \frac{1}{2\pi\sqrt{C_{ms}M_{ms}}}$$

(2.16)

and the reference efficiency η_0 at this frequency

$$\eta_0 = \frac{\rho(BlS_d)^2}{2\pi c M_{ms}^2 R_e}$$

(2.17)

with c the speed of sound. A speaker driver does not operate well at frequencies below the resonant frequency. This is because the impedance rises dramatically below f_s as it becomes purely resistive, the inductive and capacitive impedance cancels out. The speaker will also run into the maximum excursion distance, above which the speaker will mechanically damage itself. As seen in Equation 2.16, adding mass can lower the resonant frequency. Using these parameters a speaker can be modified to the required resonance, this does reduce the efficiency and thus the power budget.

2.3.2. Measuring acoustic particle velocity

Accurate measurements of the acoustic particle velocity is important to quantify the amount of forcing that is applied to the flow. Usually the acoustic pressure field is measured using microphones, then the particle velocity is calculated using the linear acoustic wave equations [50]. In the near-field of the speaker these equations are not valid, and thus this method can not be used.

Another method for measuring velocity is Hot-Wire Anemometry (HWA) [51]. HWA provides excellent temporal resolution and can measure the generally low velocities in sound waves. Downsides are that the probe measures only in a single point and it needs to be calibrated. Calibrating the probe for the low particle velocity experienced in sound waves can be difficult.

Laser Doppler Velocimetry (LDV) is a non-intrusive method to measure the particle velocity. LDV can sample at high frequencies and advanced methods exist to reduce noise in the measurements [52]. The disavantage of LDV is that it is complex to set up and it only measures in a single location.

Using Particle Image Velocimetry (PIV) for quantifying an acoustic velocity field is a more recent development. An advantage of using PIV is that it is non-intrusive and it can measure a whole plane instantaneously. Using stereoscopic PIV it is also possible to measure the velocity in all 3 axes. However, PIV measures usually at much lower frequency than the sound waves. Fisher et al. [50] describe a method where PIV image pairs are taken at fixed points 180° spaced apart in the phase of the sound wave, after which the second measurement is subtracted from the first. This yields twice the acoustic particle velocity. The flow velocity $\vec{u}$ in a turbulent section is composed as follows:

$$\vec{u}(\vec{x},t) = \vec{u}_0(\vec{x}) + \vec{\tilde{u}}(\vec{x},t) + \vec{u}'(\vec{x},t) + \vec{b}(\vec{x},t)$$

(2.18)

where $\vec{u}_0$ is the mean (bulk) flow, $\vec{u}'$ are the turbulent fluctuations, $\vec{b}$ is the measurement noise and $\vec{\tilde{u}}$ is the acoustic particle velocity, which depends on the phase of excitation of the sound wave [53]. Using a large number of image pairs cancels out the turbulent term u' since these fluctuations are considered stochastic. Then image pairs taken over the rising side of the sound wave can be subtracted from pairs taken over the falling side, canceling out the mean flow $\bar{u}$ leaving twice the acoustic particle velocity $2\vec{\tilde{u}}$. This is illustrated in Figure 2.13 and under the assumption that $\vec{u}'$ is not correlated with $\vec{\tilde{u}}$, which is the case when the acoustic perturbations do not alter the flow dynamics and are carried by the flow.
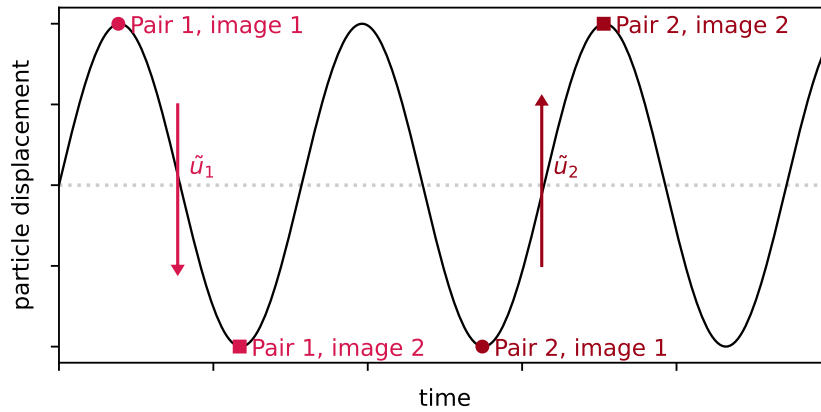
Figure 2.13: Timing of the capturing of phase-locked image pairs. An arbitrary number of phases can elapse between the image pairs.

Measuring the oscillatory boundary layer

Interaction between sound waves and a surface will result in an oscillatory boundary layer. Measuring this boundary layer accurately is crucial to quantify the friction drag on the surface. Huelsz et al. [54] used HWA to measure the boundary layer resulting from standing waves at 35, 46 and 130 Hz. The results of their experiments are shown in Figure 2.14 and line up with linear theory, indicating that HWA is a valid tool to measure the boundary layer.

2.3.3. Acoustically transparent tunnel walls

Kevlar is a commonly used material for acoustically transparent tunnel walls. The material can be stretched across a gap in the solid wall and maintain the aerodynamic shape, while having a very low acoustic transmission loss. The most commonly used Kevlar fabric is style K120 with K49 yarns, which is the lightest weave available [55]. It's tensile strength is greater than that of mild steel. The transmission loss is shown in Figure 2.15, for low frequencies the loss is negligible.

The material has a rough surface due to it being composed of weaved yarns. This roughness creates aerodynamic noise. This noise was measured experimentally for the K120 - K49 material and is shown in Figure 2.15. The noise emitted is around $\mathcal{O}(10)$ dB with frequency $\mathcal{O}(10^4)$ Hz for a freestream velocity of 50 m/s. The frequencies used for the excitation of the flow in this research will be much lower and with much greater intensity, therefore this will not interfere with the measurements.
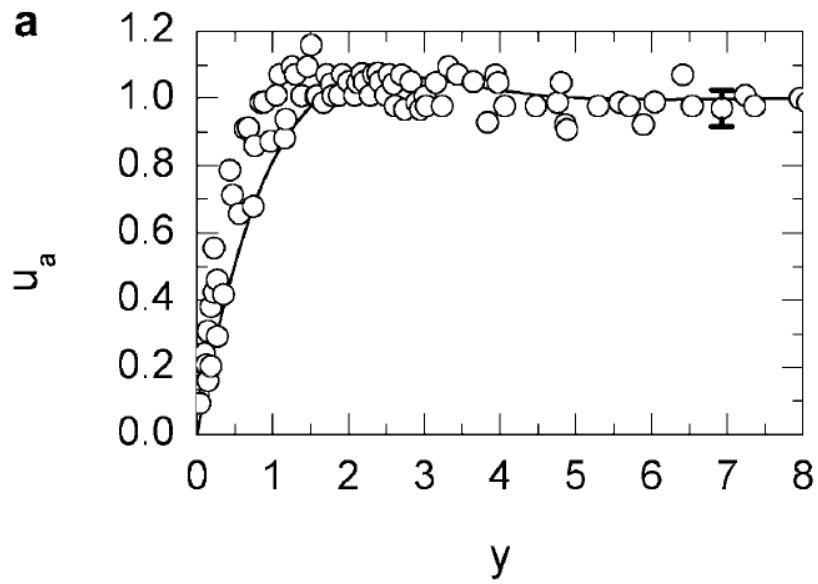
Figure 2.14: Amplitude of the velocity u_a in the streamwise direction plotted as a function of distance to the surface y, both non-dimensionalised using inner scaling, for the 35 Hz case from Huelsz et al.[54]
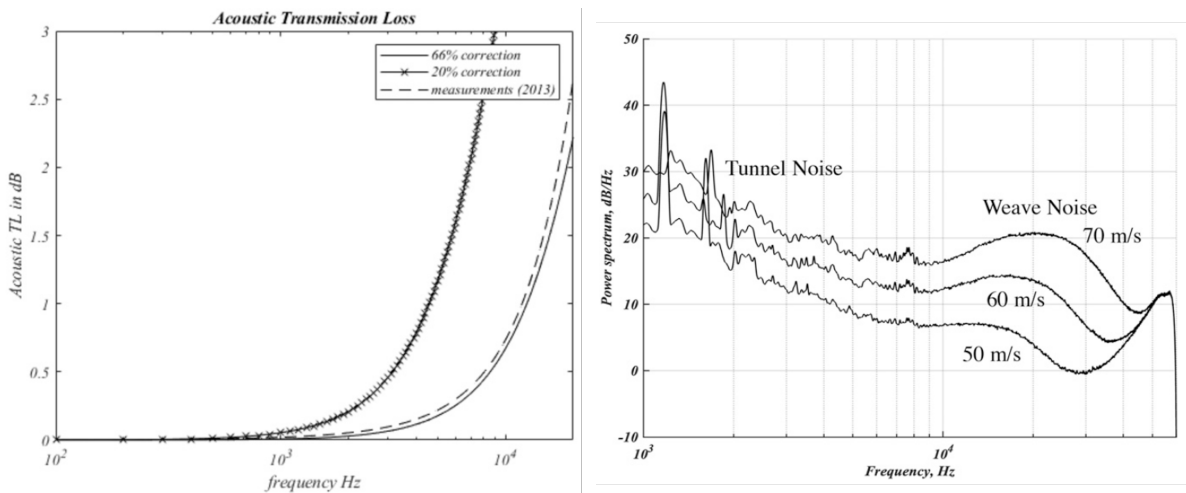
Figure 2.15: The left figure shows the acoustic transmission loss through a 58 gm/m^2 Kevlar fabric, compared to an empirical model with 66% and 20% porosity. The right figure graphs the background noise from experimental measurements, showing the Kevlar weave noise at high frequencies. Taken from [55].

<div align="right">

3

</div>

Experiment methodology

This chapter will describe the experimental setup used in the current research. It will begin with the design process in Section 3.1. The final design of the setup is shown in Section 3.2.2. The flow measurement techniques used are listed in Section 3.3 and the characterization of the speaker output is described in Section 3.4. The chapter will conclude with a description of the experiment procedure in Section 3.5.

3.1. Design

This section summarises the process of designing the acoustic forcing experimental setup. It will begin with the requirements in Section 3.1.1, a numerical simulation is explained in Section 3.1.2 and finally the selection process for a speaker driver is described in Section 3.1.3.

3.1.1. Experiment requirements

The primary goal of this research project is to validate the use of acoustics for transverse forcing. The experiment must therefore be able to replicate the conditions of prior work using conventional methods. The results of several DNS studies was collected, as described in Section 2.2.5. A point was chosen from the parameter space where $T^+ = 83$, $W_m^+ = 5$ and $Re_\tau = 1000$. This point was selected because a recent DNS study from Gatti et al. [14] used the same conditions and it has a relatively low amplitude while still generating a measurable drag reduction. Furthermore, as is explained in Section 2.3.1, a speaker will perform better at higher frequency and thus can achieve the same forcing parameters at higher Re_τ, until it reaches its power limit.

3.1.2. Simulations

To estimate attenuation rate and the requirements on the speaker drivers a Computational Fluid Dynamics (CFD) simulation was performed in Ansys CFX 2024 R2. This simulation featured a box shaped domain with a cross section equal to the DUBLF, 600 mm $\times$ 900 mm. The length of the domain was set at 2400 mm and a freestream velocity U_∞ corresponding to $Re_\tau = 1000$ was imposed. A schematic overview of the simulation is shown in Figure 3.1. The simulation was done using an incompressible solver and therefore the acoustic wave is not modeled, leaving the convective motion. As this is within the near-field of the speakers and the accuracy was not of great import this simplification was considered acceptable. The speaker drivers were modeled by creating a gap in the domain at their locations and imposing a velocity in the transverse direction u_z over them. As the speakers are moving in phase the total volume of fluid remained constant.

The simulation was performed across a single actuation period, the velocity on the centerline of the speakers is shown in Figure 3.2 for the whole of the period. From this plot a few conclusions can be drawn, mainly that the velocity field only follows a pure sine wave in the middle of the domain $z = 0$. This is the result of the 'pushing' actuator, with inwards velocity, inducing more velocity than the 'pulling' actuator with outwards velocity. As expected the direction of flow is not important, both halves of the

phase are exactly opposite.

The main variable of interest was the attenuation rate r_{att} between the velocity at the actuator u_{act} and at the centerline u_0. This is defined as $u_0 = r_{att}u_{act}$. Figure 3.3 shows the decay of u_z in the transverse direction at the centerline between the actuators. From this graph the average decay over the streamwise length of the actuator was estimated to be $r_{att} \approx 0.55$. This value was used to determine the requirements for the speaker driver.

3.1.3. Speaker driver selection

One of the primary parts in this experiment are the speaker drivers. The main parameters for selecting a speaker driver in this case are the resonant frequency f_s and the speaker power P_s. This section describes the process of converting the oscillation parameters into these quantities. This method simplifies the complex 3-dimensional flow created by the speaker to a simple 1-dimensional model, and therefore should be treated as an estimation. It was considered accurate enough to make a informed decision on which speaker to use based on the information available from the manufacturers.

The friction velocity u_τ is calculated using

$$u_\tau = \frac{Re_\tau \nu}{\delta} \tag{3.1}$$

with ν as the kinematic viscosity, Re_τ as the friction Reynolds number and defined in Section 3.1.1 and δ as the boundary layer thickness, resulting from the DUBLF tunnel characterization, as explained in Section 3.2.1. Using u_τ the oscillation parameters are dimensionalized, with the frequency f as

$$f = \frac{u_\tau^2}{T^+\nu} \tag{3.2}$$

and velocity amplitude W_m as

$$W_m = W_m^+ u_\tau \tag{3.3}$$

The velocity required at the actuator u_{act} is calculated using $u_{act} = W_m/r_{att}$, with $r_{att} = 0.55$ as the attenuation rate taken from the simulation described in Section 3.1.2. The resonant frequency of a speaker can be modified by changing the moving mass M_{ms}. The required mass can be calculated when assuming that the operating frequency f is equal to the resonant frequency f_s using

$$M_{ms} = \frac{1}{C_{ms}(2\pi f_s)^2} \tag{3.4}$$

where C_{ms} is the suspension compliance of the speaker driver. Using the T/S parameters the reference efficiency η_0 can then be calculated with

$$\eta_0 = \frac{\rho(BlS_d)^2}{2\pi c M_{ms}^2 R_e} \tag{3.5}$$

where ρ is the air density, Bl is the product of magnetic flux density and the voice coil gap, S_d is the speaker area, c is the speed of sound and R_e is the DC resistance of the speaker coil. Typically subwoofer speakers drivers have a $\eta_0 < 2\%$. The required RMS power P_{req} is calculated using

$$P_{req} = u_{act}p_{act}\frac{1}{2}\sqrt{2} \tag{3.6}$$

with p_{act} as the average pressure amplitude over the actuator, taken from the simulation of Section 3.1.2. Then, under the assumption that the reference efficiency η_0 is applicable in the near field of the speaker driver, the required speaker power P_s can be calculated using

$$P_s = \frac{1}{\eta_0}P_{req} \tag{3.7}$$

A list of available speaker drivers was composed and for each the speaker power and added mass was calculated. This was then compared to the power available and price of the speaker driver. The B&C 18TBX100 speaker driver was selected as a good compromise between price and functionality. The full list of speakers and their capabilities are shown in Appendix D.
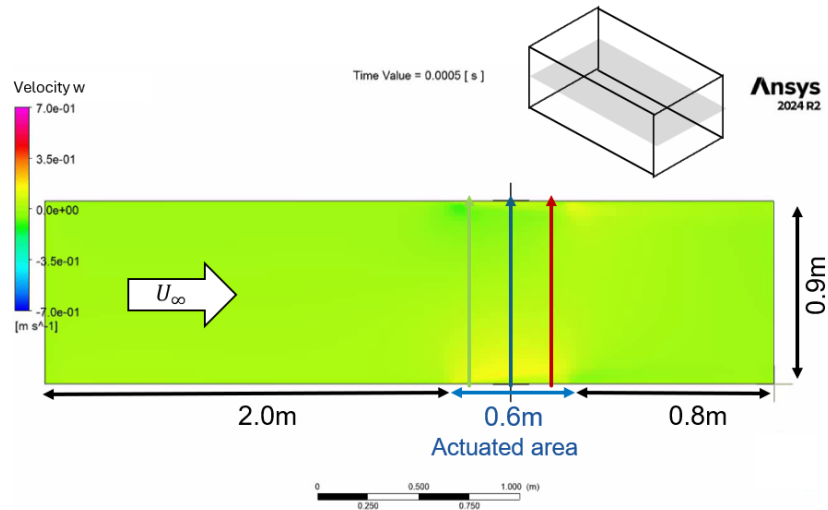
Figure 3.1: Schematic overview of a CFD simulation of the test setup.
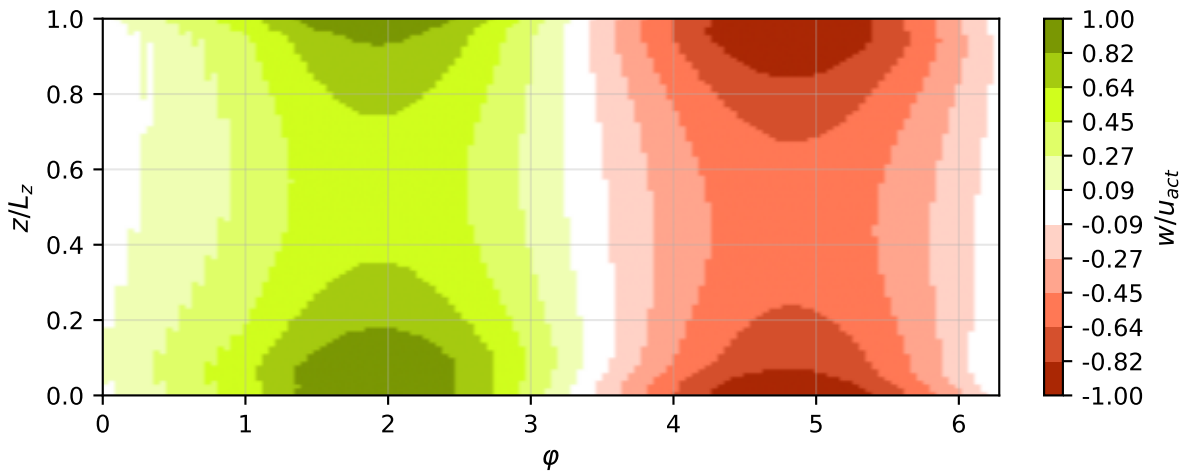
Figure 3.2: Velocity in the transverse direction u_z at the centerline of the speaker drivers (Blue line in Figure 3.1) over a single oscillation phase.
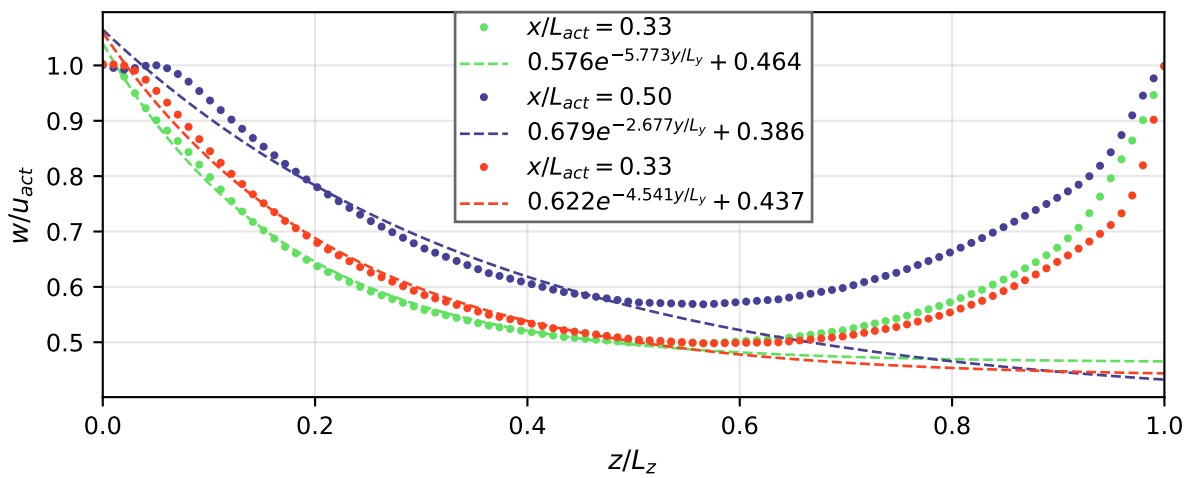
Figure 3.3: Peak velocity in the transverse direction w at 3 different lines perpendicular to the speaker drivers (Green, blue and red lines in Figure 3.1), normalised with the actuator velocity.

3.2. Experimental setup

The experiment was conducted using the existing test section of the DUBLF with modified walls and a custom designed speaker setup. A schematic overview of the test setup is shown in Figure 3.4. A description of the DUBLF is given in Section 3.2.1 and the speaker setup is explained in Section 3.2.2.

3.2.1. Delft University Boundary Layer Facility

The DUBLF with the turbulent boundary layer flat plate setup has a single axial fan powering the tunnel. The flow then passes through a diffusing section into the heat exchanger, as the tunnel is designed to be able to run in a closed return configuration. Next there are two 90° corners after which another diffuser expands the flow into the turbulence screens. After the contraction is a test section of 7.5m length and 0.9m $\times$ 0.6m cross section. The section is slightly diverging to maintain a zero pressure gradient. The end of the test section vents into open space through a mesh to create a slight positive pressure in the tunnel, causing any leaks to spill flow outwards. The test section features transparent walls for optical flow visualization techniques. It is built using modules, such that it can be adapted to suit the experiment requirements. At the start of the test section is a strip of P40 grit sandpaper to trip the boundary layer.

The working section of the DUBLF consists of a 7.5 m flat plate. The boundary layer is tripped into turbulence at the leading edge and grows along its length. The large section length creates a high Re_τ flow with a small U_∞. Therefore the boundary layer is well developed at the end of the test section, and thus it can be assumed to be in equilibrium for the measured length, see Section 5.2.1 for more detail. A photo of DUBLF is shown in Figure 3.5.

The DUBLF is controlled using a desktop PC with custom software. Here the RPM of the tunnel can be controlled and an internal PID controllers ensures a stable output. At the speeds tested at the wind tunnel RPM and U_∞ followed a linear relation, and thus the tunnel speed can be set in a precise manner to the desired value. The computer also has a data acquisition, with which the tunnel velocity can be captured by averaging this over a period of time. It is also connected to a temperature T and pressure p sensor, with which the air density ρ is derived using the ideal gas law:

$$\rho = \frac{p}{R_{specific}T} \tag{3.8}$$

with $R_{specific}$ as the specific gas constant of air. Freestream velocity U_∞ is captured using a pitot-static tube just upstream from the measurement area. This is connected to multiple pressure sensors with different measurement ranges for optimal accuracy.

DUBLF Characterization

The tunnel is able to reach Re_τ up to 8000, which corresponds to a tunnel velocity of approximately 50 m/s. The tunnel has been characterized using HWA up to a velocity of 18.3 m/s. The result of this is shown in Table 3.1. The boundary layer profile is independent of Reynolds number up to $y^+ \approx 300$. The turbulence kinetic energy is highest at $y^+ \approx 15$ for all velocities. This peak is caused mainly by fluctuations of friction wavelength $\lambda_x^+ \approx 1000$ or $T^+ \approx 110$, as seen in Figure 3.6.

3.2.2. Speaker setup

The speakers are positioned using a frame made from aluminium extrusions, with cross bracing to increase its stiffness and resistance to vibrations. The speakers are mounted to the frame with 12 mm thick wooden multiplex panels. To dampen the vibrations from the speakers the frame is placed on rubber mats. The speaker frame is physically separated from the wind tunnel test section to prevent

Table 3.1: Characterization of the DBLF, taken from Knoop et al. [56].

U_∞ [m/s]	Re_τ	δ [mm]	U_τ [m/s]	l_ν [mm]
4.6	1300	108	0.18	82.31
9.2	2400	109	0.34	45.34
13.8	3500	108	0.49	30.97
18.3	4510	107	0.64	23.78
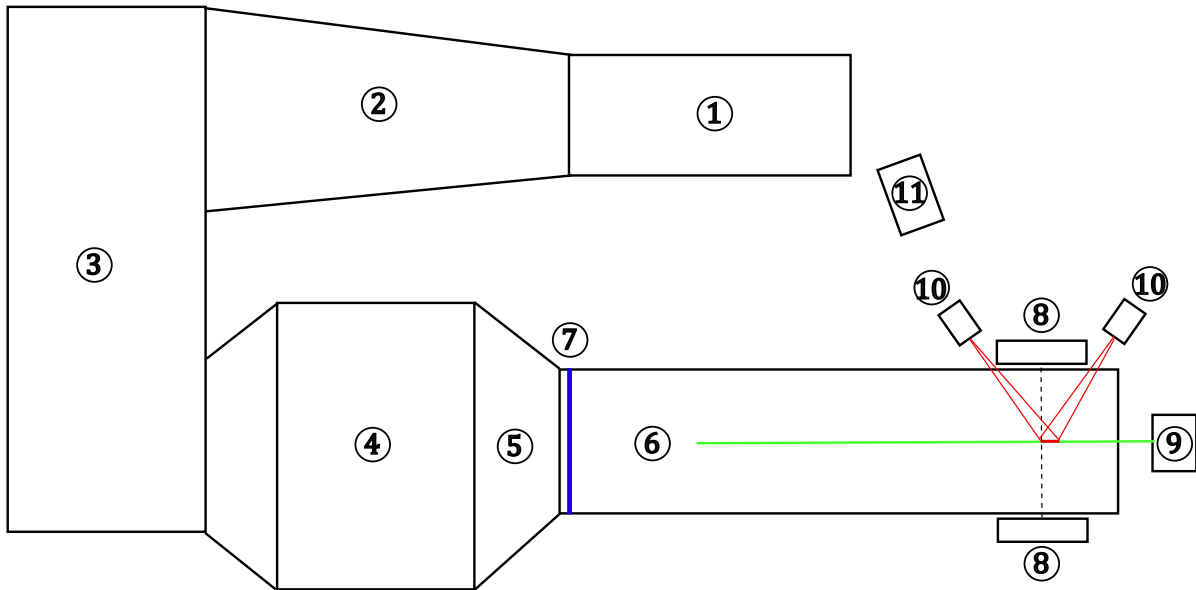
Figure 3.4: Schematic overview of the test setup, seen from above (not to scale). The flow moves in a anti-clockwise direction, the following objects are marked: 1. Fan unit, 2. Diffuser, 3. Corners with vanes, 4. Settling screens, 5. Contraction, 6. Test section, 7. Trip strip, 8. Speakers, 9. PIV Laser, 10. PIV Cameras, 11. Smoke generator.

vibrations from having unintended effects on the flow. A photo of the speaker setup is shown in Figure 3.7.

The two 18TBX100 speaker drivers, with their specifications listed in Table 3.2, are driven using a 6 kW 4-channel Behringer NX4-6000 amplifier. Two of the channels of the amplifier can be bridged to get two 3 kW audio channels. The audio signal is generated by a custom designed tone generator, shown in Figure 3.8. This program generates a stereo sine wave audio signal of which the phase and amplitude can be independently adjusted for both channels. To ensure repeatable results the volume on the amplifier was always set to the maximum and the amplitude was controlled from the tone generator, the output denoted with A_{in}.

As the amplifier can supply more power than the speakers are able to handle care must be taken with the amplitude of the input signals. Therefore a thermocouple was placed on each speaker to monitor the internal temperature and to prevent damage to the speakers. It was also found that the speaker output had a slight temperature dependence, which might cause drift in the measurements. To prevent this the speakers were actuated until the temperature stabilised before commencing the data acquisition.

The Data Acquisition (DAQ) system captured several channels, listed in Table B.1. Among these channels are the electrical signals to the speakers, to verify that the correct forcing frequency and amplitude was applied in each measurement. The signal to speaker A, which is defined as the speaker on the right-hand side of the tunnel when looking in the streamwise direction, was used as a reference for all phase designations. The temperature of the speakers and the Q-Switch input for the laser pulses are also monitored and recorded using the DAQ system.

	Behringer NX4-6000 Amplifier	18TBX100 Speaker driver
Power	4×1600 W or 2×3000 W	2400 W continuous
Frequency response	20 Hz to 20 kHz, $+0/-2$ dB	35 Hz to 1000 Hz
Signal to noise	> 100 dB	
Resonant frequency		30 Hz
Sensitivity		94 dB

Table 3.2: Specifications of amplifier and speaker.

Figure 3.5: Photo of the Delft University Boundary Layer Facility (DUBLF). The intake of the fan is seen on the right of the image, the flow passed a diffuser and 2 corners at the farthest wall in the room, seen from where the image was taken. After the settling screens and contraction, seen in the middle of the image, the flow passes through the test section and exits through the mesh at the left of the image.
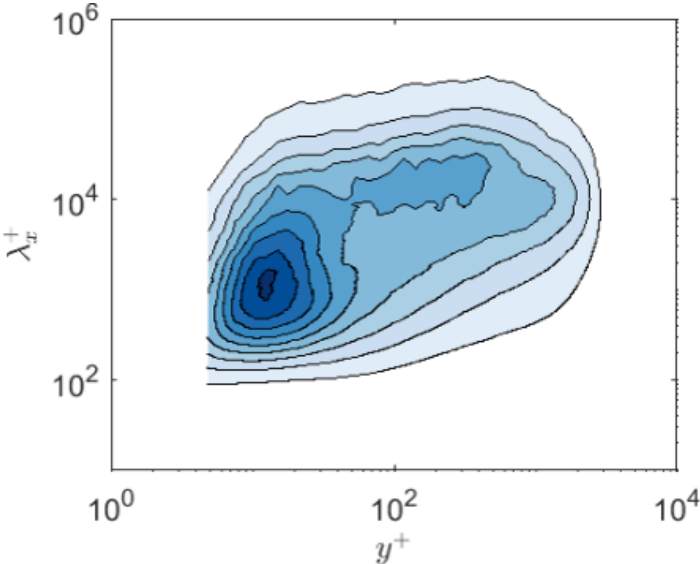
Figure 3.6: Velocity spectrogram corresponding to the measurement at $Re_\tau \approx 3500$, taken from Knoop et al. [56].

Figure 3.7: This photo shows the test section of the DUBLF with the acoustic forcing speaker setup. The speakers are mounted at the end of the test section. In the bottom right of the image the PIV laser is visible, the emitted beam passes vertically through the optics after which a small mirror rotates it horizontal.

Figure 3.8: Screen capture of the audio generator software, on the left are the current settings displayed, the middle column is used to set the input variables and on the left the settings for the phase locking signal are set and displayed.

3.3. Flow measurement techniques

This section describes the flow measurement techniques that are used. The flow was visualised using Particle Image Velocimetry, as explained in Section 3.3.1. The speaker output was measured using a microphone, detailed in Section 3.3.2

3.3.1. Particle Image Velocimetry

The flow between the speakers is visualized using PIV. The flow is seeded using a SAFEX Twin Fog DP smoke generator, with an approximate particle diameter of 1 μm. The particles are illuminated using an Quantel Evergreen EVG00200 Double pulse Nd:YAG laser. The laser beam passes through a set of optics to form a sheet, seen in Figure 3.9. The power was set at 70% of the 200 mJ per pulse. The particles are imaged using one or two LaVision Imager sCMOS CLHS cameras with Nikkor AF-S 200 mm lenses, depending on the measurement type. The seeding density was adjusted to ensure that at least 3 particles are present in each interrogation window. This was done using a test image of which the average pixel intensity was calculated. This was then compared to a reference value of which the seeding density was known to be correct.

The data was captured using several PIV planes, shown in Figure 3.10. Their dimensions and directions are described in Table 3.3. Each plane was calibrated using images of a bespoke calibration sheet and the LaVision Davis software. Most of the measurements were done using the p5020 plane, using stereoscopic PIV. The upstream and downstream camera were placed at respectively 43.6 ° and 32.2 ° to the normal (z) axis. The plane of focus was angled using a Scheimpflug adapter to compensate for this angle.

Capture timing

Two methods for the timing of the PIV images were used. The first is using random sampling, were the PIV acquisition frequency f_{PIV} has an irrational ratio to the audio frequency. This was the main method during the experiment, as the random sampling ensured that each part of the phase was captured equally, giving a representative average. This also ensured that any drift in the setup is randomly distributed and thus the effect was minimal. The number of images taken allowed for phase averaging a posteriori. An example of this method is illustrated in Figure 3.11.

The second method is by phase locking the PIV acquisition to the audio signal. This method allows a large number of images to be taken at the desired part of the phase, for instance at peak velocity. The PIV acquisition frequency f_{PIV} using phase locking is given by

$$f_{PIV} = \frac{f}{\left\lceil \frac{f}{f_L} \right\rceil} \tag{3.9}$$

with f as the audio frequency and $f_L = 15$ $[Hz]$ as the maximum laser frequency. $\lceil x \rceil$ denotes the ceiling function, where the value x is rounded to the least integer greater or equal to the value. An example of this method is illustrated in Figure 3.11. During the characterization it was found that the phase delay between the electrical input signal and the resulting velocity wave was highly frequency dependent, making it difficult to determine where in the phase the images must be taken. It was therefore decided to not use phase locking further in the experimental campaign.

Processing

All PIV measurements are processed using the flowmaster environment of LaVision DaVis software, version 10.2.1. Before the measurements a calibration is performed defining the axes on the image.

Plane	p120p	p120s	p5020	wp160
Normal direction	z-axis	z-axis	z-axis	y-axis
Type	Planar	Stereo	Stereo	Planar
Dimensions [mm]	153.5×127.5	114.0×114.5	56.3×21.0	183.1×153.2
Calibration fit error [pixels]	0.6212	1.8887	0.4974	0.2392
Resolution [pixels/mm]	16.6	22.8	51.6	15.6

Table 3.3: Nomenclature and dimensions of all PIV planes.

Figure 3.9: Photo capturing the emitted PIV laser sheet. The sheet is cut in the middle by the trailing edge of the plate, this is to ensure the lowest light is parallel to the plate, minimizing reflections.

This is done using an image of the calibration plate, with even spaced symbols in both x and y directions. The plate is placed at the same location as the laser sheet. The software detects the markings automatically, after which it calculated the appropriate transform to convert the raw images into vector fields with the correct coordinate system.

The images are pre-processed first, where from each set of 9 images the average is subtracted. This ensures that any background light is removed, leaving only the particles illuminated. All pixels are normalized to the first frame using the local average over 20 pixels. A constant of 100 counts of light intensity is subtracted to remove background noise. These operations cause the particles to be clearly distinguishable by the PIV cross-correlation algorithm.

The pre-processed images are then further processed using the PIV method of the software. All measurements were processed using the standard cross-correlation algorithm. A min/max filter with $L = 4$ is applied and the vector validation option is used. The vectors are calculated with multiple passes of decreasing interrogation window sizes. Usually a 24×24 pixel window with 75% overlap was used for the boundary layer characterization, full Field of View (FoV) processing and for the wall-parallel measurements. The image pairs of the p5020 PIV plane stereo measurements were processed again with more detail. The interrogation window size was decreased such that at least 4 vectors are present in the region $\frac{1}{2}y^+_{window} \leq y^+ \leq 5$, with y^+_{window} half the height of the interrogation window, to get an accurate estimation of u_τ. The maximum interrogation window size therefore decreased with increasing Re_τ, from 12×12 pixels at $Re_\tau = 1000$ up to 6×6 pixels at $Re_\tau = 3000$, each with 75% overlap. To increase processing speed the image is cropped to approximate -1 mm $< y < 2$ mm, with the plate location at $y = 0$. To get a better result the average velocity field of the coarse window is used as input for the pre-shift, this increased the vector quality and processing speed.

For each vector field the location of the plate is determined by finding the symmetry plane between the velocity profile on each x-location and it's reflection in the plate. All vector fields are then corrected for such that the plate is at $y = 0$, then averaged. The average of all vector fields is then averaged in the x-direction to get the velocity profile, based on the assumption that the boundary layer is in equilibrium, see Section 5.2.1. The friction velocity u_τ is calculated using the gradient of this velocity profile at $\frac{1}{2}y^+_{window} \leq y^+ \leq 5$, where $y^+ = 5$ is calculated recursively using the calculated u_τ, for this 1 to 2 iterations were needed. For each unforced case 1500 image pairs were taken, for the forced cases 3000. The detailed processing with small interrogation window gives 975 vectors in x for $Re_\tau \leq 2100$ and 1462 vectors for $Re_\tau > 2100$. The number of samples used per wall-normal point for the calculation of u_τ thus ranges from $1\,462\,500$ the low Re_τ unforced cases to $4\,386\,000$ for the high Re_τ forced cases.
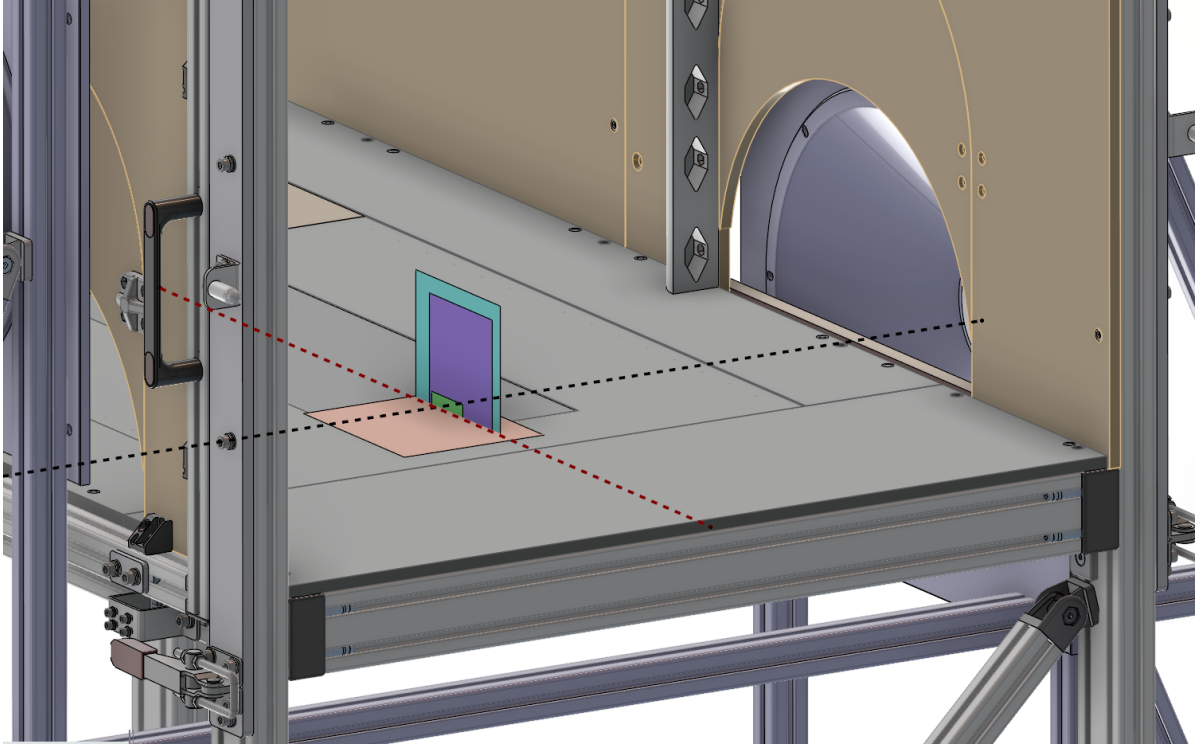
Figure 3.10: Schematic representation of all PIV planes listed in Table 3.3. Cyan corresponds to p120p, purple to p120s, green to p5020 and orange to wp160. The black dashed line is the speaker centerline and the red line the middle of the test section.
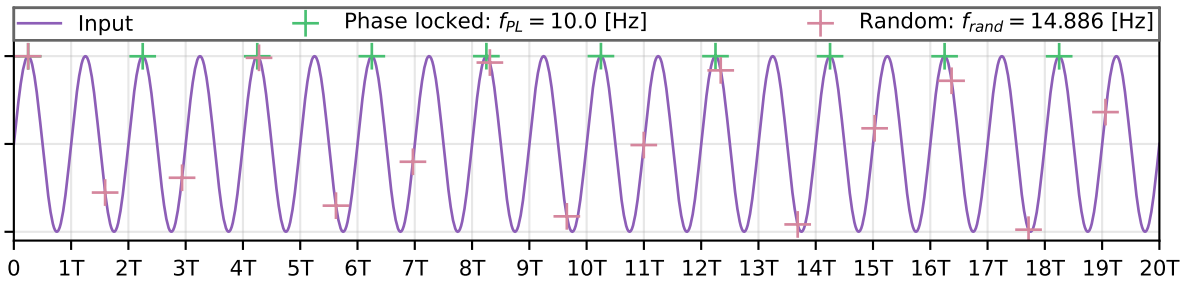
Figure 3.11: Plot illustrating the two methods of PIV capture timing, using an input signal of $f = 20$ Hz, T denotes the input signal period.

A full description of this process is found in Appendix B. The friction coefficient is calculated using

$$C_f = \frac{2u_\tau^2}{U_\infty^2} \qquad (3.10)$$

and then the drag reduction is given by

$$\mathcal{R} = 1 - \frac{C_f}{C_{f_0}} \qquad (3.11)$$

Uncertainty quantification

The uncertainty in the PIV measurements is quantified using the method of Sciacchitano and Wieneke [57]. The uncertainty of the temporal average of the velocity $U_{\overline{u}}^{(t)}$ is given by

$$U_{\overline{u}}^{(t)} = \sqrt{\frac{\sigma_u^2 + \overline{U_u^2}}{N_{eff}}} \qquad (3.12)$$

with σ_u^2 the standard deviation of the velocity over the time period, $\overline{U_u^2}$ the average squared uncertainty of the instantaneous velocity and N_{eff} the effective number of samples. The image pairs are taken with $f \leq 15\,Hz$, at $Re_\tau \approx 1300$ this results in the flow moving by $\Delta x \approx 1.5x_{vector}$ at $y^+ = 5$, with x_{vector} the distance between the vectors. Therefore the samples are uncorrelated and thus the effective number of samples are equal to the total number of samples $N_{eff} = N$.

The uncertainty of the spatial average in x of the velocity $U_{\overline{u}}^{(s)}$ is given by

$$U_{\overline{u}}^{(s)} = \sqrt{\frac{\overline{U_u^2}}{N_{eff}}} \tag{3.13}$$

The spatial average is taken from the temporal average, such that $U_u = U_{\overline{u}}^{(t)}$ in the equation above. The number of uncorrelated samples N_{eff} is equal to N_x reduced by a factor of 4 due to the 75% overlap. This gives an uncertainty on the streamwise velocity component of 0.85% at $Re_\tau \approx 1100$ to 0.28% at $Re_\tau \approx 2600$ for the unforced cases. Using this uncertainty and the covariance parameters of the fit a Standard Error (SE) for u_τ was calculated, which ranged from 1.02% to 0.25% for the Re_τ stated earlier. A standard error on U_∞ was calculated using the accuracy of the sensor, this ranged between 0.91% to 0.09%, again for the same Re_τ. Combining Equations 3.10 and 2.9 and using standard error propagation this gives a SE for the drag reduction:

$$SE_\mathcal{R} = \sqrt{\left(\frac{-2u_\tau U_{\infty 0}^2}{u_{\tau_0}^2 U_\infty^2}\right)^2 SE_{u_\tau}^2 + \left(\frac{2u_\tau^2 U_{\infty 0}^2}{u_{\tau_0}^3 U_\infty^2}\right)^2 SE_{u_{\tau_0}}^2 + \left(\frac{2u_\tau^2 U_{\infty 0}^2}{u_{\tau_0}^2 U_\infty^3}\right)^2 SE_{U_\infty}^2 + \left(\frac{-2u_\tau^2 U_{\infty 0}}{u_{\tau_0}^2 U_\infty^2}\right)^2 SE_{U_{\infty 0}}^2}$$
$$\tag{3.14}$$

3.3.2. Microphone measurements

A GRAS 46BE 1/4" CCP Free-field microphone was used to capture the pressure waves emitted by the speakers. This microphone has a dynamic range of 35 dB(A) to 160 dB and a frequency range of 4 Hz to 80 kHz. It was placed at the midpoint between the speakers to have the same attenuation and phase delay for both speakers. The microphone was positioned carefully such that the angle to both speakers was equal. The data was used to synchronize output of both speakers, as explained in Section 3.4.2.

3.4. Speaker characterization

To characterize the flowfield created by the speaker drivers a characterization test was designed and performed. This was conducted in the same location as the full experimental campaign described in Section 3.5. The working section was removed for this test and the volume of air was stationary. A schematic overview of the test setup is shown in Figure 3.12 and a photo is shown in Figure 3.13.

A audio generator program was created to create the speaker input signals. The frequency f, amplitude of speaker A A_{in_A}, amplitude of speaker B A_{in_B} and phase offset $\Delta\varphi$ could be set individually. A signal was generated by the program which triggers the PIV acquisition, as shown in Figure 3.11 and calculated using Equation 3.9. This signal could be offset to capture different points in the phase.

The main objectives of the characterization test were:

- To find the hardware limitations of the system.
- To test the PIV system and perform a convergence study.
- To characterize the frequency response of both speakers.
- To tune the speakers to move exactly out of phase.
- To map the velocity field created on the f and A_{in} field when the speakers are in phase.

The flow was visualized using PIV on a plane of dimensions 380 mm $\times$ 430 mm located at $y = 0$, using the same coordinate system as the wind tunnel, shown in Figure 3.12. The flowfield is assumed to be circularly symmetric around the centerline of the speakers, as the speakers themselves are circularly symmetric. On the basis of this assumption the entire flowfield can be characterized using this single

PIV plane, as it overlaps the centerline of the speaker and the line $y = z = 0$. The same laser, camera and seeding machine as described in Section 3.3.1 were used for this test. On the camera, mounted near the floor pointing upward, a 50 mm focal length lens was mounted. The time difference Δt between the images of an image pair was chosen such that the particle displacement would be approximately $8 - 15$ pixels. The calibration fit had an error of 0.381 pixel and the scale was 5.67 pixel/mm. A 24×24 pixel interrogation window was used on all measurements.

Next to the PIV images multiple channels of data were captured using a NI CompactDAQ data acquisition systems. These channels were captured at a frequency $f_{DAQ} = 51200 \ [Hz]$ and saved using a LabView program. The channels recorded were the microphone pressure p_{mic}, the amplifier input channels V_A and V_B, the audio generator trigger signal and the PIV laser trigger signal.

3.4.1. Hardware limitations
The limits of each of the components in the test setup are documented in their datasheets, however, the actual performance might differ slightly. Therefore the first part of the test was dedicated to finding the limits, such that they would not be exceeded during later tests. At lower frequencies the speakers are bounded by their maximum displacement. At $x_{max} = 9$ mm the sound wave becomes distorted, this is treated as a soft limit. The hard limit is when the voice coil gap is closed entirely, because this is where the speaker starts damaging itself. The voice coil gap of the speakers used is $x_{gap} = 12$ mm. This limit was found visually. At higher frequencies the displacement becomes lower for the same P_s and at a certain point the speaker starts to become limited by P_s. This limit was found by keeping track of the speaker temperature. The maximum allowable input amplitudes for the frequencies tested at are shown in Table 3.4.

3.4.2. Phase matching
Both speaker drivers are of the same model and make. During testing it was discovered that the output amplitude and phase delay was not the same for both speakers. These values varied across the f and A_{in} map, where A_{in} denotes the power of the input signal to the amplifier, ranging from 0 to 1. Therefore, for each of the test frequencies the speakers were synchronized.

The synchronization process started by actuating speaker A at the desired f and A_{in}, with the microphone recording. Then speaker B would actuate at the same input parameters and finally the output of speaker B was recorded at a slightly higher or lower frequency.

A sine wave of the test frequency was fitted to each of the microphone measurement. To the two different speaker B amplitudes a line was fitted and this was used to calculate the required A_{in_B} to match A_{in_A}. The required phase offset $\Delta\varphi$ was calculated using

$$\Delta\varphi = \varphi_B - \varphi_A \tag{3.15}$$

with φ_B as the phase of speaker B output signal and φ_A as the phase of speaker A output signal. The required input adjustments based on these measurements are shown in Figure 3.14 for A_{in} and Figure 3.15 for $\Delta\varphi$.

3.4.3. Results
The results of the characterization were measured using the PIV plane described in Figure 3.12. The measured velocity field is shown in Figure 3.16 for $f = 30$ Hz, which corresponds to the resonant

$f \ [Hz]$	A_{in}	Type
20	0.2	Displacement
30	0.35	Displacement
50	0.5	Power
65	0.5	Power
100	0.35	Power
146	0.35	Power

Table 3.4: Speaker hardware limitations
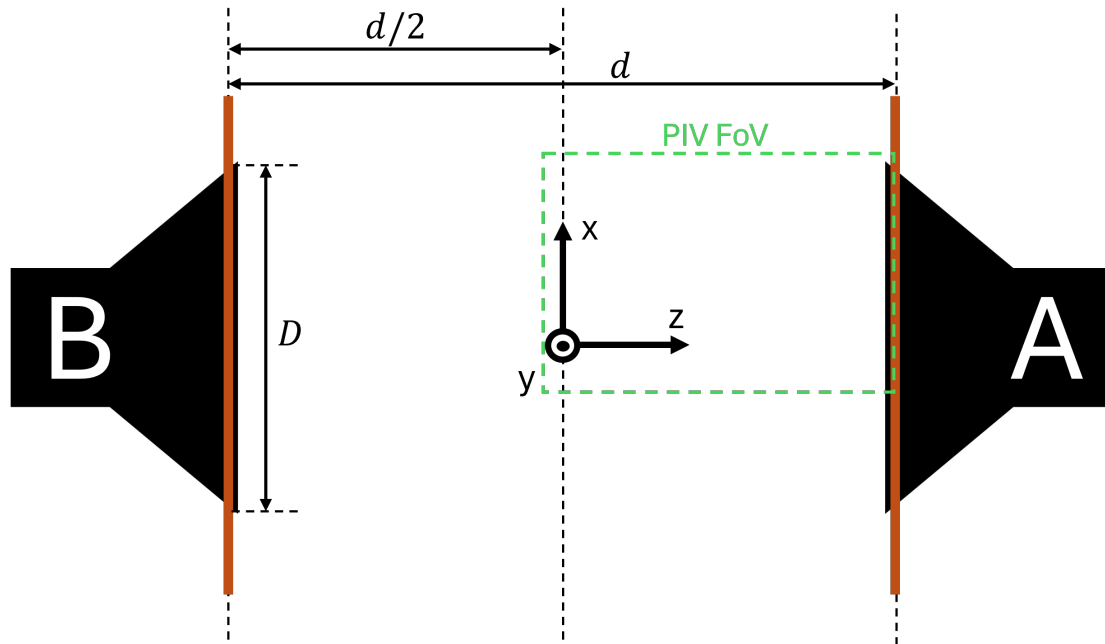
Figure 3.12: Schematic of characterization test setup, seen from above.

frequency of the speakers. The phase is calibrated to $\varphi = 0$ at the zero crossing of the electrical signal to speaker A, denoted with V_A. The contour plots show a top down view of the w-velocity field between speaker A and the center between the speakers. It is assumed that the velocity field at speaker B is the same but mirrored over the centerline between the speakers. It is evident that the 'pushing' motion, when the velocity is positive in the z-direction, propagates further than when the speaker is performing a 'pulling' motion. The 'pushing' motion can be described as a jet of air, while the 'pulling' motion draws fluid from all directions. This gives an inherent asymmetry in the velocity profile everywhere except for the centerline. The non-uniformity of the velocity field also makes this an imperfect analogy to the spatially uniform waves explained in Section 2.2.3. The velocity fields and profiles for the other frequencies can be found in Appendix C.1.

The w-velocity component is largest in at the centerline of the speaker cone, when moving away from this line in the x-direction this remains reasonably constant for a minimum of 75 mm across frequencies, after which it drops of quickly. Therefore the w-velocity is phase averaged over this region and plotted in Figure 3.17a for $f = 30$ Hz, each datapoint representing 200 phase locked images. It shows that the velocity follows a sine wave of the same frequency as the electrical input signals, however with a large standard deviation at some parts of the phase. The velocity wave has a phase delay with respect to the input signal, this delay is highly frequency dependent and hard to estimate.

Random sampling was used to create the plot in Figure 3.17b, with $f = 65$ Hz. A total of 3000 images pairs were taken, which gives each of the 20 phase bins approximate 150 images. This number of images results in good convergence on the PIV data, as explained in Appendix B.2.5. It was observed that the standard deviation is lower at this frequency compared to $f = 30$ Hz, and the generated wave approximates a perfect sine wave more closely. The velocity amplitude is a considerably lower however, and the synchronization is not perfect on this measurement as there is a negative offset in the velocity wave. For the acoustic forcing measurements it was chosen to use random sampling based on these results, as the phase resolution is higher with no loss in accuracy. The random sampling measurements are also quicker to perform.

Speaker performance
The measured maximum amplitude for each frequency is shown in Figure 3.18a. This amplitude is calculated from fitting a sine wave to the phase averaged datapoints, as seen in Figure 3.17a. A clear peak velocity is visible at $f = 30$ Hz, which coincides with the resonant frequency of the speakers.
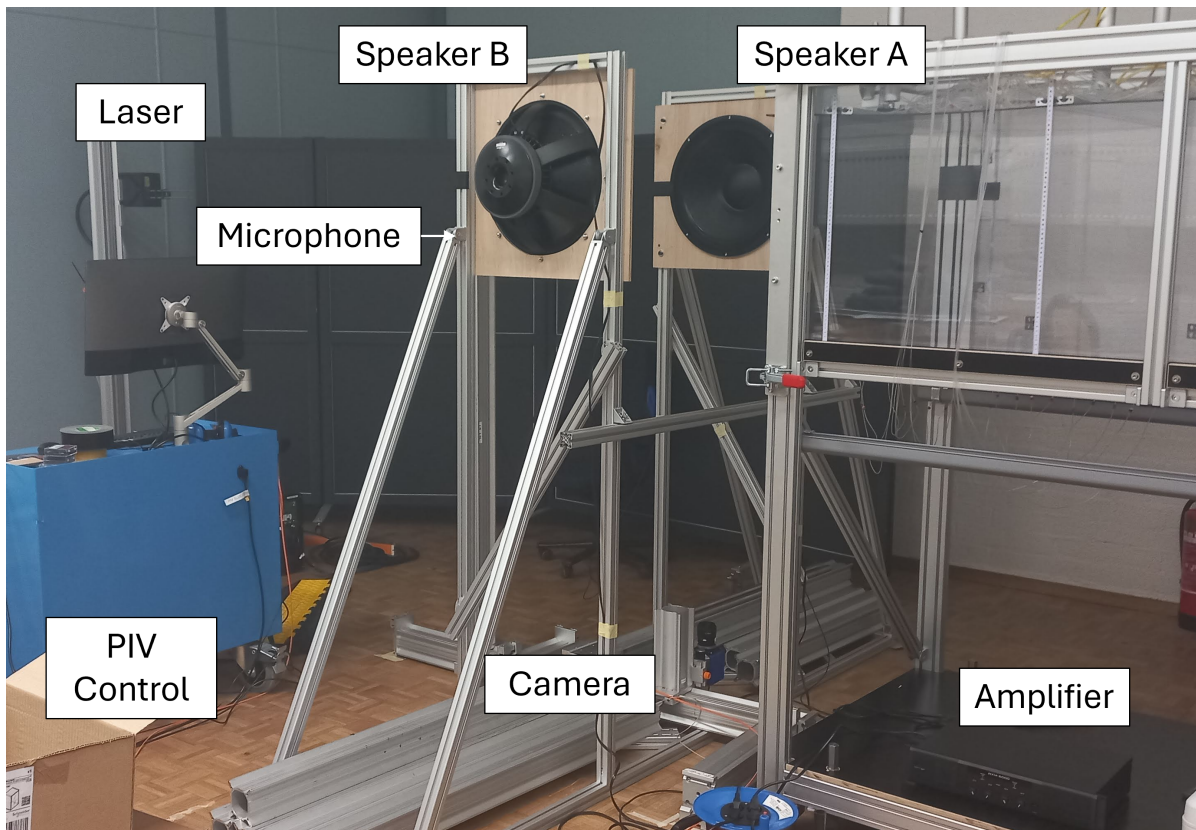
Figure 3.13: Overview of characterization test setup.

Using the friction velocity u_τ obtained from the DUBLF characterization, explained in Section 3.2.1, the forcing amplitude was estimated in wall units, shown in Figure 3.18b. The design frequency of $T^+ = 83$ is marked, and a maximum amplitude of $W_m^+ \approx 1.55$ is to be expected when the Re_τ is tuned to match the resonant frequency of the speaker. Therefore the design point was adjusted to $T^+ = 83$, $W_m^+ = 1.55$ with $Re_\tau = 1400$.
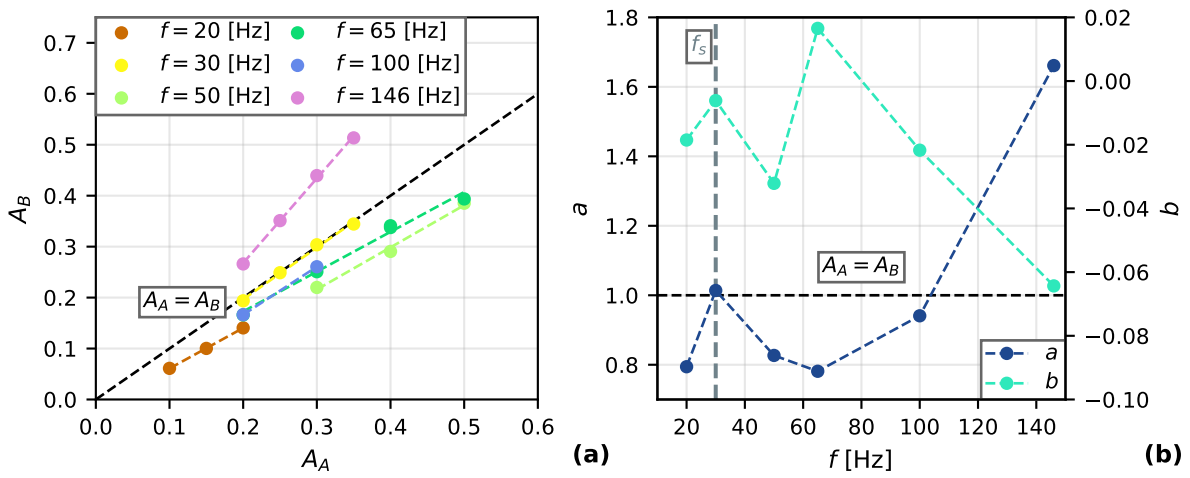
Figure 3.14: Required input amplitude A_{in} for each speaker to match the acoustic pressure measured by the microphone. On the left all measurements are shown and on the right the fit parameters for each frequency is plotted. The resonant frequency of the speaker f_s is marked.
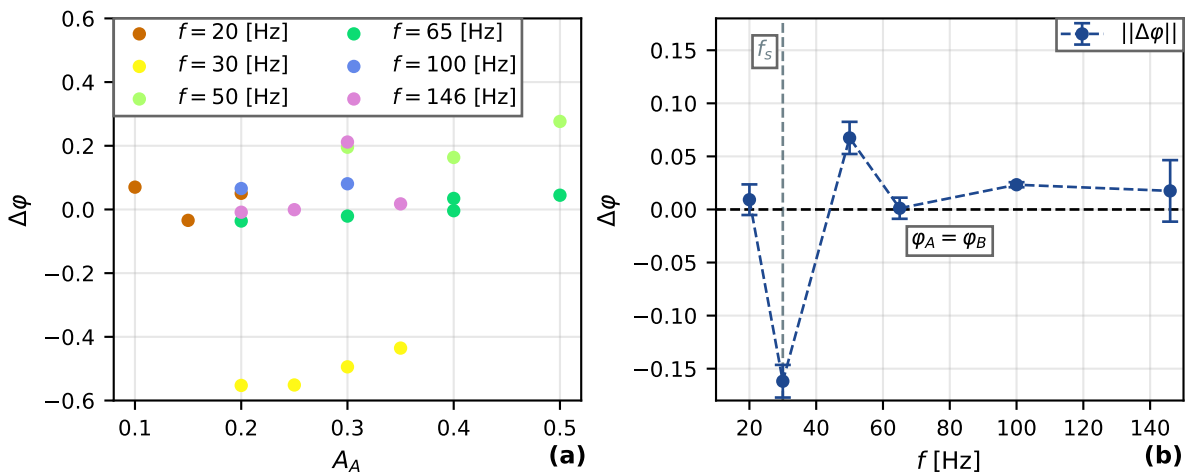
Figure 3.15: Required phase offset $\triangle\varphi$ for speaker B acoustic pressure to be exactly inverse of that of speaker A. The left plot shows all measurements on the f, A_{in} plane and the right plot is grouped by frequency. The resonant frequency of the speaker f_s is marked.
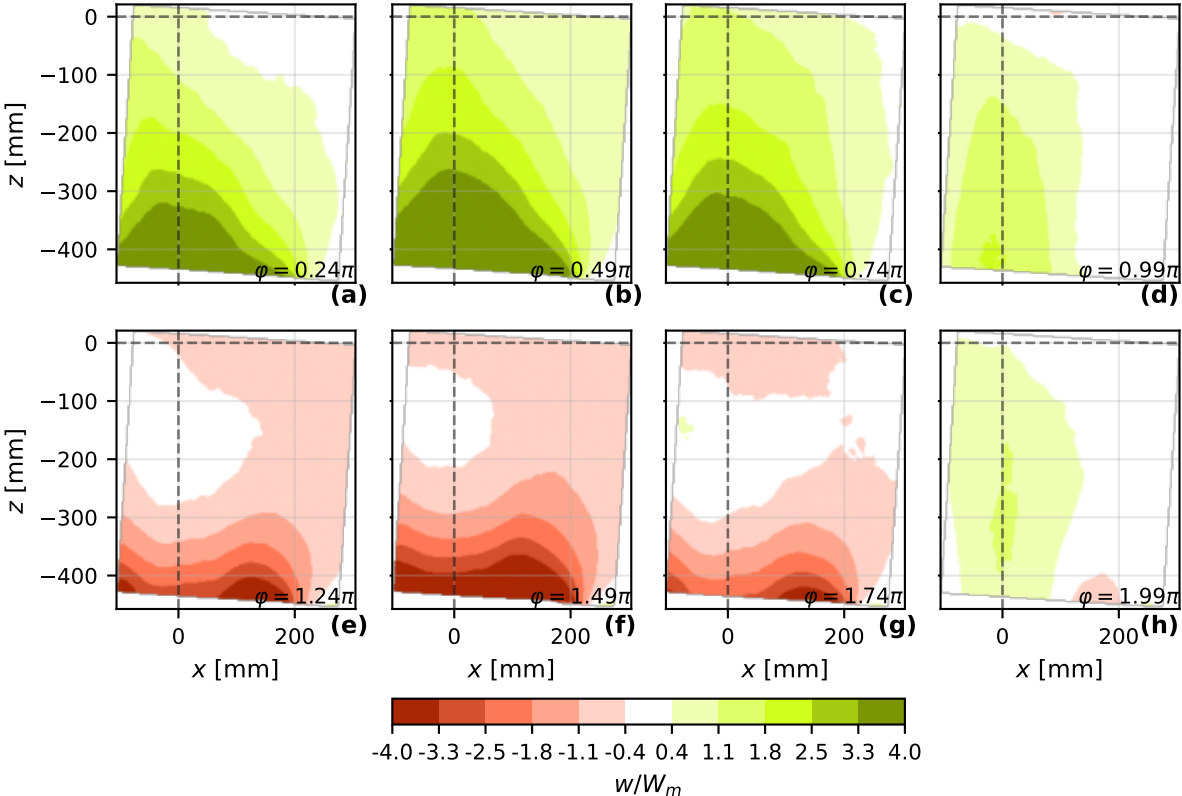
Figure 3.16: Phase averaged velocity field with $f = 30$ Hz and $W_m = 0.294$ m/s. The line at $x = 0$ denotes the speaker centerline and the line at $z = 0$ is the midpoint between the speakers. The front face of speaker A is at $z = -430$ mm.
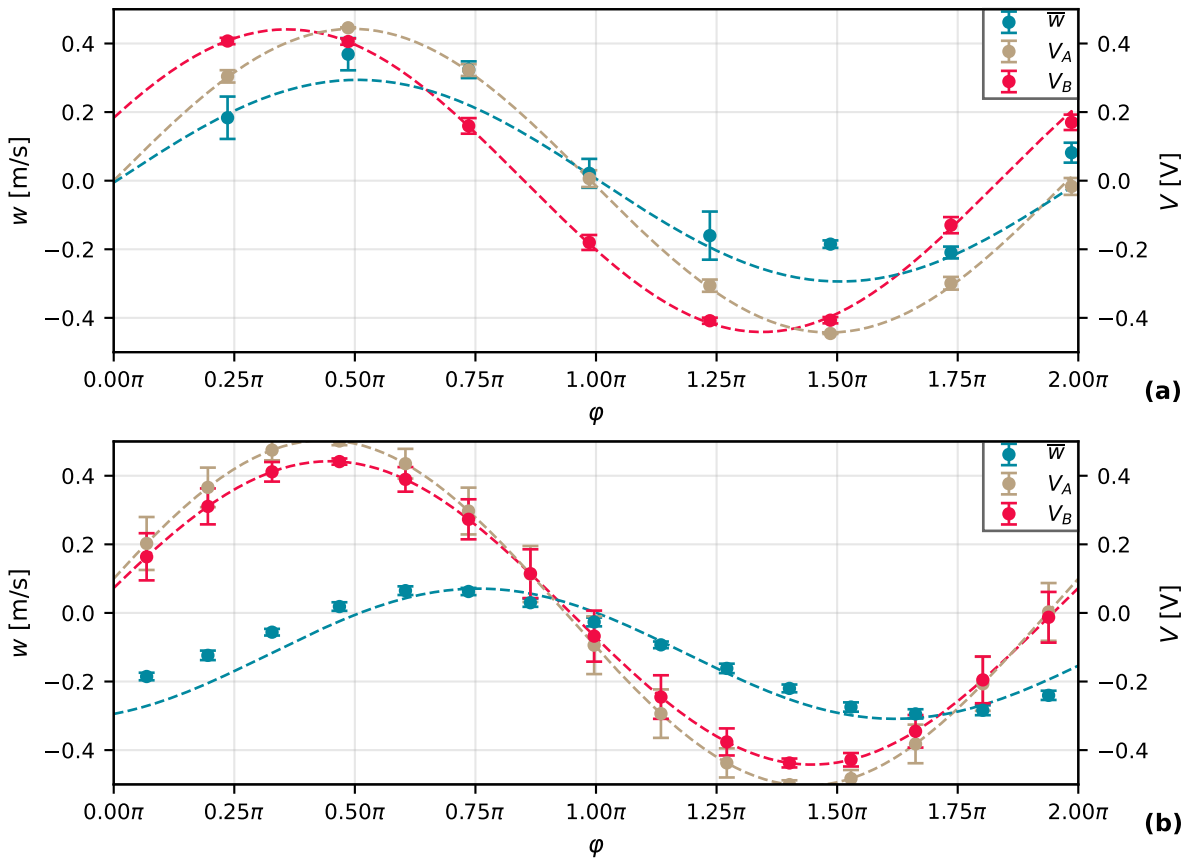
Figure 3.17: (a) Phase averaged speaker input signals V_A and V_B with $f = 30$ Hz, plotted together with the average velocity at the midpoint between the speakers with -75 mm $< x < 75$ mm. (b) Speaker input signals and average velocity of measurement with random sampling, then binned and averaged according to phase. Measurement with $f = 65$ Hz.
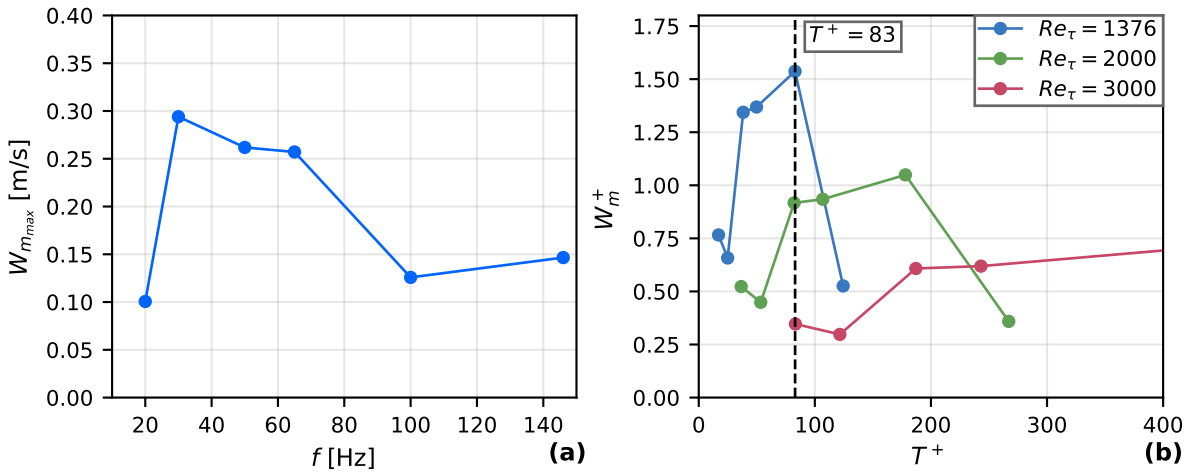
Figure 3.18: (a) Maximum achievable velocity amplitude at the midpoint between the speakers for the tested frequencies. (b) Maximum amplitude converted into wall units, based on the u_τ taken from the tunnel characterization, the design frequency is marked with the dashed line.

3.5. Experiment procedure

Each measurement followed the same procedure. First it was verified that all the equipment is switched on. The seeding of the room followed, where the smoke generator blows directly into the fan such that the wind tunnel distributes the seeding until the room is homogeneously seeded. Next the wind tunnel speed was adjusted to achieve the target U_∞, after this is stabilized a test image is taken using the PIV system. This test image is compared to an earlier reference to check the seeding density, and this is adjusted if needed. As soon as the seeding density is verified the measurement of the atmospheric conditions is started using the wind tunnel control computer, see Section 3.2.1. The next steps are performed in quick succession, to ensure that the data is captured at the same moment. First the speakers are switched on at their desired frequency and amplitude. The data acquisition is started as soon as the temperature, and thus the output, of the speakers is stabilized. This takes up to 30 seconds depending on frequency. The PIV recording is started immediately after the DAQ, during the acquisition process all the systems are monitored to spot any unexpected events quickly. After all the images are recorded everything is switched off.

The experiments were performed in multiple stages, outlined in the next sections. First the boundary layer was characterized. The characterization from Section 4.1 was used for an estimation of u_τ in the design phase, however, a bespoke characterization of the test was considered necessary since some modifications to the tunnel were done. The main experiments were done in batches, with the most important measurements first. Finally there were some extra measurements taken to support the conclusions drawn in this report.

3.5.1. Boundary layer characterization

The experiment started with the characterization of the boundary layer, indicated with numbers $3 - 6$ in Table A.1. The flow was visualised using the p120p PIV plane, which is located at $z = 0$ and uses a single camera to get the flow in the x and y direction. The FoV captured the centerline of the speakers and the area directly downstream of it, in which the FoV of the main measurements is also located. The only parameter that is changed between the measurements is the wind tunnel velocity, this enabled the measurements to be taken in quick succession. This also resulted in the atmospheric conditions to be the same for each run.

Later in the experimental campaign it was discovered that measurement 4 was done using the wrong Δt between the PIV images. Therefore it was decided to redo this measurement at the end of the campaign. Another intermediate step was also added, these measurements have numbers 74 and 75 respectively in Table A.1.

3.5.2. Acoustic tranverse forcing

With the boundary layer characterization complete the setup was changed to capture the p5020 PIV plane. This plane is a small region at $z = 0$ directly downstream of the speaker centerline, and captured using 2 cameras. As this stereo PIV setup was capturing double the amount of data as a planar setup it was chosen to crop the image in the y direction, capturing only the area of interest near the plate. These measurements correspond to numbers $8 - 65$ in Table A.1

Before the measurements were performed the speaker synchronization routine was done. In the speaker characterization test it was discovered that both speakers have a slightly different frequency response, see Section 3.4.2 for more information. The speaker synchronization was done using a microphone positioned in the midpoint between the speakers, see Figure 3.19 for an image of the synchronization setup. The sequence began with speaker A emitting the desired frequency and amplitude. Then speaker B was switched on at the desired frequency with the amplitude adjusted based on the characterization test. The phase delay was also set at the expected value. Then the amplitude of speaker B was adjusted to a slightly higher value. A python script then calculated the correct amplitude and phase delay of speaker B to attenuate the pressure wave of speaker A. Finally both speaker were switched on using the calculated settings, after which some minor adjustments were subsequently applied to further minimize the pressure signal measured by the microphone. At this point the speakers were moving exactly out of phase, maximizing the velocity amplitude in the test section. The microphone was removed before the PIV measurements started.
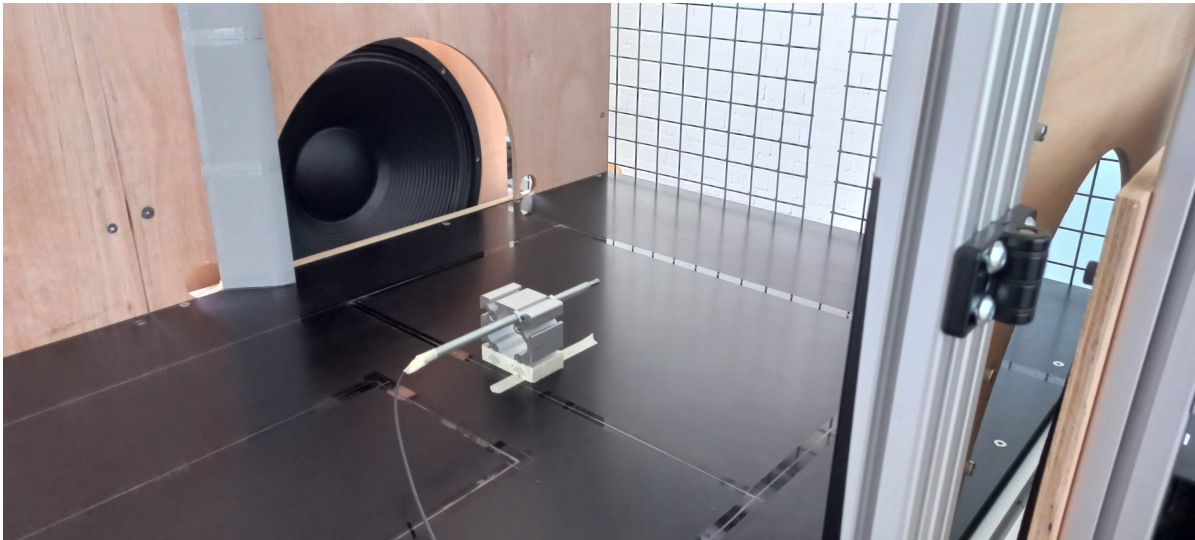
Figure 3.19: Photo taken from the speaker synchronization routine. Looking in the streamwise direction down the test section the microphone is seen mounted to a piece of aluminium. The painters tape is used to position it exactly in the midpoint between the speakers. Speaker A is located on the right just outside of the image and speaker B is seen on the left. The deflector next to the speaker opening and the mesh to provide a small positive pressure in the test section are also visible in this image.

Each measurement at a new wind tunnel speed started with a reference case. In this case the speakers were disabled, thus capturing the unforced case. The forced case, with the acoustic forcing applied, was captured directly afterwards, this ensured that the atmospheric conditions were the same for both cases. The number of images was usually double in the forced case to capture converged phase data. This exceeded the available memory of the acquisition computer and therefore these measurements were captured in two separate batches. It was ensured at each measurement that the reference unforced case and all forced batches were taken in quick succession, such that the atmospheric conditions are similar.

3.5.3. Extra measurements
A number of measurements were captured using the wall-parallel PIV plane wp260, which was located at a height of 2.5 mm from the flat plate. This enabled the visualisation of the transverse velocity field between the speakers, revealing the low-speed streaks near the wall. These measurements correspond to the numbers $70 - 73$ in Table A.1.

<div style="text-align: right;">

4

</div>

<div style="text-align: right;">

Results

</div>

This chapter presents the results of the experimental campaign. It will start with the boundary layer characterization in Section 4.1, the effects on the turbulent friction drag are explained in Section 4.2 and finally the observed changes in the velocity field are outlined in Section 4.3.

4.1. Boundary layer characterization

The unforced reference boundary layer was characterized using the p120p PIV plane, see Table 3.3 for more details. Figure 4.1 shows contours of the Boundary Layer (BL) at low and high Re_τ. The FoV for the p5020 plane is marked in these images, this is where the stereo measurements to determine the drag reduction were made. The progression of the boundary layer thickness δ_{99} is also visible in these images. A slight increase in BL thickness was observed over this streamwise length, this is likely an artifact of the flow deflectors along the speaker holes, see Section 5.1.1 for more details. The BL is assumed to be in equilibrium over the streamwise length of the p5020 PIV plane, as explained in Section 5.2.1.

Figure 4.2b shows the velocity profiles of a characterization measurement and a stereo measurement using the p5020 PIV plane at similar Re_τ. The profiles are averaged over the same x^+ range which corresponds to the p5020 PIV plane width. At $y^+ > 50$ the profiles show a perfect overlap, indicating that the boundary layer is consistent across measurements and that the 2 PIV methods show good correspondence. This confirms that the δ_{99} values obtained from the characterization are suitable for use in the stereo measurements. At lower y^+ the characterization measurement diverges from the stereo measurement. This is likely due to the proximity to the wall in that region, which is within a few interrogation windows. However, for the characterization this is not considered as the region of interest.

Section 4.1.1 details the boundary layer thickness and shape, Section 4.1.2 contains information on the turbulence statistics in the reference boundary layer. More details about the development of the boundary layer are found in Section 4.1.3. Contour plots of all measured Re_τ, the corresponding velocity profiles and turbulence statistics can be found in Appendix C.2.

4.1.1. Boundary layer thickness

As explained in the previous section there is a slight decrease in boundary layer thickness in the streamwise direction. Therefore the velocity profiles are averaged over the length of the p5020 FoV as this is the area of interest. This reduces the effects of the non-uniformity of the boundary layer to a minimum.

The boundary layer thickness δ_{99} is defined by the height from the plate where the velocity is 99% of freestream velocity U_∞. This value is also used in the definition of Re_τ. At low $Re_\tau < 1500$ the $\delta_{99} \approx 103$ mm, at higher Re_τ the thickness decreases to a minimum of $\delta_{99} = 96.7$ mm, as seen in Figure 4.2a. The boundary layer momentum thickness δ_2 is defined by

$$\delta_2 = \int_0^\infty \frac{u(y)}{U_\infty}\left(1 - \frac{u(y)}{U_\infty}\right) dy \tag{4.1}$$

<div style="text-align: center;">

39

</div>
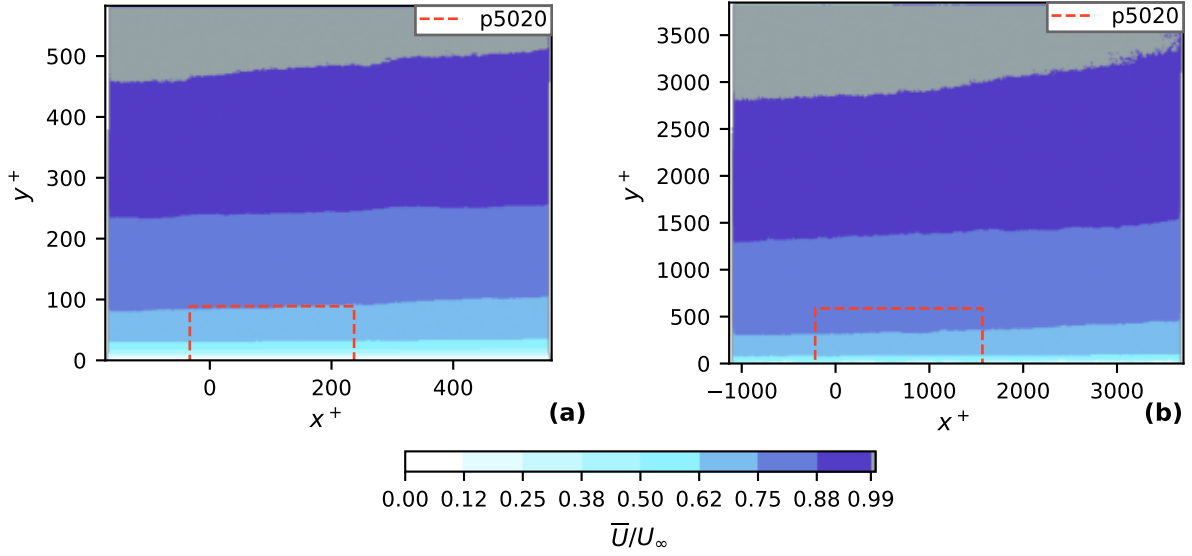
Figure 4.1: Velocity magnitude of boundary layer for (a) $Re_\tau = 491$ and (b) $Re_\tau = 3036$. The FoV for the SPIV measurements is marked.

and ranges from 11.6 mm at low Re_τ to 10.4 mm at high Re_τ.

4.1.2. Turbulence statistics

The 2-dimensional Reynolds stresses are calculated using the fluctuating components of the flow u' and v', which are calculated using $u_i' = u_i - \overline{u}_i$, with u_i the instantaneous velocity component and $\overline{u}_i$ the averaged velocity component over the full measurement. The magnitude of the Reynolds stresses are larger for high Re_τ, as seen in Figure 4.3a. The evolution of the Reynolds stresses in the wall normal direction is similar to that of DNS results [32].

The contribution of the production $\mathcal{P}$ and dissipation ε terms of the Turbulence Kinetic Energy (TKE) transport equation are shown in Figure 4.3b. These two terms are selected as they are the biggest contributors, all terms are shown in Appendix C.2.2. At low y^+ both terms are larger in absolute magnitude for low Re_τ, however, the terms might be unresolved in the high Re_τ case as the interrogation window size imposes a low pass filter. The half interrogation window size is not shown in Figure 4.3 as it is lower than the left y^+ boundary. The method for extracting these terms is explained in Appendix B.2.4.

4.1.3. Boundary layer development

Further investigation was done into the development of the boundary layer, as it was noted that it is not perfectly constant. The boundary layer velocity profile is averaged over 2 separate regions, near the upstream edge and the downstream edge of the FoV, as shown in Figure 4.4a. The extracted velocity profiles are shown in Figure 4.4b. A slight offset in velocity can be observed, with a higher velocity at the downstream end. This also increases the boundary layer thickness δ_{99} by 0.68%, from $\delta_{99}^+ = 1428$ to $\delta_{99}^+ = 1438$, in the streamwise direction. This negative streamwise velocity gradient is most likely attributed to the deflectors along the speaker openings, as explained in Section 5.1.1. The Reynolds stresses also have a variation along the streamwise direction, shown in Figure 4.4c. Downstream of the speaker centerline the $\langle u'u' \rangle$ and $\langle v'v' \rangle$ components are lower. The dissipation and production terms of TKE transport equation are also lower as a result, shown in Figure 4.4d. All profiles shown in Figure 4.4 have been non-dimensionalised using an average value for u_τ based on the stereoscopic PIV done using the p5020 plane. The actual u_τ in the downstream region is most likely lower due to the progression of the boundary layer, explaining the difference in the profiles observed. Most of the dissipation occurs at the small scales, which are not fully resolved due to the PIV resolution, therefore the dissipation is likely underestimated. The absolute values should therefore be regarded with caution, however, the difference between measurements is still of interest.
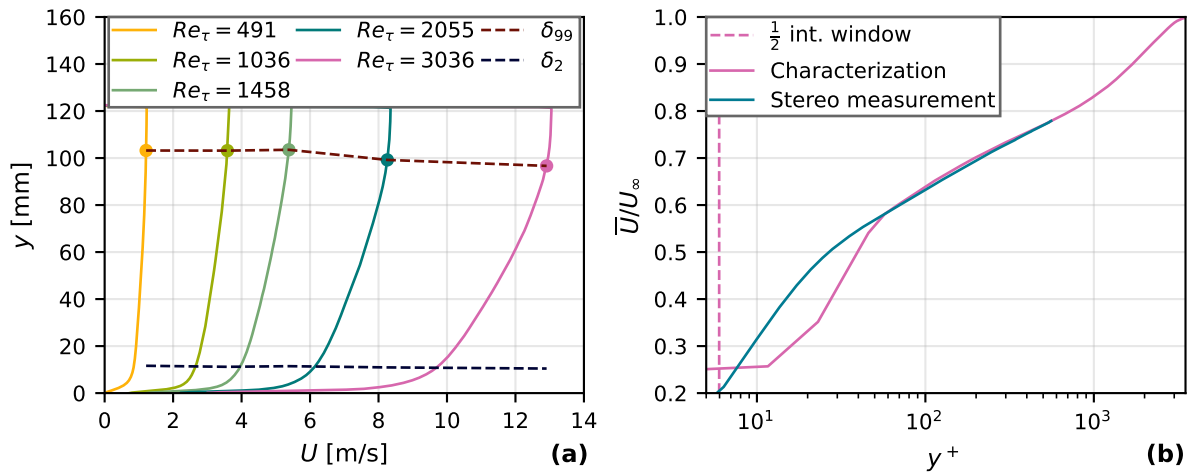
Figure 4.2: (a) Boundary layer thickness and momentum thickness for different Re_τ. (b) Comparison between a BL characterization measurement with $Re_\tau = 3036$ and a SPIV measurement with $Re_\tau = 3023$.
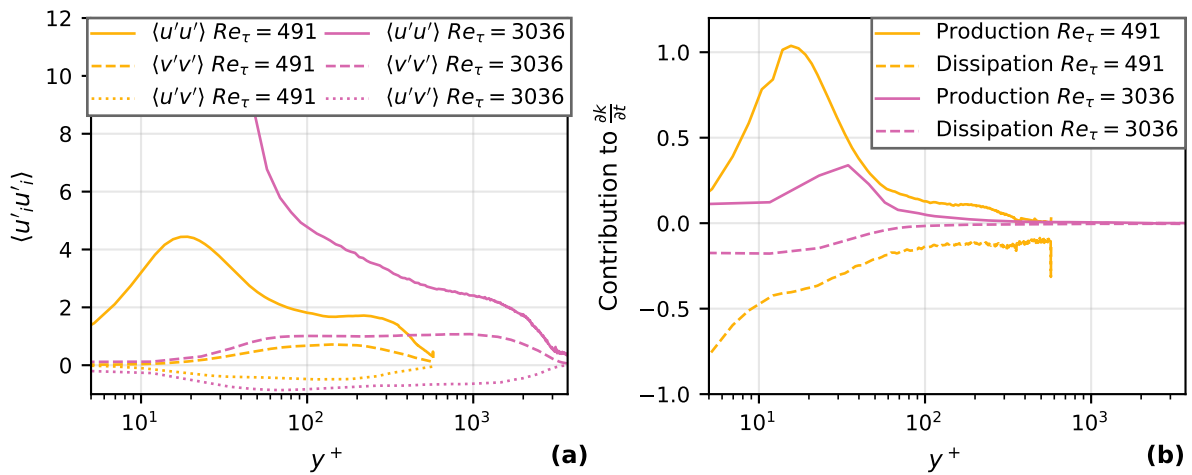
Figure 4.3: (a) Reynolds stresses in the BL for low and high Re_τ. (b) Production and dissipation terms of the turbulence kinetic energy budget for low and high Re_τ.
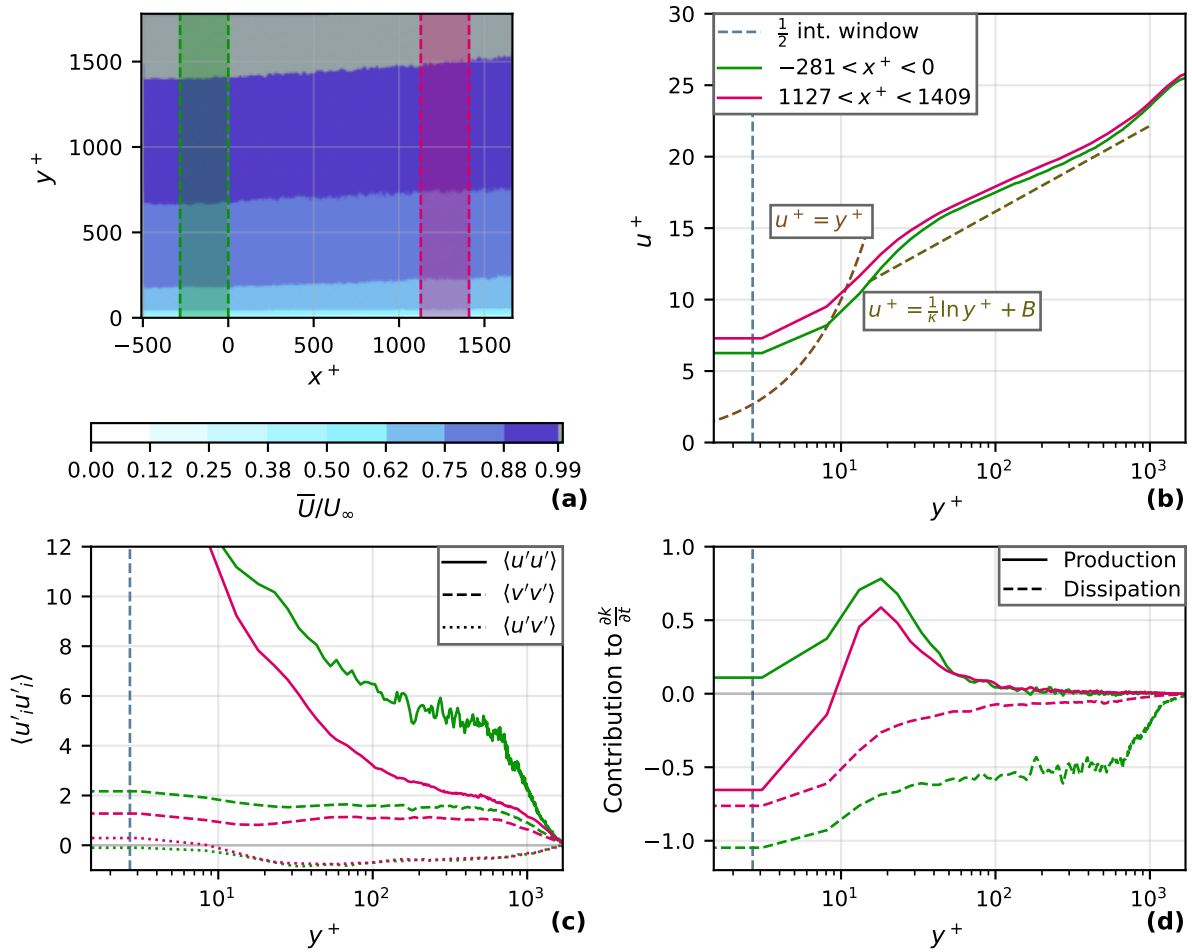
Figure 4.4: Development of the boundary layer with $Re_\tau = 1458$, (a) shows the areas in which the other variables are averaged, (b) shows the velocity profiles, (c) the Reynolds stresses and (d) the production and dissipation terms of the TKE budget.

4.2. Acoustic transverse forcing

The results of the friction drag reduction measurements are described in this section, they are processed using the method given in Section 3.3.1.

Two series of measurements were taken at maximum amplitude and a constant forcing period, $T^+ = 83$ and $T^+ = 100$ and are found in Section 4.2.1. Another series of measurements was done with the period and amplitude constant, to isolate the effect of Reynolds number, this is described in Section 4.2.2.

4.2.1. Constant period

The experimental setup was designed for the forcing parameters of $T^+ = 83$ and $Re_\tau \approx 1500$, with W_m^+ as large as the equipment would allow, as explained in Section 3.4.3. Since the setup can change these parameters with minimal effort a range of measurements was done at $T^+ = 83$. The results are shown in Figure 4.5a, with the velocity profile in the viscous sublayer of the design point from Section 3.4.3 in Figure 4.5b. The actual period was $T^+ \approx 100$ due to the deflector influence, see Section 5.1.1 for more details. This period does correspond to the optimal period found by Quadrio et al. [5]. The velocity profiles corresponding to all the measurements can be found in Appendix C.3.1. A drag reduction $\mathcal{R} = 4.77\%$ with an standard error of 13.4% was found at the design point, with $W_m^+ = 1.40$, $T^+ = 97.2$ and $Re_\tau = 1441$. Interpolating the map of $\mathcal{R}$ on the $W_m^+ - T^+$ plane in Figure 1 of the DNS study by Quadrio and Ricco [5], shown in Figure 2.12 gives $\mathcal{R} \approx 3.0\%$ at the same T^+ with $W_m^+ = 1.8$. A direct comparison can not be made however, as the amplitude is slightly higher and the map is with $Re_\tau = 200$.

A better comparison can be made using the measurement at $Re_\tau = 1847$, here the flow is forced with a period $T^+ = 95.2$ and $W_m^+ = 1.10$. This resulted in a drag reduction $\mathcal{R} = 6.02\%$ with a standard error of 7.78%. Gatti et al. [14] found $\mathcal{R} = 12.5\%$ with $T^+ = 83$ and $Re_\tau = 2000$. The drag reduction they found was approximately double, however, their amplitude was higher at $W_m^+ = 5$. The drag reduction values found are of similar order of magnitude, but can not be directly compared due to the difference in forcing parameters. The streamwise length of the forced area is difficult to determine as there is no well defined boundary. The area where the velocity is at its maximum is $x/\delta \approx 1.2$. It is likely that the drag reduction has not reached it maximum potential within this length, explaining part of the difference. Other factors might be the slight positive pressure gradient or inaccuracies in the experimental method. Further measurements must be done to get a direct comparison.

At the lowest $Re_\tau = 1192$ a drag reduction $\mathcal{R} = 5.79\%$ was found with a standard error of 19.3%. The forcing parameters $T^+ = 95.3$ and $W_m^+ = 1.18$ were used. Yao et al. [33] found an $\mathcal{R}$ of 25.9% with $Re_\tau = 1000$, $T^+ = 90$ and $W_m^+ = 12$ using a DNS channel flow. Touber and Leszchiner [31] have a similar result with $\mathcal{R} = 29\%$ at $T^+ = 100$, using the same W_m^+ and Re_τ and also running a DNS channel flow simulation. Experimental data on an oscillating wall from Gouder et al. [27] with at $Re_\tau = 1025$ and forcing parameters $W_m^+ = 11.4$, $T^+ = 90$ shows a $\mathcal{R} = 16\%$. The results of these studies show that if a higher W_m^+ can be achieved the drag reduction will be more significant.

At higher Re_τ the drag reduction found decreases and at $Re_\tau = 3023$ there is a drag increase due to the forcing. This is likely a result of the waveform not being symmetrical, as seen in Figure 4.10a. With an asymmetrical waveform the forcing conditions are removed from the optimal, and therefore the main effect of the speakers is an increase in turbulence intensity. This results in a higher friction drag.

The optimum forcing period was determined to be at $T^+ = 100$ by Quadrio et al. [5]. Therefore a series of measurements at that period were done at maximum amplitude, their results shown in Figure 4.6. The resulting period was higher due to the deflectors at $T^+ \approx 120$. The velocity profiles corresponding to these measurements can be found in Appendix C.3.1. The peak drag reduction was at $Re_\tau = 1575$ with $\mathcal{R} = 2.80\%$. The drag reduction is significantly lower as in the measurements with a lower period, which is to be expected as the period in these measurements diverges from the optimum. At $Re_\tau = 2067$ a drag reduction of $\mathcal{R} = 2.73\%$ was found, with a period $T^+ = 120.5$ and amplitude $W_m^+ = 1.04$. Yao et al. [33] found $\mathcal{R} = 22\%$ at $T^+ = 100$ and $W_m^+ = 12$ using a DNS channel flow. Gatti et al. [14] found $\mathcal{R} = 9.5\%$ with $T^+ = 138$ and $W_m^+ = 5$ at the same Re_τ. These results reiterate the point that there is a lot more drag reduction to be found if the amplitude is increased and the period is optimal. Increasing the streamwise length of the forced region could also bring the results closer to that found
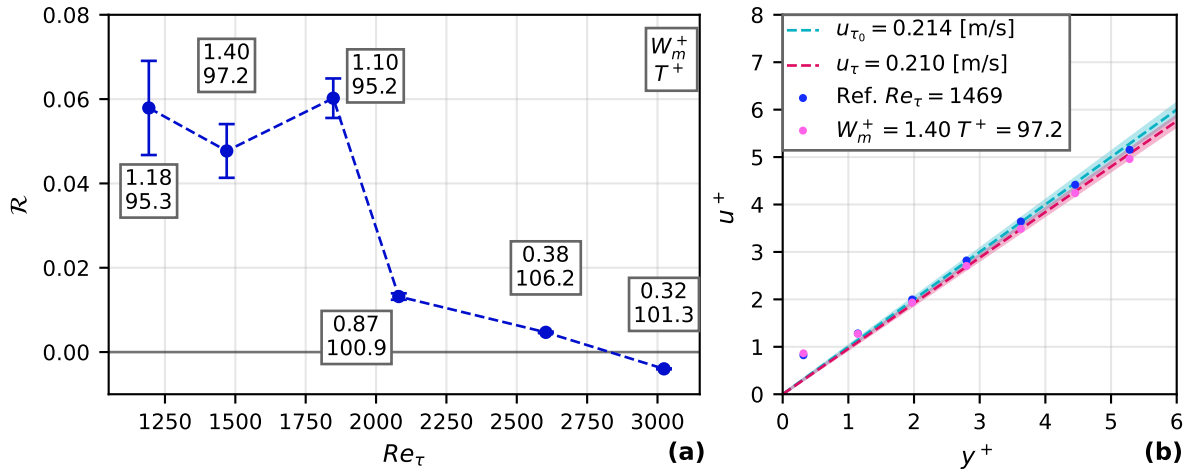
Figure 4.5: (a) The resulting drag reduction $\mathcal{R}$ for all measurements with $T^+ \approx 95$, with their standard error. (b) The $u^+ - y^+$ velocity profile of the measurement at the design point. The shaded area marks the standard error of u_τ.

in DNS studies.

4.2.2. Reynolds number dependence

One of the main open questions currently is the extrapolation of the drag reduction effect to higher, practical friction Reynolds numbers, see Section 2.2.3. The forcing method of the current research was in part developed to help answer this question. To test if future researchers can use this method to study this effect a series of measurements was done with the optimal period [5] $T^+ \approx 100$ and $W_m^+ \approx 0.80$ at different Re_τ. The actual period was higher at $T^+ \approx 120$ due to the effect of the deflector, see Section 5.1.1.

The results are shown in Figure 4.7. The drag reduction starts at 6.83% at low Re_τ and drops at higher Re_τ. The low absolute drag reduction is due to the low amplitude, this was chosen such that the setup could reach this value at each measurement. The relative drag reduction is of interest in this series of measurement, as $\mathcal{R}$ decreases with higher Re_τ while the forcing inputs stay relatively stable. The higher $\mathcal{R}$ in the first measurement is likely a result of T^+ being closer to the optimum. The resulting slope is likely not a perfect indication of the $\mathcal{R} - Re_\tau$ trend, there could be other factors influencing the result due to the experimental limitations of the current setup. More work is needed to get a definitive answer to this question, however, this result does prove that researching the Re_τ trend is possible using a similar setup to the current work because the forcing parameters can be kept stable at different Re_τ.
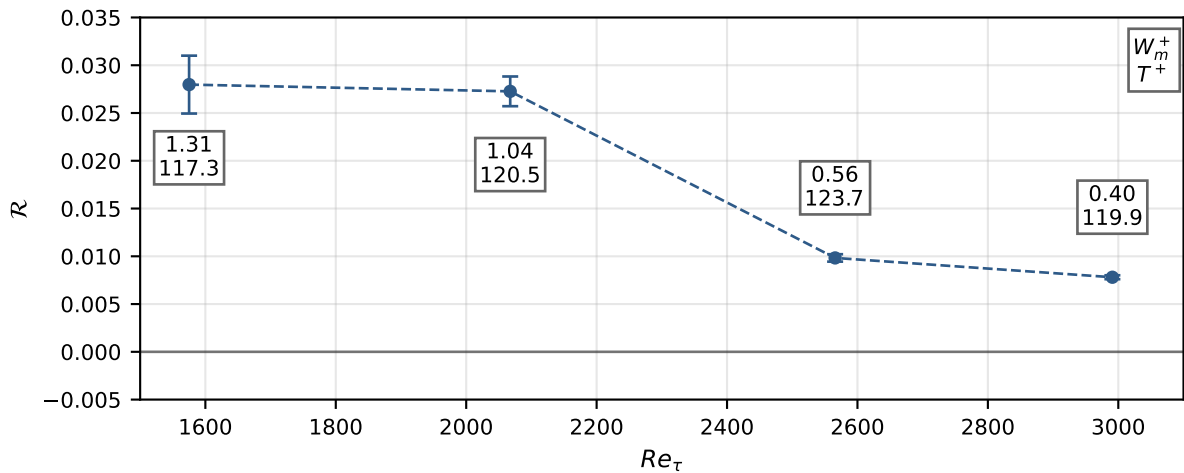
Figure 4.6: The resulting drag reduction $\mathcal{R}$ for all measurements with $T^+ \approx 100$, with their standard error.
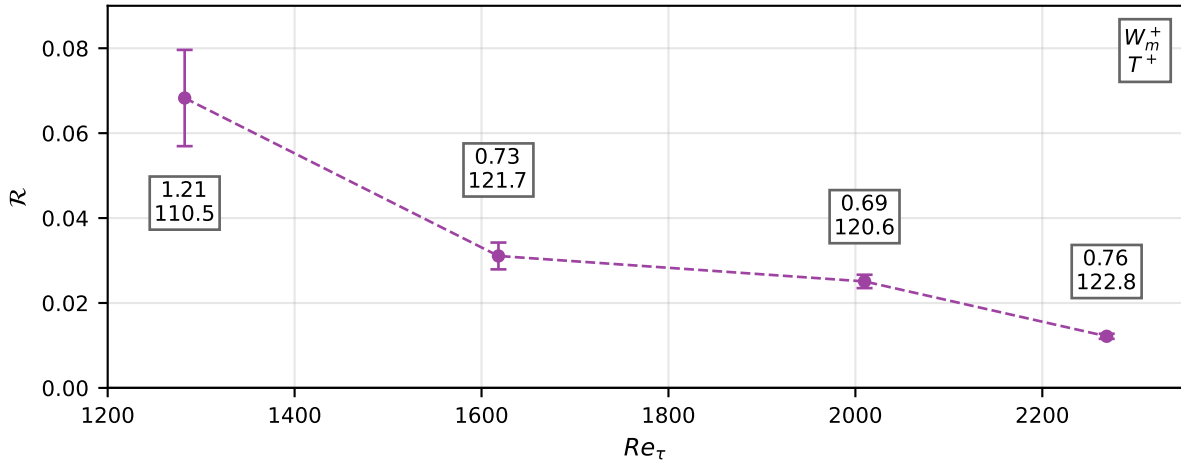
Figure 4.7: The resulting drag reduction $\mathcal{R}$ for a series of measurements with $T^+ \approx 100$ and $W_m^+ \approx 0.80$, with their standard error.

4.3. Effects on velocity field

The effects of the acoustic transverse forcing on the velocity field in the test section are described in this section.

Four indicator were investigated, Section 4.3.1 outline the velocity profiles in the boundary layer, Section 4.3.2 the transverse velocity, Section 4.3.3 describes the effect on the Reynolds stresses and Section 4.3.4 the changes to the components of the TKE transport equation.

4.3.1. Velocity profiles

The profile of the streamwise velocity u^+ in the wall normal direction y^+ is a direct indicator of the effect of flow control methods with the intention of reducing turbulent friction drag. The friction velocity u_τ is derived from this profile and is used directly for calculating the drag reduction, see Equation 3.10 and 3.11.

Figure 4.8a shows the streamwise velocity profiles of the measurement pair at $Re_\tau = 1192$. The forced case resulted in a drag reduction of $\mathcal{R} = 5.79\%$. The reference profile adheres to the $u^+ = y^+$ rule in the laminar sublayer for $y^+ < 5$, after which it starts to diverge. The forced case has a lower slope, as the u_τ is lower due to the effects of the forcing, as intended. In the buffer layer the profiles do not exactly follow the log-law, with $\kappa = 0.384$ and $B = 4.17$. The slight development of the boundary layer and positive pressure gradient is likely the cause of this. The proposed mechanisms for the drag reduction are mainly in the viscous sublayer and the lower part of the buffer layer, see Section 2.2.4. Therefore the drag reduction values are still considered valid in the context of this research. The streamwise velocity over the full measurement domain, $y^+ < 110$ in this case, is slightly lower when the forcing is applied, resulting in a different boundary layer shape. The streamwise velocity profiles of all measurements can be found in Appendix C.3.1.

4.3.2. Transverse velocity

The ideal shape for transverse forcing signal is a sine wave centred around 0 [23]. Therefore the input signals to the speaker must be tuned such that they move exactly out of phase, see Section 3.4.2. With the stereo PIV setup the transverse, out of plane velocity can be extracted, with lower accuracy than the streamwise and wall-normal components. From this velocity conclusions about the effectiveness of the forcing can be drawn.

For each forced measurements 3000 image pairs at were taken, these were sorted according to phase in 20 bins of 150 images each, see Appendix B.2.5 how these values were chosen. The transverse velocity w^+ profile for each of these phase instances was found by taking the average in time and along the streamwise direction. These profiles at peak amplitude are shown in Figure 4.10b. As the Re_τ of the transverse flow is lower than that of the main flow the boundary layer is thin, and at $y^+ > 30$ the
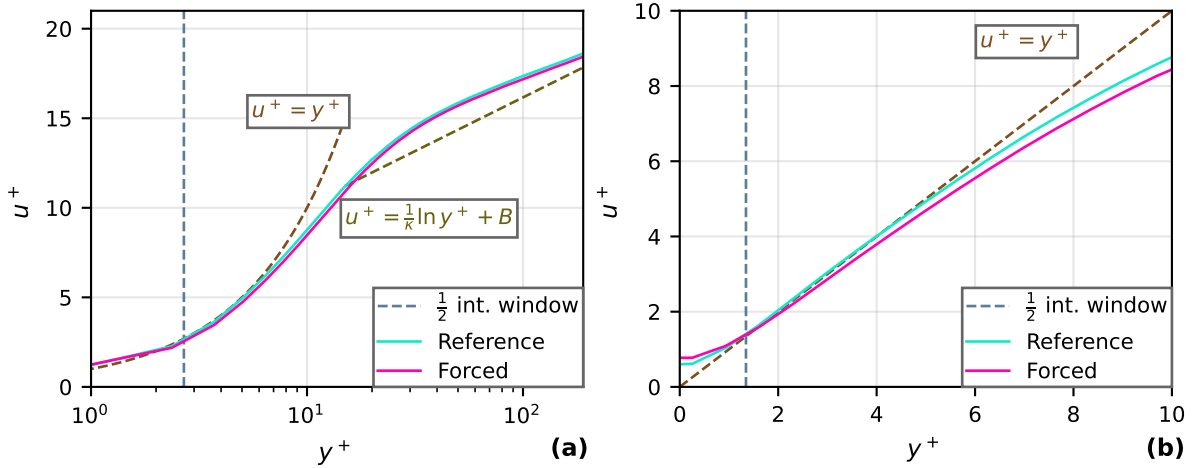
Figure 4.8: (a) Boundary layer velocity profile for the reference flow with $Re_\tau = 1161$ and the same flow with transverse forcing, $W_m^+ = 1.18$ and $T^+ = 95.3$, applied. The controlled flow has a $\mathcal{R} = 5.79\%$. (b) Detail of the viscous sublayer.

w^+ is constant. To calculate the forcing amplitude W_m^+ the w^+ was averaged in this constant region, shown for $Re_\tau = 1161$ in Figure 4.9a. A sine wave is fitted to the resulting signal, and the amplitude of this wave is taken as the forcing amplitude, $W_m^+ = 1.18$ in this case. The offset of the wave is $0.0084 \cdot W_m^+$, indicating that the speakers are correctly synchronized. The average w^+ over the phase for the other measurements with $T^+ \approx 100$ are shown in Figure 4.10a. The offset of the wave is larger for some measurements, especially at higher Re_τ. This leads to the conclusion that a better method for synchronizing the speakers is needed, as this has a negative impact on the drag reduction.

The transverse velocity profiles at various parts of the phase for $Re_\tau = 1161$ are shown in Figure 4.9b. This measurement was picked to show in detail as the velocity in the near wall region, $5 < y^+ < 20$ is significantly higher than further from the wall. This effect was only observed at low Re_τ, where the speaker is operating below its resonant frequency. A possible explanation might be that the velocity jet diffuses from the speaker centerline and then gets diverted by the plate as it moves in the transverse direction towards the midpoint between the speakers. However, further research is needed to get a definitive answer. The higher velocity near the wall does likely influence the drag reduction in a positive manner, as the amplitude and transverse shear is higher in the most sensitive region.

The transverse velocity profiles for the other measurements with $T^+ \approx 100$ are shown in Figure 4.10b. They all monotonically increase moving away from the wall, with the exception of the aforementioned measurement at $Re_\tau = 1161$. Some profiles show a negative velocity directly at the wall. This might be attributes to hysteresis due to imperfect synchronization. However, as the accuracy of the out of plane velocity component is low in this region this might also be an artifact of the PIV processing. The transverse velocity profiles of all measurements can be found in Appendix C.3.2.

Comparison to Stokes' theory
With conventional transverse forcing using wall motion the w-velocity profile can be described using the Stokes layer [45], given by Equation 2.15. The w profiles for several different parts of the phase given by this equation are shown in Figure 4.11 with dashed lines. The solid lines are w profiles taken from the measurement with $Re_\tau = 1790$, with the amplitude W_m subtracted to reverse the reference frame from forcing the fluid to wall motion. The profiles in the positive direction are similar to the theoretical Stokes' profiles, with minor deviation. In the negative direction large deviations are found. This corroborates the asymmetry of the forcing velocity found in many of the measurements, which is an effect of imperfect speaker synchronization. The other measurements show similar results to the one shown. It is likely possible to match all profiles to the theoretical Stokes' profiles with careful tuning of the experimental setup.
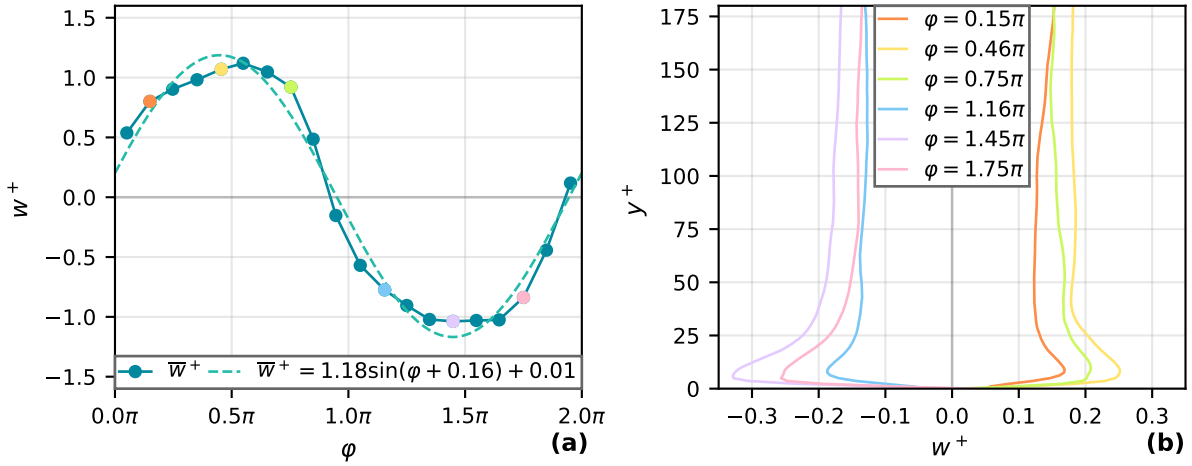
Figure 4.9: (a) w^+ velocity averaged over $y^+ > 30$ with $Re_\tau = 1161$ and $T^+ = 95.3$. (b) w^+ velocity profiles at various parts of the phase, the line colors correspond to the marked points in (a).
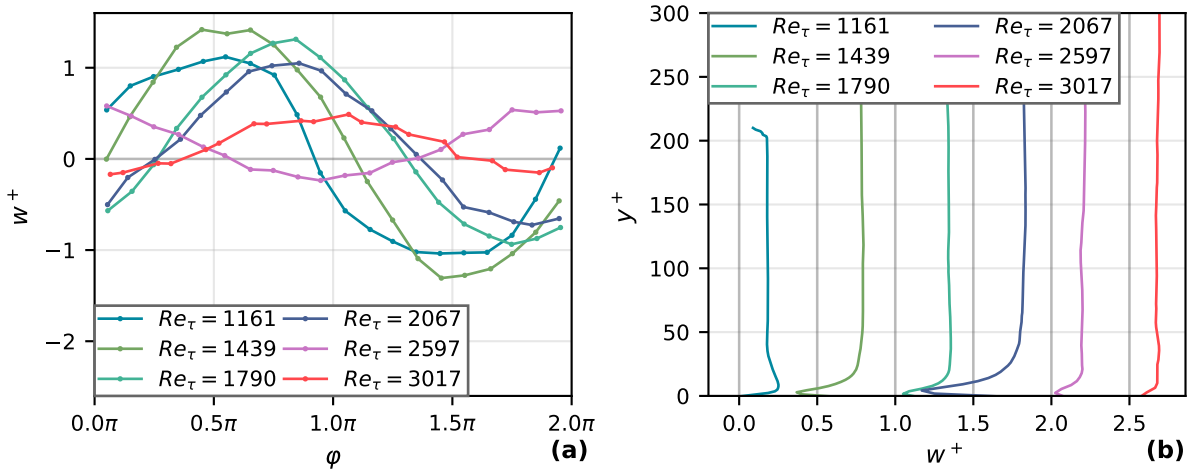
Figure 4.10: (a) w^+ velocity averaged over $y^+ > 30$ for various Re_τ with $T^+ \approx 100$. $\varphi = 0$ denotes the zero-crossing of the electrical signal to speaker A. (b) w^+ velocity profiles at peak amplitude for various Re_τ, spaced apart by $w^+ = 0.5$.

4.3.3. Reynolds stresses

The Reynolds stress tensor is calculated by taking the square of the velocity components and averaging these for the full measurement. "The Reynolds stress plays a crucial role in turbulent flows because it represents the rate of mean momentum transfer by turbulent fluctuations" [57]. The effect of the forcing on these stresses is therefore important to understand, as it might indicate towards the underlying aerodynamic mechanism.

Figure 4.12 shows a selected set of Reynolds stress tensor components, the components in the principal directions, $\langle u'u' \rangle$, $\langle v'v' \rangle$ and $\langle w'w' \rangle$, are chosen to illustrate the magnitude of the fluctuations. The $\langle u'v' \rangle$ component is shown because it is the largest contributor to the production of turbulence, based on Equation B.3 and given that $\frac{\partial u}{\partial v}$ is large near the wall. The stresses shown are calculated from the measurement at $Re_\tau = 1192$, the solid line corresponds to the reference case and the dashed line to the forced case. A shift of $\langle u'u' \rangle$ in the wall-normal direction is observed, indicating that the fluctuations in the streamwise direction are reduced in the near wall region at $y^+ < 15$. The forced case has a large increase in $\langle w'w' \rangle$, this is because the transverse forcing velocity is included in the fluctuations. The Reynolds stresses for the other measurements can be found in Appendix C.3.3.
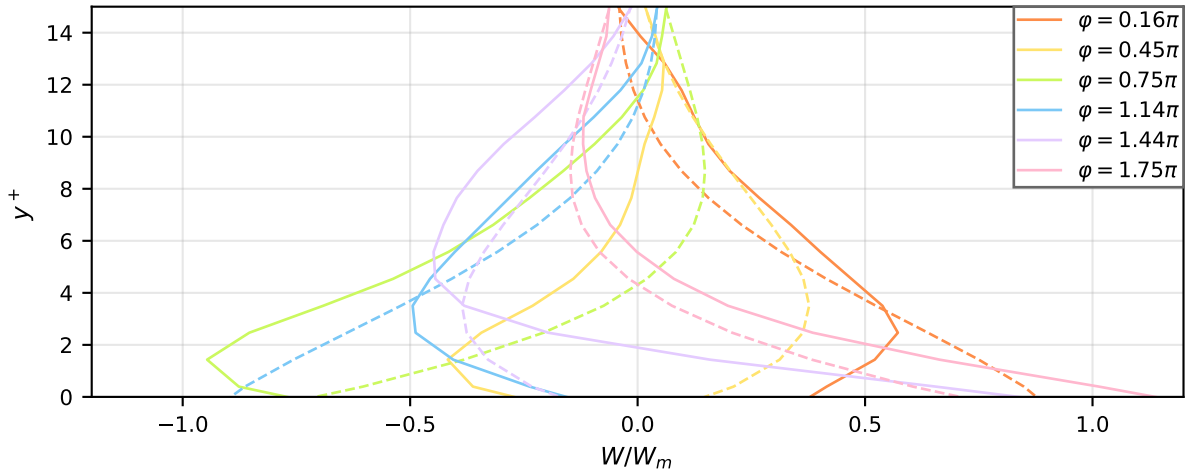
Figure 4.11: Transverse w-velocity profiles with the amplitude W_m subtracted from the measurement at $Re_\tau = 1790$. The dashed lines show the profile given by Stokes' theory for a conventional transverse forcing case with wall motion at the same conditions.
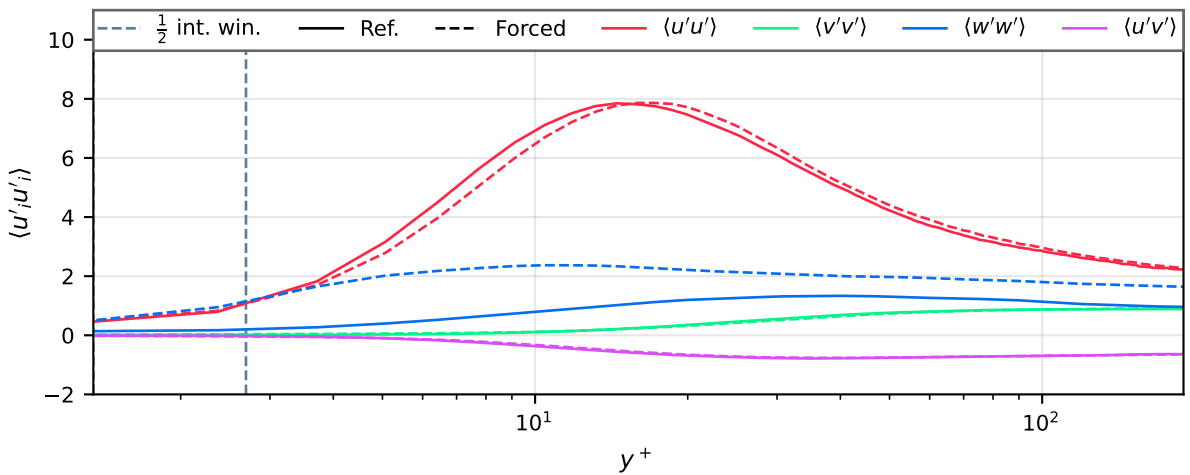
Figure 4.12: Reynolds stresses averaged in the streamwise direction. The reference flow has $Re_\tau = 1192$ and the forced case has $W_m^+ = 1.18$ and $T^+ = 95.3$ as input parameters.

4.3.4. Turbulence kinetic energy

The turbulence kinetic energy (TKE) transport equation, see Equation B.3, can be subdivided into several components. Each of these components has their own influence on the change in TKE, and the transverse forcing effects these components in different ways. Figure 4.13 shows the average of the TKE components along the wall-normal direction for $Re_\tau = 1192$. The pressure transport term is omitted because this requires the pressure fluctuations to be known, due to the deflector influence there is a slight pressure gradient and therefore the pressure can not be accurately derived from the PIV data, see Section 5.1.1. The TKE components of the other measurements can be found in Appendix C.3.3. The three measurements with $Re_\tau = 1192$, $Re_\tau = 1496$ and $Re_\tau = 1847$, all with $T^+ \approx 95$ and $\mathcal{R} \approx 5.50\%$, show a similar change in the TKE components when the forcing is applied. There is a slight reduction in turbulence production in the near-wall region, with $y^+ < 30$. The turbulent convection is greatly reduced in the viscous sublayer, both these effects reduce the amount of turbulence produced. The most significant contributor is the increase in dissipation along the whole measured area. It is still unknown if the reduction in TKE through the modification of aforementioned components is an effect of the drag reduction or the other way around.
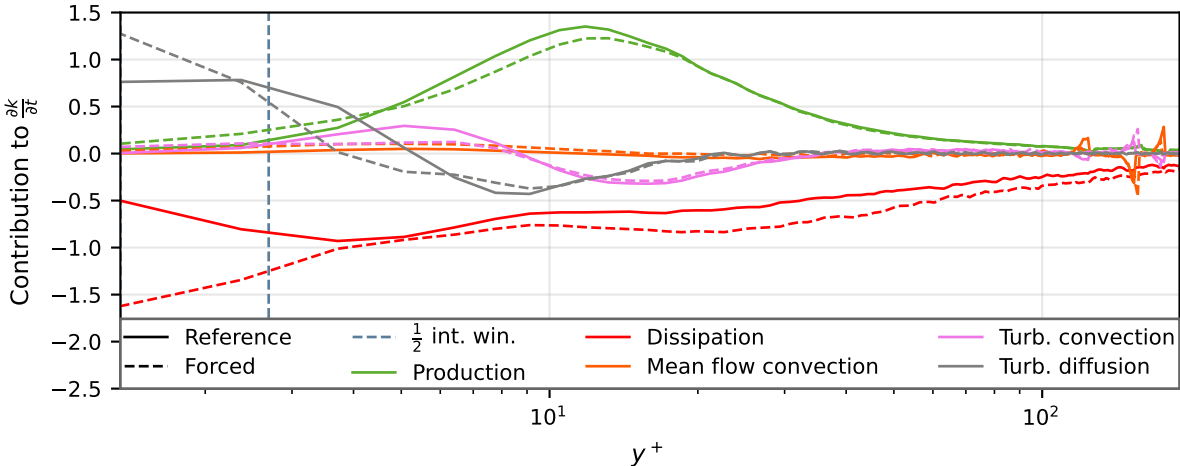
Figure 4.13: Turbulence kinetic energy budget averaged in the streamwise direction. The reference flow has $Re_\tau = 1192$ and the forced case has $W_m^+ = 1.18$ and $T^+ = 95.3$ as input parameters.

Discussion

This chapter will provide an overarching discussion on the accuracy of the results and the validity of the conclusions made in the research. It will start with a discussion of the experimental methods in Section 5.1 and finish with the assumptions made in Section 5.2.

5.1. Experimental methods

One of the main difficulties in experimental research is producing a test setup with minimal inaccuracies. Due to practical and temporal constraints not all shortcomings of the setup could be addressed, this section will discuss them and their likely influence on the result.

5.1.1. Deflector influence

To allow the speakers to influence the air in the wind tunnel openings were introduced to the tunnel wall. To prevent the flow from impinging on the downstream edge of the opening on each side deflectors were placed at the leading edges. This deflector protruded into the working section and therefore influenced the velocity. The pitot tube, which was used to set the wind tunnel velocity, was mounted upstream of the deflectors. This resulted in a mismatch between the actual freestream velocity in the measurement area and the measured freestream velocity of the pitot tube, illustrated in Figure 5.1a. The two measured values are directly related with a ratio of 1.11. The width of the test section was reduced by a factor of 1.25, which corresponds to a velocity increase with the same ratio due to the continuity constraint. Taking the diffusion of the velocity increase from the deflector to the measured area into account leads to the conclusion that the mismatch between the measured values is a direct result of the deflectors. Therefore the boundary layer was not experiencing a true zero pressure gradient, however, for the purposes of this research this was not considered a problem as this does not affect the laminar sublayer in a significant manner, which is used to determine the friction drag. An example of this is shown in Figure 5.2a, the streamwise velocity profile adheres to the theoretical $u^+ = y^+$, while in the overlap layer there is a mismatch to the log-law. This is likely attributed to the positive pressure gradient.

Figure 5.1b shows the transverse velocity in a plane parallel to the wall, at $y = 2.5$ mm. The flow in the negative z-region is exhibiting a minor positive z-directional component towards the centerline, which is likely also attributed to the deflectors. The angle of the flow to the x-axis is small, as seen from the velocity vectors. Therefore the dominant direction remains in the direction of the x-axis, which aligns with expectations. At the centerline, where the drag reduction measurements were taken, the flow is parallel to the x-axis.

5.1.2. Speaker shape and placement

The speaker drivers are selected for their frequency range and power output, see Section 3.1.3. However, these speakers are designed to have a good frequency response for the acoustic waves emitted, to produce a uniform acoustic response. In this research they are used to create an oscillating velocity field, which is not what they are intended for. Therefore the shape of the cone is most likely suboptimal,
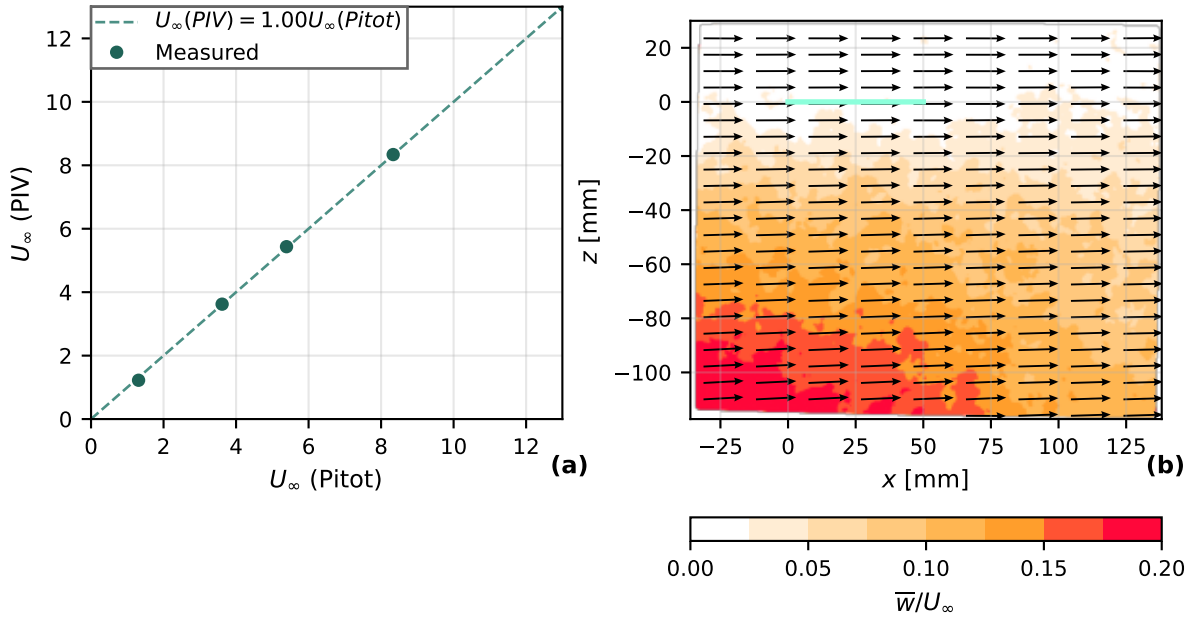
Figure 5.1: (a) U_∞ as measured with the pitot tube and averaged using the PIV data from Section 4.1. (b) transverse velocity component w overlayed with velocity vectors, parallel with the plate at $y = 2.5$ mm and with $U_\infty = 7.6$ m/s, corresponding to $Re_\tau = 1905$.

and the resonant frequency is too high. The resonant frequency could be lowered by adding mass to the diaphragm and the cone shape could be optimized to generate a constant velocity wave. This was outside the scope of the current work, and therefore the speakers were used as they are. This does produce a velocity wave that varies in the streamwise direction, therefore this is an imperfect analogy to the moving wall. The effect on the drag reduction is unknown, but based on research into other waveforms it is likely not very large [23].

The speakers are placed at a height in the y-direction such that their largest velocity output is at the plate location. This causes the lower part of the speaker to be directly opposite the test section frame. Therefore the velocity created in that region will impinge on the frame and be redirected in the positive and negative vertical direction. This vertical momentum could effect the output of the speakers, to quantify this effect measurements in a x-normal plane are required, which are out of the scope of this research.

The streamwise length of the forced area is also a factor, as discussed in Section 2.2.6. Based on the results of the characterization in Section 3.4 the velocity is reasonably constant over a streamwise length of $x/\delta \approx 1$. Based on the results of Ricco and Wu [25] this should result in approximately 50% of the drag reduction that would occur at a larger streamwise forced region. However, in contrary to the moving plate the velocity gradually decreases in the upstream direction, therefore the percentage of drag reduction is likely slightly higher.

5.2. Assumptions
Some assumptions were made during the current work to define the scope of the problem. These assumptions and their validity are discussed in this section.

5.2.1. Equilibrium boundary layer
The DUBLF features a developing turbulent boundary layer over a flat plate, which is inherently not in equilibrium. However, the facility is designed with a long test section and low freestream flow velocity, to achieve a high Re_τ with a large boundary layer thickness δ. The measurements are taken at the end of the test section, because of the large ratio between the length of the FoV and the test section length $L_{FoV}/L_{test} \approx 0.0066$ it is assumed that the boundary layer is in equilibrium along the length of the FoV.

This assumption was tested by extracting the boundary layer profile at 3 streamwise locations along the FoV. These locations are shown in Figure 5.2b and their corresponding velocity profiles are shown in Figure 5.2a. The difference between the profiles is small enough to allow for the equilibrium assumption to be valid. The maximum deviation in u_τ was found to be 0.47%.

5.2.2. Zero pressure gradient

The DUBLF is designed to produce a turbulent boundary layer with zero-pressure gradient. In this research it is therefore assumed that the pressure gradient is zero, however, there might be a slight variation. Figure 5.3 show a picture of the test section during the experiment. There are two reasons to doubt the validity of the zero pressure gradient assumption. The first are the deflectors, as explained in Section 5.1.1, marked with the green arrow. The acceleration of the flow by the deflector causes a local low pressure zone, downstream there will be a positive pressure gradient. It is assumed that the distance of the measurement area to the deflectors is sufficiently large such that the effect is negligible. A second, smaller gradient might be introduced by the test section upper wall. This wall is angled to compensate the expansion of the boundary layer, to tune this angle it is mounted on adjustable pivots that are evenly spaced. However, as the tunnel aged the transparent plastic between the pivots has started to sag, which gives it a wavy pattern, marked with the blue arrow in Figure 5.3. The effect of this is likely marginal. The resulting pressure gradient is estimated to be small. All measurements performed are compared relative to each other, so any systematic error will have cancelled out, therefore the conclusions made in this research are still considered valid.
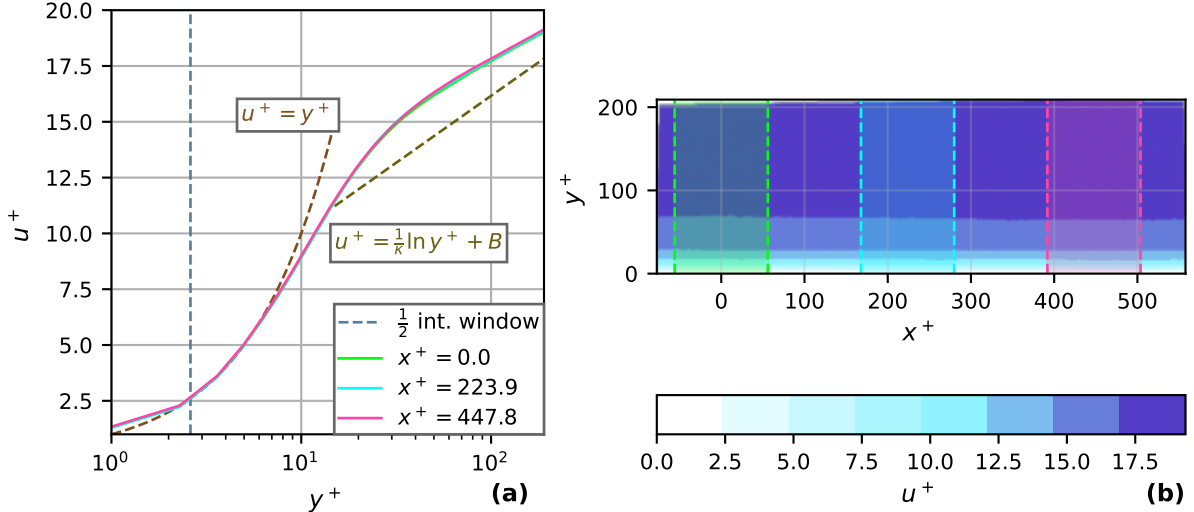
Figure 5.2: (a) Boundary layer profiles averaged at 3 different x^+ locations along the FoV (b) Averaged unforced flowfield with $Re_\tau = 1192$ and averaging regions with a width of 110 viscous units overlayed.
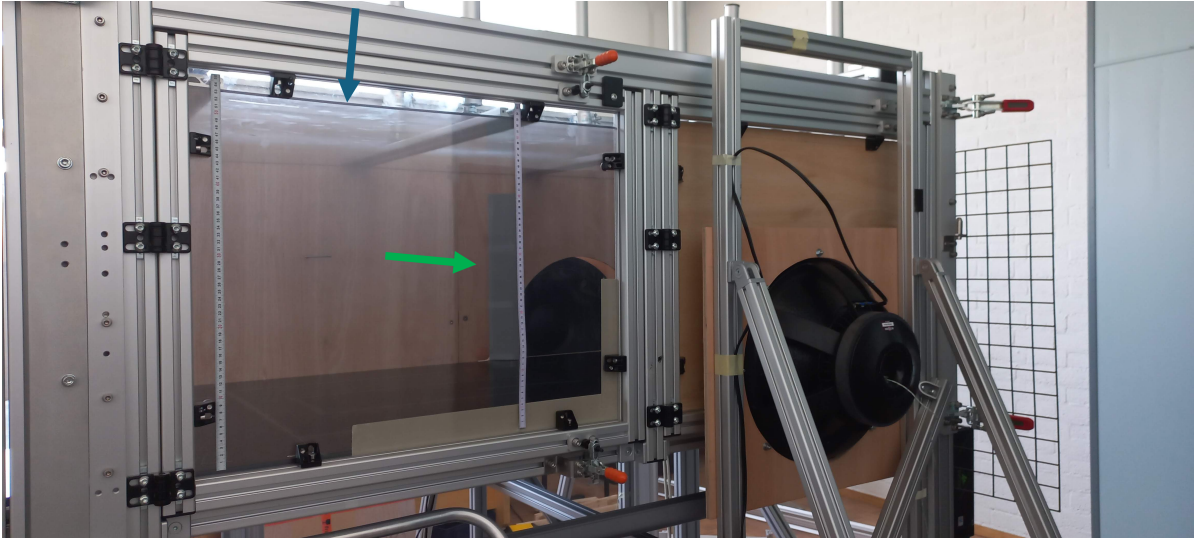
Figure 5.3: Photo of the side of the test section.

6

Conclusions

The current research set out to find the answer to the following research question: *How can the friction drag reduction in a turbulent boundary layer, from transverse forcing through oscillatory wall motion, be replicated by forcing the flow using acoustic excitation?* This chapter will describe the answer to this question and the conclusions that lead up to it.

An experimental setup was developed that can generate a transverse oscillatory flow field in a zero-pressure gradient turbulent boundary layer over a flat plate. Two speakers were placed on opposing sides and they were actuated out of phase with each other, such their momentum transfer into the fluid would complement each other. The input to the speakers was tuned such that their phase, frequency and amplitude was equal. This generated an acoustically forced flow that approximates a perfect sine wave in the midpoint between the speakers, an example of this velocity field is shown in Figure 3.16.

The velocity field in the midplane between the speakers was visualised using Stereoscopic Particle Image Velocimetry (PIV). The PIV cameras were focussed on a small area after the centerline of the speakers, to get sufficient resolution in the near-wall region. Measurements with large sample sizes were taken at several Re_τ values, for each measurement a reference case and a case with the acoustic forcing applied. Each vector field was corrected for the instantaneous location of the plate and temporally averaged. The velocity profiles were taken by spatially averaging this resulting vector field under the assumption that the boundary layer was locally in equilibrium. The transverse velocity profile compares to the profile given by Stokes' theory in part of the phase, to get an exact match for the entire actuation period more work is needed on the synchronization of the speakers.

In the laminar sublayer a linear fit was done to the streamwise velocity profile, from which the friction velocity u_τ was derived. Using this u_τ and the freestream velocity U_∞ the friction coefficient C_f was calculated. Comparing the C_f between the reference case and the forced case gave the drag reduction as a result of the acoustic transverse forcing. When the flow was forced with the correct forcing period and amplitude a drag reduction of up to $\mathcal{R} = 6.02\%$ was found. Figure 4.5 shows this result and drag reduction found for the other measurements are found in Section 4.2. In some of these other cases the forcing resulted in a drag increase, this was likely because the transverse velocity did not have the correct waveform. The drag reduction found could likely be approximately doubled by increasing the length of the forced region in the streamwise direction.

The current research did not provide enough detail to definitively identify the underlying aerodynamic mechanism behind the measured drag reduction. A large decrease in the dissipation term of the turbulence kinetic energy transport equation was found in the viscous sublayer. However, as is the case in previous works, it is unclear if this decrease in dissipation is the cause of the drag reduction or the other way around. A small shift in the profile of the $\langle u'u' \rangle$ component of the Reynolds stress was observed, again the causality between this observation and the drag reduction is undefined. A large increase in the $\langle w'w' \rangle$ was seen, this is a direct effect of the acoustic transverse forcing as the flow is oscillated in this direction. These results are discussed in Section 4.3.4.

The measured drag reduction using acoustic forcing could not directly be compared to pre-existing data from DNS studies and experiments using an oscillating wall. The forcing amplitude created by the speakers was lower than that of previous work. However, when comparing the measurements at selected T^+ and Re_τ the drag reduction does approach that found by DNS and earlier experiments. It is therefore concluded that acoustic forcing is a valid method to replicate the reduction of friction drag in a turbulent boundary layer by oscillatory wall motion.

7

Recommendations

This research was the first investigating the potential of acoustic transverse forcing, therefore there is much more knowledge to be found. As mentioned at the beginning of this document further research into friction drag reduction in a turbulent boundary layer can result in significant economic and environmental improvements. Recommendations for future researchers into this topic are explained in this chapter, based on the experience and knowledge acquired in the process of creating the current work.

7.1. Experimental setup

The experimental setup used was developed during this research and the results in this document are from the first experiments. Therefore there is much more knowledge to gain by using the current setup to its full potential. However, some improvements could be made.

The distance between the speakers is approximately 2.2 times their diameter, therefore the velocity in the centerline is significantly lower than at the speaker diaphragm. The spacing could not be reduced in the current research due to the constraints of the test section. Future work with a smaller spacing between the speaker made possible by a modified test section or using a different wind tunnel could achieve much higher amplitudes, resulting in a higher drag reduction.

The speakers in the current research were physically separated from the test section to prevent the vibrations from disturbing the measurements. Holes were cut out of the test section walls to let the momentum induced by the speaker propagate into the section. The deflectors added resulted in an acceleration of the freestream velocity, as explained in Section 5.1.1. This impacts the accuracy of the experiment. Future work should try to prevent this either by using smaller deflectors or using a different approach for coupling the speakers and the test section. The speakers could be connected to the test section by a flexible seal or even be mounted to the test section walls.

The conical shape of the speakers result in that the velocity is focussed near the speaker centerline, as shown in Figure 3.16. Therefore the streamwise area that is forced is small. Future work could focus on the shape of the actuator, for example a rectangular actuator could be used, with a long streamwise length with $x/\delta > 4$ and a height in the order of 1δ. This could focus the forcing to the near wall region, where it is most important, increasing the efficiency and enabling higher amplitudes. The longer streamwise dimension of the forced area ensures that any transient effects are minimal and the full drag reduction potential could be reached. The current setup can not achieve the maximum drag reduction because of the short streamwise forced area. Another approach to focus the velocity to the desired area could be to use a large diameter speaker and connect this to a converging section. This section focusses the induced momentum and could also be used to tune the frequency response.

7.2. Experimental procedure

This research has focussed on very low frequencies, which corresponded to the optimal forcing parameters at low Re_τ. The main reason for this was to be able to compare the results to existing data

from previous works, such as DNS results which are usually at low Re_τ. With the method proven to be functional future research could focus on higher frequencies and higher Re_τ, where speakers are designed to be operated. This could result in interesting new insights because existing methods, DNS and experimental, have difficulties operating at higher Re_τ. This research has also proven that the speakers can change the T^+ and W_m^+ independently from Re_τ. Using this across a large Re_τ range could give insights in the $Re_\tau - \mathcal{R}$ trend, which is important because practical applications have Re_τ much larger than is possible to test with current methods.

The synchronization of the speakers was done using the a microphone measuring the pressure wave emitted by the speakers, as explained in Section 3.4.2. This was done using the assumption that the phase offset between the velocity wave and pressure wave is constant. As seen in Section 4.3.2 the speakers were not fully out of phase at every measurement, impacting the effectiveness of the forcing. The limitations of this method were known early on in this research, however they could not be adjusted due to time constraints. Future work could improve the synchronization by using PIV, HWA or another method that measures the acoustic velocity directly.

7.3. Underlying mechanism

Using active methods of flow control in practical engineering applications might never be feasible. The required input power is high and the theoretical power savings low. The aim of this research is therefore to develop a tool to study the underlying aerodynamic phenomena that result in the friction drag reduction. An improved experimental setup, using the recommendations above and any other improvements, could enable future researchers to study the change in the turbulent boundary layer in detail. This method allows for high resolution PIV of the laminar sublayer as the wall is stationary, high forcing frequencies can be achieved because of the actuation mechanism and due to the freedom in settings the sensitivity of each forcing parameter can be studied independently. The insights from this could enable future researchers to develop passive methods for achieving a similar effect, reducing turbulent friction drag without active input.

References

[1] A. Colagrossi et al. "Da Vinci's observation of turbulence: A French-Italian study aiming at numerically reproducing the physics behind one of his drawings, 500 years later". In: *Physics of Fluids* 33.11 (Nov. 2021), p. 115122. ISSN: 1070-6631. DOI: 10.1063/5.0070984.

[2] Francois G. Schmitt. "Turbulence from 1870 to 1920: The birth of a noun and of a concept". In: *Comptes Rendus Mécanique* 345.9 (2017), pp. 620–626. ISSN: 1631-0721. DOI: https://doi.org/10.1016/j.crme.2017.06.003.

[3] J.E. Penner et al. "Aviation and the Global Atmosphere: A special report in collaboration with the Scientific Assessment Panel to the Montreal Protocol on Substances that Deplete the Ozone Layer". In: *Intergovernmental Panel on Climate Change* (1999).

[4] A. Abbas et al. "Drag reduction via turbulent boundary layer flow control". In: *Science China* 60 (2017), pp. 1281–1290. DOI: 0.1007/s11431-016-9013-6.

[5] M. Quadrio and P. Ricco. "Critical assessment of turbulent drag reduction through spanwise wall oscillations". In: *Journal of Fluid Mechanics* 521 (2004), pp. 251–271. DOI: 10.1017/S0022112004001855.

[6] F. Laadhari, L. Skandaji, and R. Morel. "Turbulence reduction in a boundary layer by a local spanwise oscillating surface". In: *Physics of Fluids* 6.10 (Oct. 1994), pp. 3218–3220. ISSN: 1070-6631. DOI: 10.1063/1.868052.

[7] W.C. Reynolds. "The potential and limitations of direct and large eddy simulations". In: *Whither Turbulence? Turbulence at the Crossroads*. Ed. by J.L. Lumley. Berlin, Heidelberg: Springer Berlin Heidelberg, 1990, pp. 313–343. ISBN: 978-3-540-47032-8.

[8] K.S. Choi, J.R. DeBisschop, and B.R. Clayton. "Turbulent Boundary-Layer Control by Means of Spanwise-Wall Oscillation". In: *AIAA Journal* 36.7 (1998), pp. 1157–1163. DOI: 10.2514/2.526.

[9] E.J. Hopkins, D.W. Jillie, and V.L. Sorensen. *Charts for estimating boundary-layer transition on flat plates*. Tech. rep. NASA Ames Research Center, 1970.

[10] W.S. Saric, H.L. Reed, and E.J. Kerschen. "Boundary-layer receptivity to freestream disturbances". In: *Annual Review of Fluid Mechanics* 34 (2002), pp. 291–319. DOI: 34.082701.161921.

[11] H. Schlichting and K. Gersten. *Boundary-Layer Theory (8th ed.)* Springer, 2004.

[12] H.M. Nagib and K.A. Chauhan. "Variations of von Kármán coefficient in canonical flows". In: *Physics of Fluids* 20.10 (Oct. 2008), p. 101518. ISSN: 1070-6631. DOI: 10.1063/1.3006423.

[13] M. Quadrio, P. Ricco, and C. Viotti. "Streamwise-travelling waves of spanwise wall velocity for turbulent drag reduction". In: *Journal of Fluid Mechanics* 627 (2009), pp. 161–178. DOI: 10.1017/S0022112009006077.

[14] D. Gatti et al. *Turbulent skin-friction drag reduction via spanwise forcing at high Reynolds number*. 2024. arXiv: 2409.07230 [physics.flu-dyn].

[15] N. Kasagi, Y. Hasegawa, and K. Fukagata. "Toward cost-effective Control of Wall Turbulence for Skin Friction Drag Reduction". In: *Advances in Turbulence XII*. Ed. by Bruno Eckhardt. Berlin, Heidelberg: Springer Berlin Heidelberg, 2009, pp. 189–200. ISBN: 978-3-642-03085-7.

[16] D. Gatti and M. Quadrio. "Reynolds-number dependence of turbulent skin-friction drag reduction induced by spanwise forcing". In: *Journal of Fluid Mechanics* 802 (2016), pp. 553–582. DOI: 10.1017/jfm.2016.485.

[17] M. Skote. "Turbulent boundary layer flow subject to streamwise oscillation of spanwise wall-velocity". In: *Physics of Fluids* 23.8 (Aug. 2011), p. 081703. ISSN: 1070-6631. DOI: 10.1063/1.3626028.

[18] A. Yakeno, Y. Hasegawa, and N. Kasagi. "Spatio-temporally periodic control for turbulent friction drag reduction." In: (Jan. 2009).

[19] C. Viotti, M. Quadrio, and P. Luchini. "Streamwise oscillation of spanwise velocity at the wall of a channel for turbulent drag reduction". In: *Physics of Fluids* 21.11 (Nov. 2009), p. 115109. ISSN: 1070-6631. DOI: 10.1063/1.3266945.

[20] M. Mishra and M. Skote. "Drag Reduction in Turbulent Boundary Layers with Half Wave Wall Oscillations". In: *Mathematical Problems in Engineering* 2015.1 (2015), p. 253249. DOI: 10.1155/2015/253249.

[21] M.W. Knoop et al. "Experimental assessment of square-wave spatial spanwise forcing of a turbulent boundary layer". English. In: *Experiments in Fluids* 65.5 (2024). ISSN: 0723-4864. DOI: 10.1007/s00348-024-03799-9.

[22] W.J. Jung, N. Mangiavacchi, and R. Akhavan. "Suppression of turbulence in wall-bounded flows by high-frequency spanwise oscillations". In: *Physics of Fluids A: Fluid Dynamics* 4.8 (Aug. 1992), pp. 1605–1607. ISSN: 0899-8213. DOI: 10.1063/1.858381.

[23] P. Ricco, M. Skote, and M.A. Leschziner. "A review of turbulent skin-friction drag reduction by near-wall transverse forcing". In: *Progress in Aerospace Sciences* 123 (May 2021), p. 100713. ISSN: 0376-0421. DOI: 10.1016/j.paerosci.2021.100713.

[24] M. Skote, M. Mishra, and Y. Wu. "Wall Oscillation Induced Drag Reduction Zone in a Turbulent Boundary Layer". In: *Flow Turbulence Combust* 102 (2019), pp. 641–666. DOI: 10.1007/s10494-018-9979-2.

[25] P. Ricco and S. Wu. "On the effects of lateral wall oscillations on a turbulent boundary layer". In: *Experimental Thermal and Fluid Science* 29.1 (2004), pp. 41–52. ISSN: 0894-1777. DOI: https://doi.org/10.1016/j.expthermflusci.2004.01.010.

[26] K.U. Kempaiah et al. "3-dimensional particle image velocimetry based evaluation of turbulent skin-friction reduction by spanwise wall oscillation". In: *Physics of Fluids* 32.8 (Aug. 2020), p. 085111. ISSN: 1070-6631. DOI: 10.1063/5.0015359.

[27] K. Gouder, M. Potter, and J.F. Morrison. "Turbulent friction drag reduction using electroactive polymer and electromagnetically driven surfaces". In: *Experiments in Fluids* 54.1441 (2013). DOI: 10.1007/s00348-012-1441-y.

[28] M. Skote. "Comparison between spatial and temporal wall oscillations in turbulent boundary layer flows". In: *Journal of Fluid Mechanics* 730 (Sept. 2013). DOI: 10.1017/jfm.2013.344.

[29] R. Moarref and M.R. Jovanović. "Model-based design of transverse wall oscillations for turbulent drag reduction". In: *Journal of Fluid Mechanics* 707 (2012), pp. 205–240. DOI: 10.1017/jfm.2012.272.

[30] L. Ding et al. *Acceleration is the Key to Drag Reduction in Turbulent Flow*. 2024. arXiv: 2312.12591 [physics.flu-dyn].

[31] E. Touber and M.A. Leschziner. "Near-wall streak modification by spanwise oscillatory wall motion and drag-reduction mechanisms". In: *Journal of Fluid Mechanics* 693 (2012), pp. 150–200. DOI: 10.1017/jfm.2011.507.

[32] L. Agostini and M.A. Leschziner. "On the departure of near-wall turbulence from the quasi-steady state". In: *Journal of Fluid Mechanics* 871 (July 2019). DOI: 10.1017/jfm.2019.395.

[33] J. Yao, X. Chen, and F. Hussain. "Reynolds number effect on drag control via spanwise wall oscillation in turbulent channel flows". In: *Physics of Fluids* 31.8 (Aug. 2019), p. 085108. ISSN: 1070-6631. DOI: 10.1063/1.5111651.

[34] I. Marusic et al. "An energy-efficient pathway to turbulent drag reduction". In: *Nature Communications* 12.5805 (2021). DOI: 10.1038/s41467-021-26128-8.

[35] D. Gatti and M. Quadrio. "Performance losses of drag-reducing spanwise forcing at moderate values of the Reynolds number". In: *Physics of Fluids* 25.12 (Dec. 2013), p. 125109. ISSN: 1070-6631. DOI: 10.1063/1.4849537.

[36] E. Hurst, Q. Yang, and Y.M. Chung. "The effect of Reynolds number on turbulent drag reduction by streamwise travelling waves". In: *Journal of Fluid Mechanics* 759 (2014), pp. 28–55. DOI: 10.1017/jfm.2014.524.

[37] P. Ricco et al. "Changes in turbulent dissipation in a channel flow with oscillating walls". In: *Journal of Fluid Mechanics* 700 (2012), pp. 77–104. DOI: 10.1017/jfm.2012.97.

[38] W. Yuan et al. "Phase-space dynamics of near-wall streaks in wall-bounded turbulence with spanwise oscillation". In: *Physics of Fluids* 31.12 (Dec. 2019), p. 125113. ISSN: 1070-6631. DOI: 10.1063/1.5130161.

[39] L. Agostini, E. Touber, and M.A. Leschziner. "The turbulence vorticity as a window to the physics of friction-drag reduction by oscillatory wall motion". In: *International Journal of Heat and Fluid Flow* 51 (2015), pp. 3–15. ISSN: 0142-727X.

[40] K.S. Choi. "Near-wall structure of turbulent boundary layer with spanwise-wall oscillation". In: *Physics of Fluids* 14.7 (July 2002), pp. 2530–2542. ISSN: 1070-6631. DOI: 10.1063/1.1477922.

[41] M. Quadrio and P. Ricco. "The laminar generalized Stokes layer and turbulent drag reduction". In: *Journal of Fluid Mechanics* 667 (2011), pp. 135–157. DOI: 10.1017/S0022112010004398.

[42] M. V. Goudar, W.-P. Breugem, and G. E. Elsinga. "Auto-generation in wall turbulence by the interaction of weak eddies". In: *Physics of Fluids* 28 (2016). DOI: 10.1063/1.4944048.

[43] O. Sendstad and P. Moin. "On the mechanics of 3-D turbulent boundary layers". In: *Symposium on Turbulent Shear Flows, 8 th, Munich, Federal Republic of Germany*. 1991, pp. 5–4.

[44] A. Baron and M. Quadrio. "Turbulent drag reduction by spanwise wall oscillations". In: *Applied Scientific Research* 55 (1995), pp. 311–326. DOI: 10.1007/BF00856638.

[45] G.G. Stokes. *On the effect of the internal friction of fluids on the motion of pendulums*. Creative Media Partners, LLC, 1851. ISBN: 9781015199002.

[46] R. Akhavan, W. Jung, and N. Mangiavacchi. "Control of wall turbulence by high frequency spanwise oscillations". In: *3rd Shear Flow Conference*. DOI: 10.2514/6.1993-3282.

[47] J. Jimenez and A. Pinelli. "Wall turbulence - How it works and how to damp it". In: *4th Shear Flow Control Conference*. 1997. DOI: 10.2514/6.1997-2112.

[48] M.W. Knoop et al. "Response of a turbulent boundary layer to steady, square-wave-type transverse wall-forcing". In: *Phys. Rev. Fluids* 10 (6 June 2025), p. 064607. DOI: 10.1103/PhysRevFluids.10.064607.

[49] F. Hoffman. *Encyclopedia of Recorded Sound*. Routledge, 2004. DOI: 10.4324/9780203484272.

[50] A. Fischer, E. Sauvage, and I. Roehle. "Acoustic PIV: Measurement of the acoustic particle velocity using synchronized PIV□technique". In: *The Journal of the Acoustical Society of America* 123.5 (May 2008), pp. 3130–3130. ISSN: 0001-4966. DOI: 10.1121/1.2933079.

[51] G. Huelsz and F. Lópz-Alquicira. "Hot-wire anemometry in acoustic waves". In: *Experiments in Fluids* 30 (2001), pp. 283–285. DOI: 10.1007/s003480000174.

[52] P. Buchhave and C.M. Velte. "Reduction of noise and bias in randomly sampled power spectra". In: *Experiments in Fluids* 56.4 (2015). ISSN: 1432-1114. DOI: 10.1007/s00348-015-1922-x.

[53] O. Léon et al. "Measurement of acoustic velocity components in a turbulent flow using LDV and high-repetition rate PIV". In: *Experiments in Fluids* 58.6 (2017), p. 72. DOI: 10.1007/s00348-017-2348-4.

[54] G. Huelsz and F. López-Alquicira. "Velocity measurements in the oscillatory boundary layer produced by acoustic waves". In: *Experiments in Fluids* 32 (2002), pp. 612–614. DOI: 10.1007/s00348-001-0383-6.

[55] S. Glegg, M. Szőke, and W. Devenport. "Acoustic transmission loss and noise from Kevlar wind tunnel walls". In: *International Journal of Aeroacoustics* 21.5-7 (2022), pp. 382–409. DOI: 10.1177/1475472X221107497.

[56] M.W. Knoop, A.H. Hassanein, and W.J. Baars. "Delft University Boundary Layer Facility". In: 2025.

[57] A. Sciacchitano and B. Wieneke. "PIV uncertainty propagation". In: *Measurement Science and Technology* 27 (2016). DOI: 10.1088/0957-0233/27/8/084006.
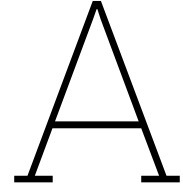
Test Matrix

Table A.1 contains the input settings used during the wind tunnel experiment. The parameters f, P_A, P_B and φ_B are used as inputs to the speaker system. U_∞ controls the wind tunnel speed. The PIV column describes the PIV plane setup used, with p120p a z-normal plane with dimensions 153.5×127.5 mm, p5020 a stereo z-normal plane with dimensions 56.3×21.0 mm and wp260 a wall-parallel plane with dimensions 183.1×153.2 mm, see Section 3.3.1 for more detail. f_{PIV}, N_{im} and Δt are the input parameters for the PIV system. Re_τ, W_m^+ and T^+ are calculated using the characterization data described in Section 3.4 and an estimated u_τ obtained from wind tunnel characterization data [56].

The abbreviations used in the Name column are explained in Table A.2.

Commissioning

Name	#	Spk	f [Hz]	A_{in_A}	A_{in_B}	U_∞	φ_B	PIV	f_{PIV}	N_{im}	Re_τ	W_m^+	T^+	u_τ	Δt [us]
IT	1	A	50.0	0.30	0.30	5.00	0.000								59
TL	2	A	146.0	0.30	0.30	0.00	0.000								
BL	3	-				1.14		p120p	15.00	1000	500				257
	4	-				3.27		p120p	15.00	1000	1000				90
	5	-				7.53		p120p	15.00	1000	2000				39
	6	-				11.78		p120p	15.00	1000	3000				25
SPIV	7	-	0.0	0.00	0.00	5.00		p5020		200					59

Experiments

Name	#	Spk	f [Hz]	A_{in_A}	A_{in_B}	U_∞	φ_B	PIV	f_{PIV}	N_{im}	Re_τ	W_m^+	T^+	u_τ	Δt [us]
SS	8	AB	20.0	0.25	0.25	0.00									
	9	AB	30.0	0.35	0.35	0.00									
	10	AB	50.0	0.50	0.50	0.00									
	11	AB	65.0	0.50	0.50	0.00									
	12	AB	100.0	0.35	0.35	0.00									
	13	AB	146.0	0.30	0.30	0.00									
Tp83	14	-				3.83		p5020	15.00	1500	1131			0.16	77
	15	AB	20.0	0.25	0.23	3.83	0.039	p5020	14.89	3000	1131	0.80	83	0.16	77
	16	-				4.87		p5020	15.00	1500	1377			0.19	60
	17	AB	30.0	0.35	0.33	4.87	-0.033	p5020	14.94	3000	1377	1.54	83	0.19	60
	18	-				6.53		p5020	15.00	1500	1767			0.25	45
	19	AB	50.0	0.50	0.43	6.53	0.035	p5020	14.73	3000	1767	1.06	83	0.25	45
	20	-				7.57		p5020	15.00	1500	2010			0.28	39
	21	AB	65.0	0.50	0.47	7.57	0.002	p5020	14.83	3000	2010	0.91	83	0.28	39
	22	-				9.59		p5020	15.00	1500	2485			0.35	31
	23	AB	100.0	0.35	0.32	9.59	0.000	p5020	14.73	3000	2485	0.42	83	0.35	31
	24	-				11.77		p5020	15.00	1500	2996			0.42	25
	25	AB	146.0	0.30	0.32	11.77	0.008	p5020	14.75	3000	2996	0.30	83	0.42	25

Name	#	Spk	f [Hz]	A_{in_A}	A_{in_B}	U_∞	φ_B	PIV	f_{PIV}	N_{im}	Re_τ	W_m^+	T^+	u_τ	Δt [us]
Map	26	-				1.14		p5020	15.00	1000	500			0.07	257
	27	AB	30.0	0.35	0.33	1.14	-0.033	p5020	14.94	1000	500	4.43	10	0.07	257
	28	AB	65.0	0.50	0.47	1.14	0.002	p5020	14.83	1000	500	3.87	5	0.07	257
	29	AB	146.0	0.30	0.32	1.14	0.008	p5020	14.75	1000	500	1.89	2	0.07	257
	30	-				3.27		p5020	15.00	1000	1000			0.14	90
	31	AB	30.0	0.35	0.33	3.27	-0.033	p5020	14.94	1000	1000	1.31	43	0.14	90
	32	AB	65.0	0.50	0.47	3.27	0.002	p5020	14.83	1000	1000	1.52	20	0.14	90
	33	AB	146.0	0.30	0.32	3.27	0.008	p5020	14.75	1000	1000	1.83	9	0.14	90
	34	-				7.53		p5020	15.00	1000	2000			0.28	39
	35	AB	30.0	0.35	0.33	7.53	-0.033	p5020	14.94	1000	2000	0.52	178	0.28	39
	36	AB	65.0	0.50	0.47	7.53	0.002	p5020	14.83	1000	2000	1.50	82	0.28	39
	37	AB	146.0	0.30	0.32	7.53	0.008	p5020	14.75	1000	2000	0.55	37	0.28	39
	38	-				11.78		p5020	15.00	1000	3000			0.42	25
	39	AB	30.0	0.35	0.33	11.78	-0.033	p5020	14.94	1000	3000	0.70	405	0.42	25
	40	AB	65.0	0.50	0.47	11.78	0.002	p5020	14.83	1000	3000	0.61	187	0.42	25
	41	AB	146.0	0.30	0.32	11.78	0.008	p5020	14.75	1000	3000	0.30	83	0.42	25
SS	42	AB	29.7	0.35		0.00									
	43	AB	53.4	0.50		0.00									
	44	AB	84.0	0.40		0.00									
	45	AB	121.5	0.35		0.00									
Tp100	46	-				5.40		p5020	15.00	1500	1500			0.21	54
	47	AB	29.7	0.35	0.32	5.40	0.013	p5020	14.79	3000	1500		100	0.21	54
	48	-				7.53		p5020	15.00	1500	2000			0.28	39
	49	AB	53.4	0.50	0.50	7.53	0.020	p5020	14.81	3000	2000		100	0.28	39
	50	-				9.65		p5020	15.00	1500	2500			0.35	30
	51	AB	84.0	0.40	0.41	9.65	0.012	p5020	14.85	3000	2500		100	0.35	30
	52	-				11.78		p5020	15.00	1500	3000			0.42	25
	53	AB	121.5	0.35	0.42	11.78	0.000	p5020	14.82	3000	3000		100	0.42	25
SS	54	AB	20.0	0.27		0.00									
	55	AB	30.0	0.20		0.00									
	56	AB	50.0	0.41		0.00									
	57	AB	65.0	0.48		0.00									
REYN	58	-				4.28		p5020	15.00	1500	1237			0.17	68
	59	AB	20.0	0.27	0.26	4.28	0.050	p5020	14.88	3000	1237	0.80	100	0.17	68
	60	-				5.43		p5020	15.00	1500	1508			0.21	54
	61	AB	30.0	0.20	0.18	5.43	-0.056	p5020	14.95	3000	1508	0.80	100	0.21	54
	62	-				7.26		p5020	15.00	1500	1937			0.27	40
	63	AB	50.0	0.41	0.36	7.26	0.020	p5020	14.74	3000	1937	0.80	100	0.27	40
	64	-				8.39		p5020	15.00	1500	2203			0.31	35
	65	AB	65.0	0.48	0.47	8.39	-0.003	p5020	14.83	3000	2203	0.80	100	0.31	35
LFoV	66	-				4.87		p120s	15.00	1000	1377			0.19	120
	67	AB	30.0	0.35	0.33	4.87	-0.033	p120s	14.94	2200	1377	1.54	83	0.19	120
	68	-				7.57		p120s	15.00	1000	2010			0.28	77
	69	AB	65.0	0.50	0.47	7.57	0.002	p120s	14.83	2200	2010	0.91	83	0.28	77
WP	70	-				4.87		wp260	15.00	1000	1377			0.19	240
	71	AB	30.0	0.35	0.33	4.87	-0.033	wp260	14.94	2200	1377	1.54	83	0.19	240
	72	-				7.57		wp260	15.00	1000	2010			0.28	155
	73	AB	65.0	0.50	0.47	7.57	0.002	wp260	14.83	2200	2010	0.91	83	0.28	155
04REP	74	-				3.27		p120p	15.00	1000	1000			0.14	90
BL	75	-				4.87		p120p	15.00	1000	1377			0.19	60

Table A.1: Wind tunnel experiment test matrix

Name	Description
IT	Initial test
TL	Find thermal limits
BL	Boundary layer characterization
SPIV	Stereo PIV development
SS	Speaker synchronization using microphone
Tp83	Constant period run with $T^+ = 83$
Map	Map various values at maximum amplitude
Tp100	Constant period run with $T^+ = 100$
REYN	Contant T^+ and W_m^+ run
LFoV	Repeat tests with larger FoV
WP	Wall parallel measurements
04REP	Repeat of measurement 4 due to Δt error

Table A.2: Abbreviations from test matrix

B

Processing Workflow

This appendix contains extra information about the wind tunnel experiment data processing workflow. Section B.1 describes the data acquisition processing methods and Section B.2 the PIV methods.

B.1. Data acquisition

The electrical signals to the speakers and PIV equipment were recorded using a NI CompactDAQ data recorder with the channels described in Table B.1. The signals have been sampled at 51200 Hz and saved to a .txt file. The DAQ data is compressed and the phase of the speaker input signals is found as described in the following sections.

B.1.1. Compression

The DAQ files are approximately 400 MB per measurement of 1500 PIV images and take a while to read during the data processing stage. They are therefore compressed using the method described in this section.

The full data set is read into memory using a Python script and all Programmable Timing Unit (PTU) pulses are found using the `scipy.signal.find_peaks` function, which correspond to the time when the images were taken. Then the other channels were sampled at these locations and this data set, together with the phase of V_A and V_B as described in Section B.1.2, was saved to a .csv file. The compressed files are approximately 126 kB and load much faster into the processing scripts.

An extra pulse was found in each measurement, i.e. for a set of 1500 images there were 1501 PTU pulses. The temporal spacing of each pulse was equal. To solve the issue a single dataset was processed twice omitting either the first or last pulse. When the first pulse was omitted a clear correlation between average w velocity and the V_A was found, leading to the conclusion that the first PTU pulse did not have a corresponding PIV image set.

Name	Variable	Unit	Description
X_Value	t	s	Time since start of recording
TempA	T_A	$^\circ C$	Temperature of speaker A
TempB	T_B	$^\circ C$	Temperature of speaker B
Mic	p_{mic}	mV	Output of microphone
PTU	V_{PTU}	V	Q-Switch input for laser pulse
V_A	V_A	V	Electrical signal to speaker A
V_B	V_B	V	Electrical signal to speaker B

Table B.1: NIDAQ channels

B.1.2. Phase estimation

As the compressed files only save the values at the PTU pulses the time-resolved evolution of the signals is lost. For most of the channels this is not an issue but the phase in the sine waves of V_A and V_B must be known for grouping the PIV vector fields according to phase.

The sine wave of Equation B.1 was fitted to the time series around each PTU pulse. The width of this fit was chosen to be 16 cycles to get a good accuracy and an initial guess based on the expected amplitude and frequency was used. The value φ was used as the phase of the signal at the pulse.

$$V_i = A_i \sin(\omega t + \varphi) \tag{B.1}$$

B.2. Velocity field processing

B.2.1. Plate location estimation

The speakers and their mounting were physically separated from the wind tunnel test section to minimize the vibrations from the speakers influencing the measurements. However, the acoustic pressure from the speakers did induce a non-negligible vibration in the anodized aluminium plate. The vibration was small enough to consider its aerodynamic effect negligible, but the movement must be taken into account when averaging the PIV vector fields.

The location of the plate can be calculated using the velocity profile. This profile is taken from each column in x, as the angle of the plate to the image axes is small this vertical approximation can be used. For each of these profiles a straight line is fitted to the linear region between $0 \leq y^+ \leq 5$ of the velocity profile, as shown in Figure B.1b. Another line is fitted to the reflected image of the velocity below the plate. The estimated location of the plate y_p is determined by the crossing of these lines. The calculated y_p for each x on an example vector field is shown in Figure B.1a. To these locations a straight line is fitted, which determines the assumed height and angle of the plate at this particular instance in time. This calculation is performed on each vector field of a measurement.

A straight fit line to the calculated y_p is only suitable if the plate is flat. To test this assumption the deviation of y_p to the fit y_{fit} is plotted in Figure B.2a for the full measurement, number 15 of Table A.1, with 1500 vector fields. The average deviation for each x is also shown, this reasonably approximates a straight line and thus the assumption is valid. The probability density of the deviation of y_p to y_{fit} is shown in Figure B.2b and follows a normal distribution. The mean standard deviation for the full measurement $|\sigma^2| = 0.0157$ mm.

The deviation of y_p compared to its mean location and the deviation of the angle θ are shown in Figure B.3a, sorted based on the phase φ of the speaker signal V_A. This data is from measurement 15 of Table A.1. There is a strong correlation between the displacement of the plate and the speaker signal, confirming that the movement is caused by the speaker output. Analysis of the Power Spectral Density of the plate position from Figure B.3b shows a resonance at $3.1f$, corresponding to $f_{plate} \approx 64$ Hz. Analysis of other measurements confirms this resonant frequency of the plate.

B.2.2. Averaging

As the turbulent boundary layer is defined relative to the flat plate, each image must be corrected to the plate location before averaging. For each column of vectors in x the plate location $y_p(x)$ is calculated, then the column is shifted upwards by subtracting $y_p(x)$ as depicted in Figure B.4, resulting in the plate being located at $y = 0$. A common grid is defined, with x exactly the same as the original images and y based on the average plate location with the same spacing as the original axis. The shifted column is then interpolated onto the common grid. Finally each column is averaged with all the other images of the measurement set. This method does not take the rotation of the plate into account. However, as the plate angle is between $-0.26° < \theta < 0.05°$ the effect of skewing instead of rotation is considered negligible.

The phase averaged data is extracted by dividing $0 \leq \varphi < 2\pi$ into 20 bins of $\varphi_{bin} = 0.1\pi$. This number was chosen to give good phase resolution while keeping the averages converged, see Section B.2.5 for more details.
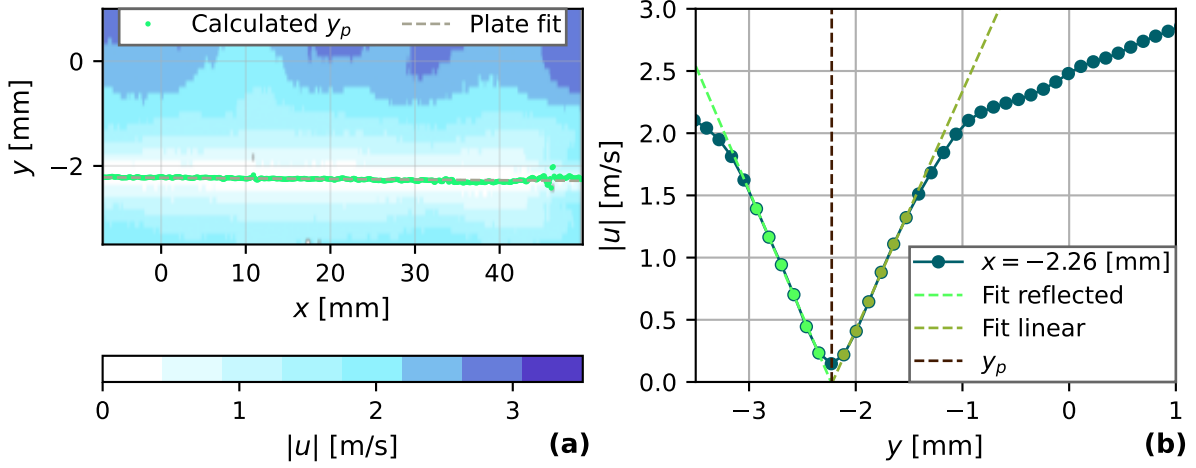
Figure B.1: (a) Part of vector field from a random image set with the calculated plate location and fit overlayed. (b) Visualisation of process calculating plate location at a x-location.
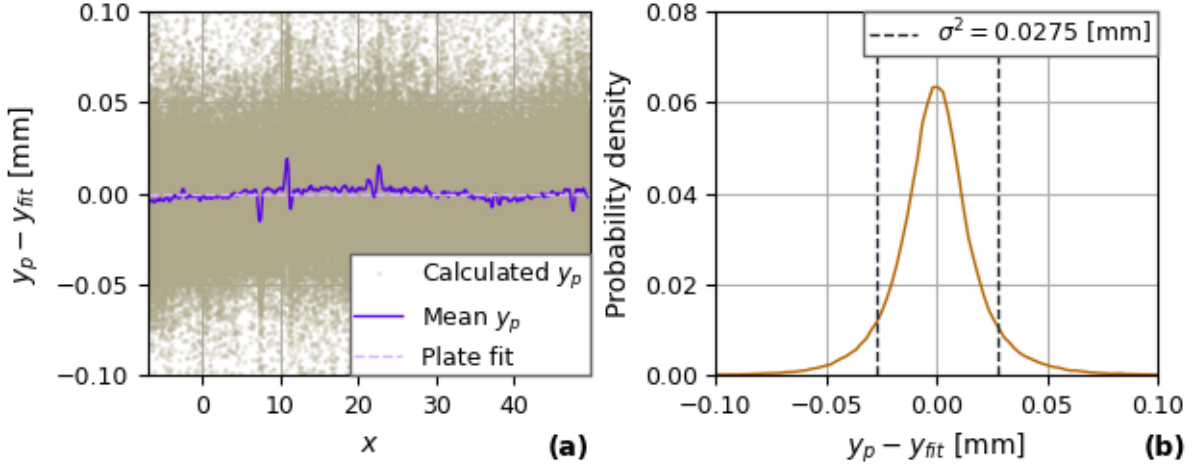

Figure B.2: (a) Deviation of calculated plate location from linear plate fit for full measurement. (b) Probability density function for deviation of plate location to linear plate fit.

B.2.3. Extracting friction velocity

To calculate the skin friction the friction velocity u_τ is needed. This is calculated using

$$u_\tau = \sqrt{\nu \left(\frac{\partial u}{\partial y}\right)_{y=0}} \tag{B.2}$$

where the kinematic viscosity ν is calculated from the atmospheric conditions. The wall-normal gradient of velocity $\frac{\partial u}{\partial y}$ at the wall is calculated by fitting a straight line to the streamwise velocity in the laminar sublayer, with $0 \leq y^+ < 5$. This range is further constrained by setting the height of a half interrogation window as the lower bound, because the vectors closer to the plate are distorted by the plate itself. To calculate the upper bound u_τ is needed, making this an iterative calculation. A first estimate of u_τ is made using earlier characterization data from the DUBLF, see Section 3.2.1. An estimate of $\frac{\partial u}{\partial y}$ is then extracted from the resulting range, which is then used to calculate a closer estimate of u_τ and thus $y^+ = 5$. This process is repeated until u_τ converges. It was found that at most 2 iterations were needed in all cases. See Figure B.5 for a graphic representation of this process.

B.2.4. Turbulence statistics

To get better insights into the behaviour of the turbulent boundary layer the turbulence statistics were extracted. The Reynolds stress components $\langle u_i' u_j' \rangle$ are calculated using the velocity fluctuations, defined
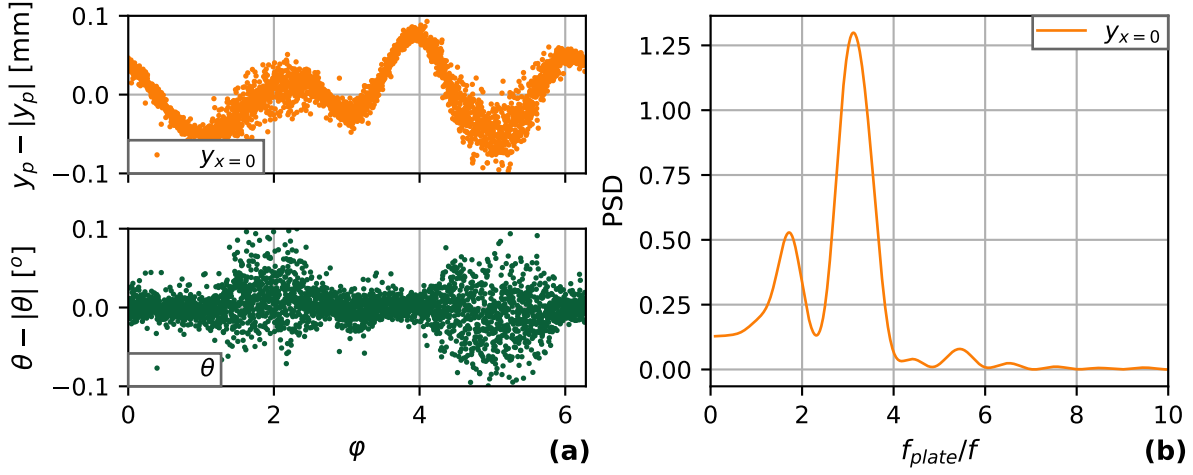
Figure B.3: (a) Plate location and angle deviation from the mean over phase of V_A. (b) Power spectral density of plate location, normalized with speaker frequency.

by $u_i' = u_i - \overline{u}_i$, with u_i the instantaneous velocity component and $\overline{u}_i$ the average velocity component. The average velocity component was calculated using the complete measurement, after which the fluctuations were calculated for each PIV vector field. After multiplication to get the instantaneous Reynolds stresses they were averaged for the complete measurement.

The turbulence kinetic energy equation is given by

$$\frac{\partial k}{\partial t} + \mathcal{M} = \mathcal{C} + \mathcal{D} + \mathcal{P} + \Pi - \varepsilon \tag{B.3}$$

With the following components:

With k as the turbulence kinetic energy, x_i the direction corresponding to u_i, ρ the density, ν the kinematic viscosity and p' the pressure fluctuations. The pressure could not be directly measured and was estimated using the dynamic pressure and assuming a zero pressure gradient. This gave unusual results for the pressure transport term and thus it was chosen to omit this term. For each measurement the rest of the components are calculated, after which they are averaged for the complete set. As the production and dissipation terms are the largest the main focus is on them.

B.2.5. PIV convergence

The variables of interest are taken from the averaged velocity field, which is calculated from PIV images. The random nature of turbulent flow forces the number of images required for a representative average to be high. To find the minimum number of images required and to validate the results a convergence study was performed.

Figure B.6a shows the convergence of u_τ averaged over different number of images N_{im}. This convergence was calculated by averaging subsets of images taken from a reference measurement with $Re_\tau = 1151$ and no forcing applied. The value of u_τ converges to within 0.3% of the full set within 600

$$
\begin{aligned}
\mathcal{M} &= \langle u_j \rangle \frac{\partial k}{\partial x_j} && \text{(Mean flow convection)} \\
\mathcal{C} &= -\frac{1}{2}\frac{\partial \langle u_i' u_i' u_j' \rangle}{\partial x_j} && \text{(Turbulent convection)} \\
\mathcal{D} &= \nu \frac{\partial^2 k}{\partial x_j^2} && \text{(Turbulent diffusion)} \\
\mathcal{P} &= -\langle u_i' u_j' \rangle \frac{\partial \langle u_i \rangle}{\partial x_j} && \text{(Production)} \\
\Pi &= -\frac{1}{\rho}\frac{\partial \langle u_j' p' \rangle}{\partial x_j} && \text{(Pressure transport)} \\
\varepsilon &= \nu \left\langle \frac{\partial u_i'}{\partial x_j}\frac{\partial u_i'}{\partial x_j} \right\rangle && \text{(Dissipation)}
\end{aligned}
$$
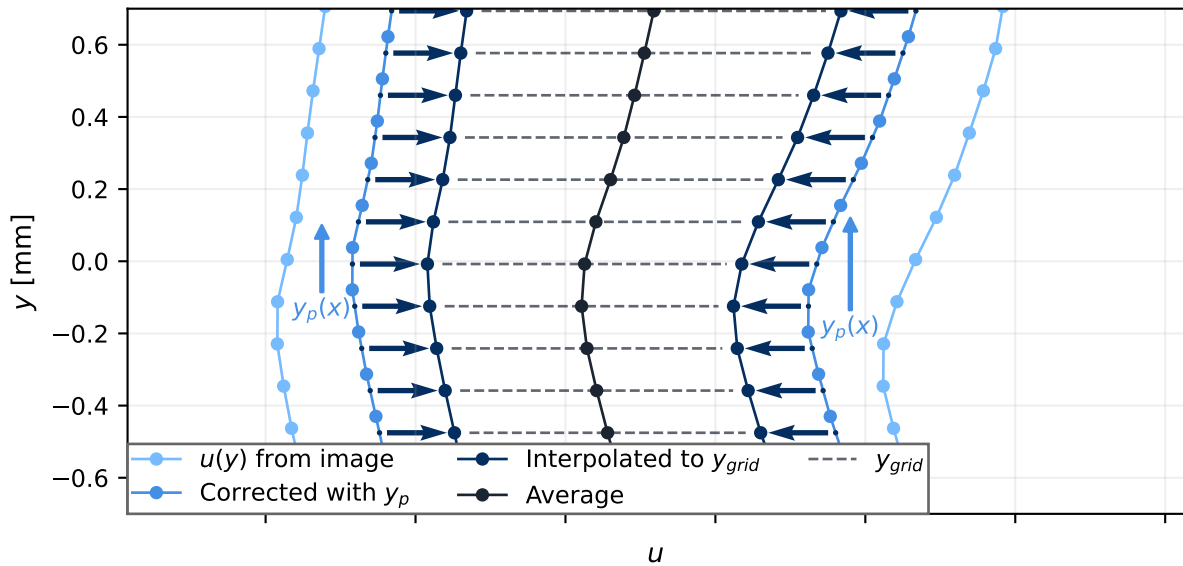
Figure B.4: Schematic depiction of the averaging process of a column of vectors at a single x location. The 2 outer curves represent the same column in different images.

images. It is therefore considered that the average of 1500 images for the unforced cases and 3000 images for the forced cases is considered accurate.

The number of images in the forced cases is set at 3000 images to allow the set to be divided according to phase. Averaging over the phase enables the forcing parameters to be extracted and the effects of the forcing to be studied in more detail. Figure B.6b shows the convergence of the transverse velocity w for a subset of images corresponding to peak velocity within the phase. It shows that w converges to within 1% of the final average within 150 images. This enables a set of 3000 images to be divided into 20 phase bins, giving sufficient detail in the phase averaged profiles.
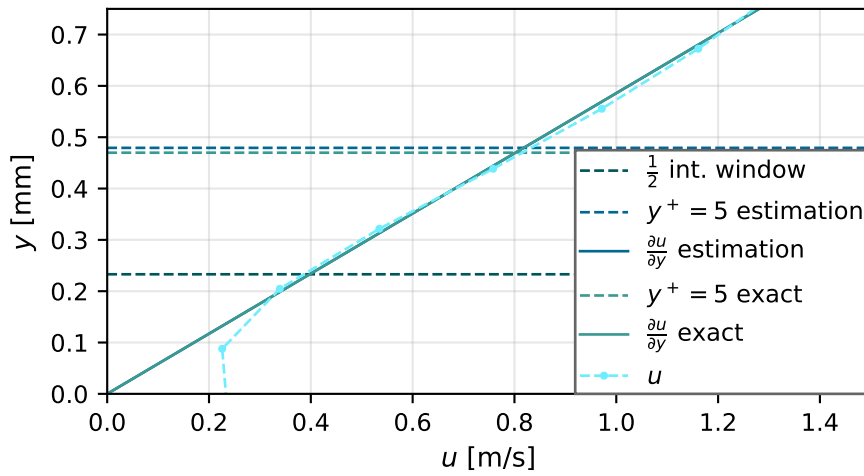
Figure B.5: Example of the processing routine for extracting u_τ. The range in which to apply a linear fit is constrained by half the interrogation window size and $y^+ \leq 5$, which is first estimated based on characterization data and then calculated exactly.
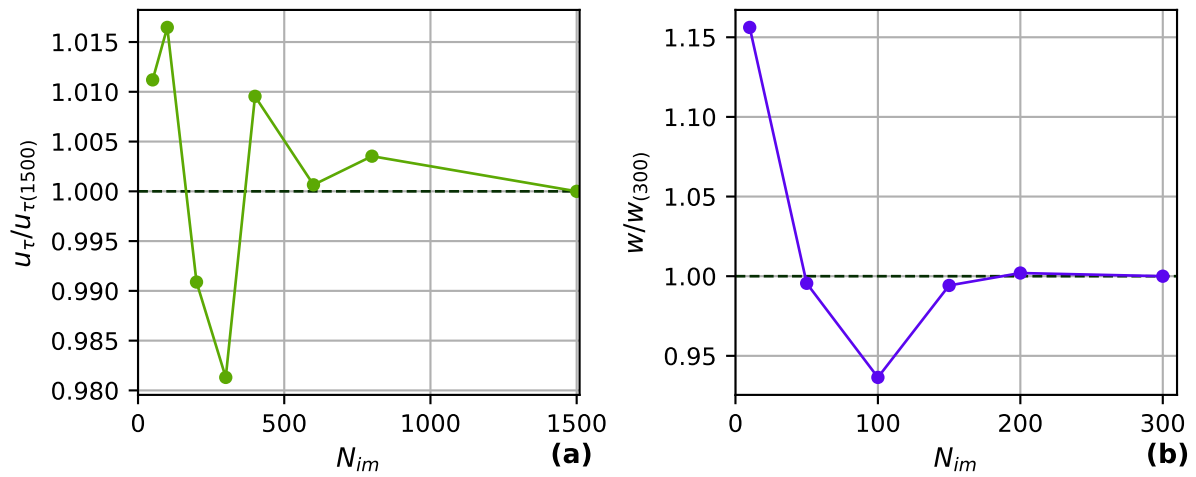
Figure B.6: (a) Convergence of u_τ for measurement 14 from Table A.1 (b) Convergence of the average w in $y > 3$ mm using measurements taken between $0.35\pi \leq \varphi \leq 0.55\pi$, which corresponds to peak velocity in measurement 15 from Table A.1.

C
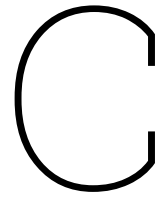
PIV Results

C.1. Speaker velocity field

The main results and conclusions from the speaker characterization test can be found in Section 3.4. This section shows all the measured velocity fields in Section C.1.1.

C.1.1. Phase averaged velocity fields

This section shows the phase averaged velocity fields for all the test frequencies used in the characterization of the speakers. The phase values used are with reference to the electrical signal to speaker A, V_A, therefore $\varphi = 0$ is at the first zero crossing of V_A. The amplitude W_m values used for normalising the velocity fields are found in Figure 3.18a.

Figure C.1 shows the velocity field for $f = 20$ Hz. This is the only frequency tested below the resonant frequency $f_s = 30$ Hz of the speakers. The velocity is low as the speakers are not designed to operate at this frequency. The shape of the velocity field is symmetric around the speaker centerline, indicating that the synchronization is adequate. The velocity field with $f = f_s$ is shown in Figure 3.16 and discussed in Section 3.4.3, at this frequency the maximum amplitude was achieved. At $f = 50$ Hz and $f = 65$ Hz a similar high amplitude was achieved. The velocity fields are similar and shown in Figures C.2 and C.3, they are symmetric around the speaker centerline. At $f = 100$ Hz, shown in Figure C.4, the amplitude drops, resulting in a smoother velocity field. This indicates that there are fewer fluctuations present. The velocity field at $f = 146$ Hz is similar and shown in Figure C.5.

Figure C.1: Phase averaged velocity field for characterization test with $f = 20$ Hz.

Figure C.2: Phase averaged velocity field for characterization test with $f = 50$ Hz.

Figure C.3: Phase averaged velocity field for characterization test with $f = 65$ Hz.
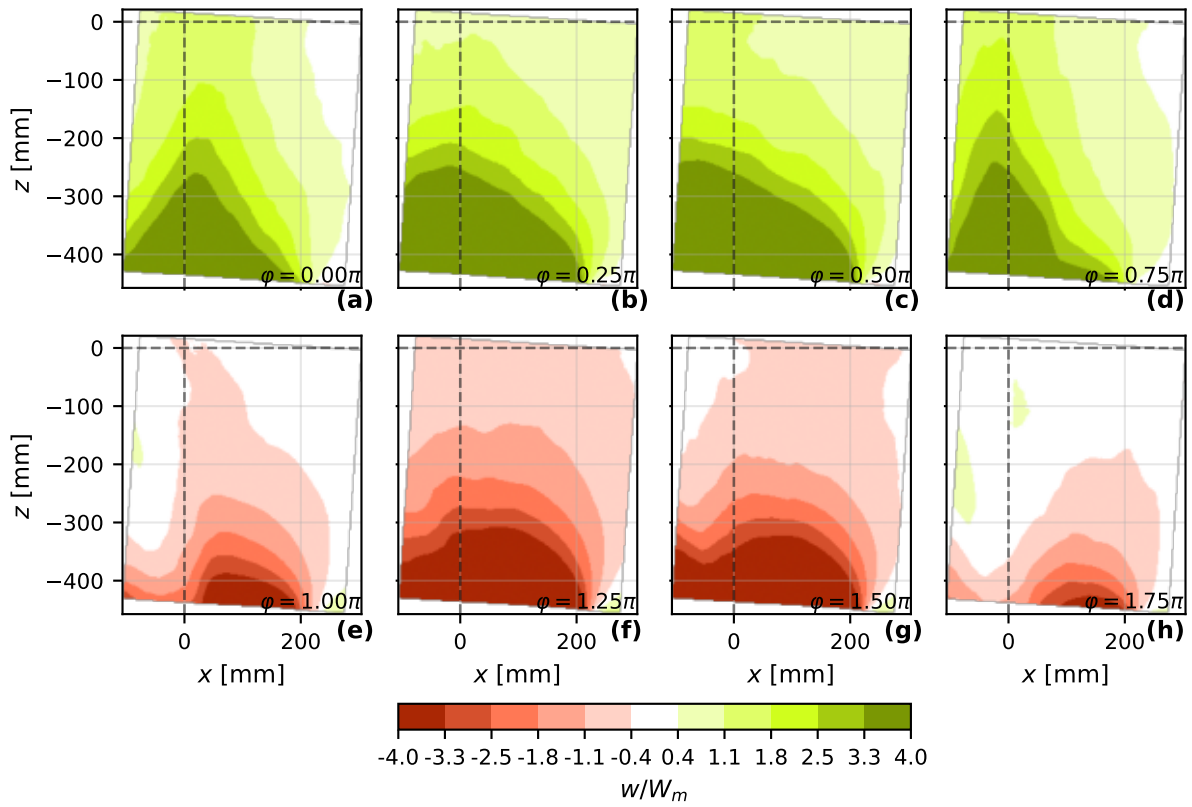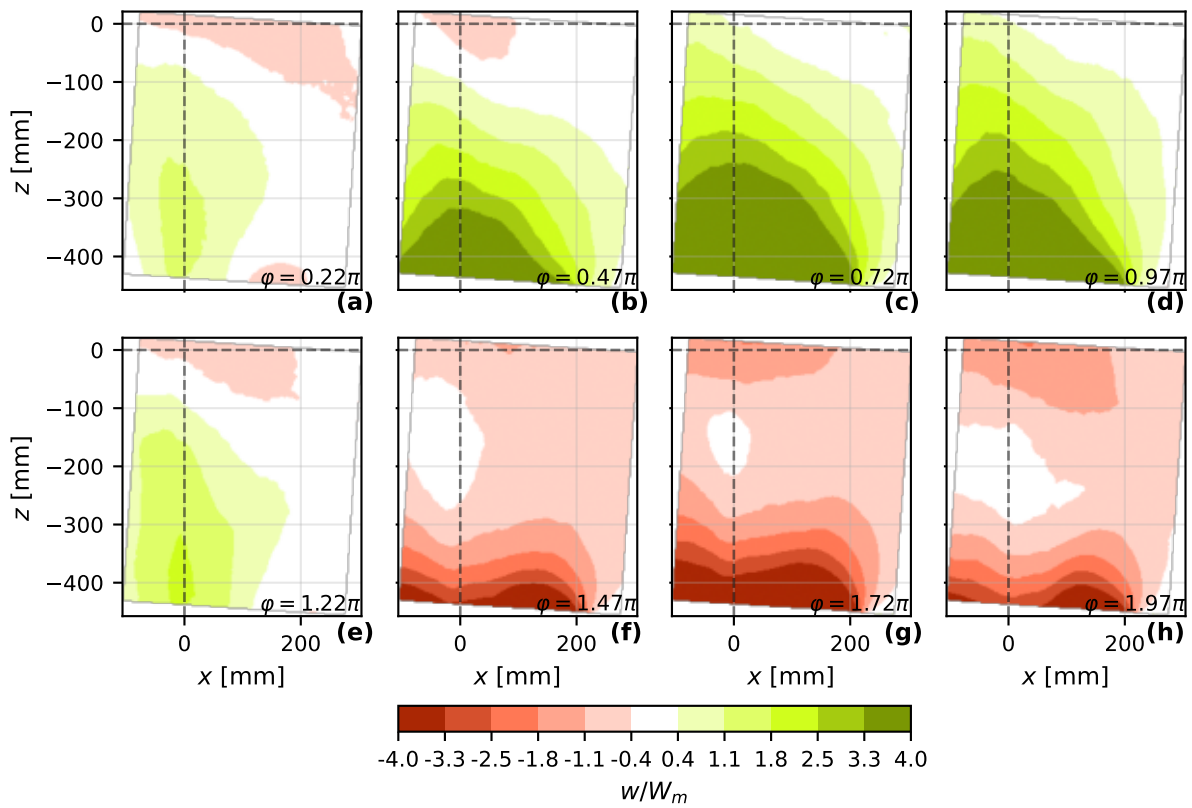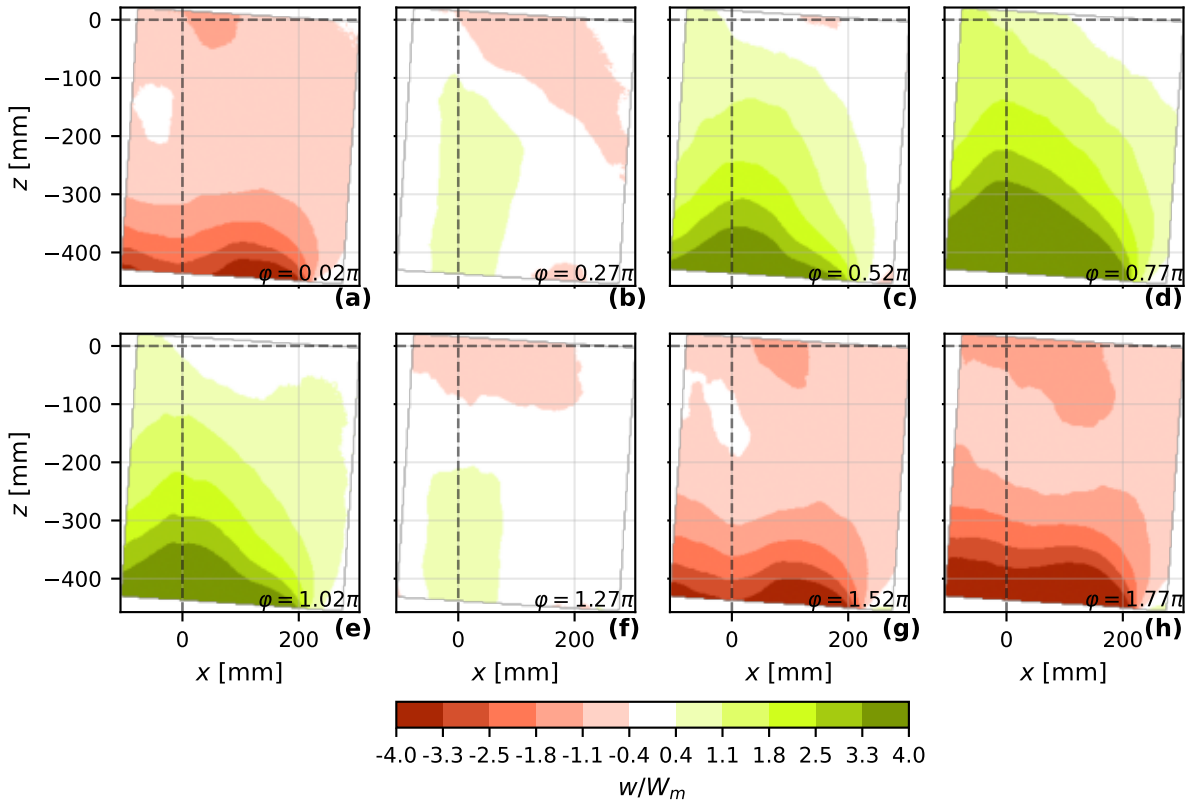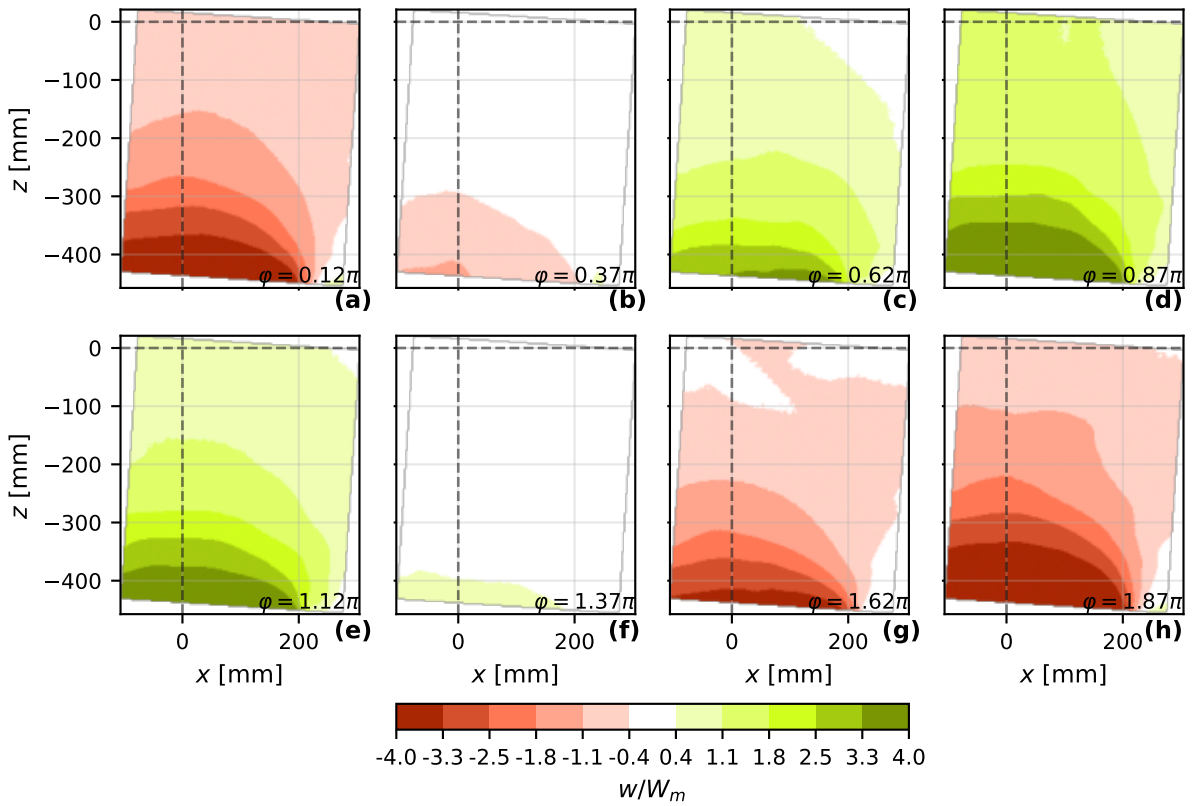

Figure C.4: Phase averaged velocity field for characterization test with $f = 100$ Hz.
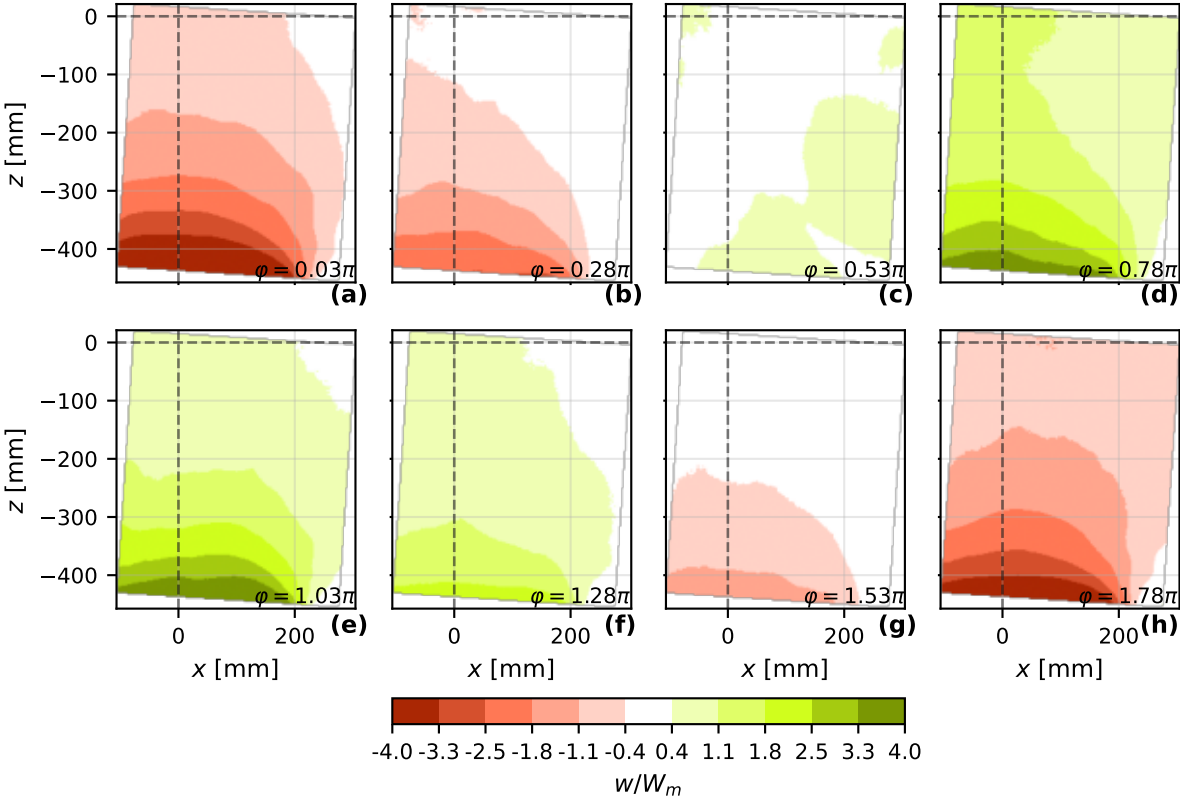
Figure C.5: Phase averaged velocity field for characterization test with $f = 146$ Hz.

C.2. Boundary layer characterization

The results of the boundary layer characterization is discussed in Section 4.1. This section provides some additional velocity fields and corresponding streamwise velocity profiles in Section C.2.1 and the turbulence statistics of the boundary layer are found in Section C.2.2.

C.2.1. Velocity in the boundary layer

The boundary layer was characterized using 5 planar PIV measurements with no forcing applied. The resulting velocity field of each measurement can be found in Figure C.6. The shape of the boundary layer is similar between all the measurements, indicating a stable boundary layer. Some development of the boundary layer can be seen, this is discussed in Section 4.1.3.

The velocity profiles corresponding to each measurement can be found in Figure C.7. The velocity of these profiles is obtained by averaging the velocity fields of Figure C.6 along the streamwise length of the p5020 PIV plane. The freestream velocity U_∞ is determined by taking the average of the profile with $y > 110$ mm. This value for the wall-normal coordinate was chosen to ensure sufficient distance from the boundary layer thickness δ_{99} while still having enough data to get an accurate average.

C.2.2. Turbulence statistics

The Reynolds stress tensor components were calculated for each measurement and are shown in Figures C.8a, C.9a, C.10a, C.11a and C.12a. The components containing the w' fluctuations are omitted as these can not be extracted from planar PIV. The stresses are similar throughout the Re_τ range, except for $\langle u'u' \rangle$ in the near wall region with $y^+ < 20$. This difference could be a result of the course interrogation window size used in these measurements.

The contributions to the TKE transport equation are shown in Figures C.8b, C.9b, C.10b, C.11b and C.12b. The pressure transport term is omitted as this requires the pressure fluctuations p' to be known and these can not accurately be determined from the acquired data. At low Re_τ the turbulent convection and mean flow convection terms feature significant noise in the wake region. This is likely a result of the course interrogation window having an effect on the gradient in the wall-normal direction.
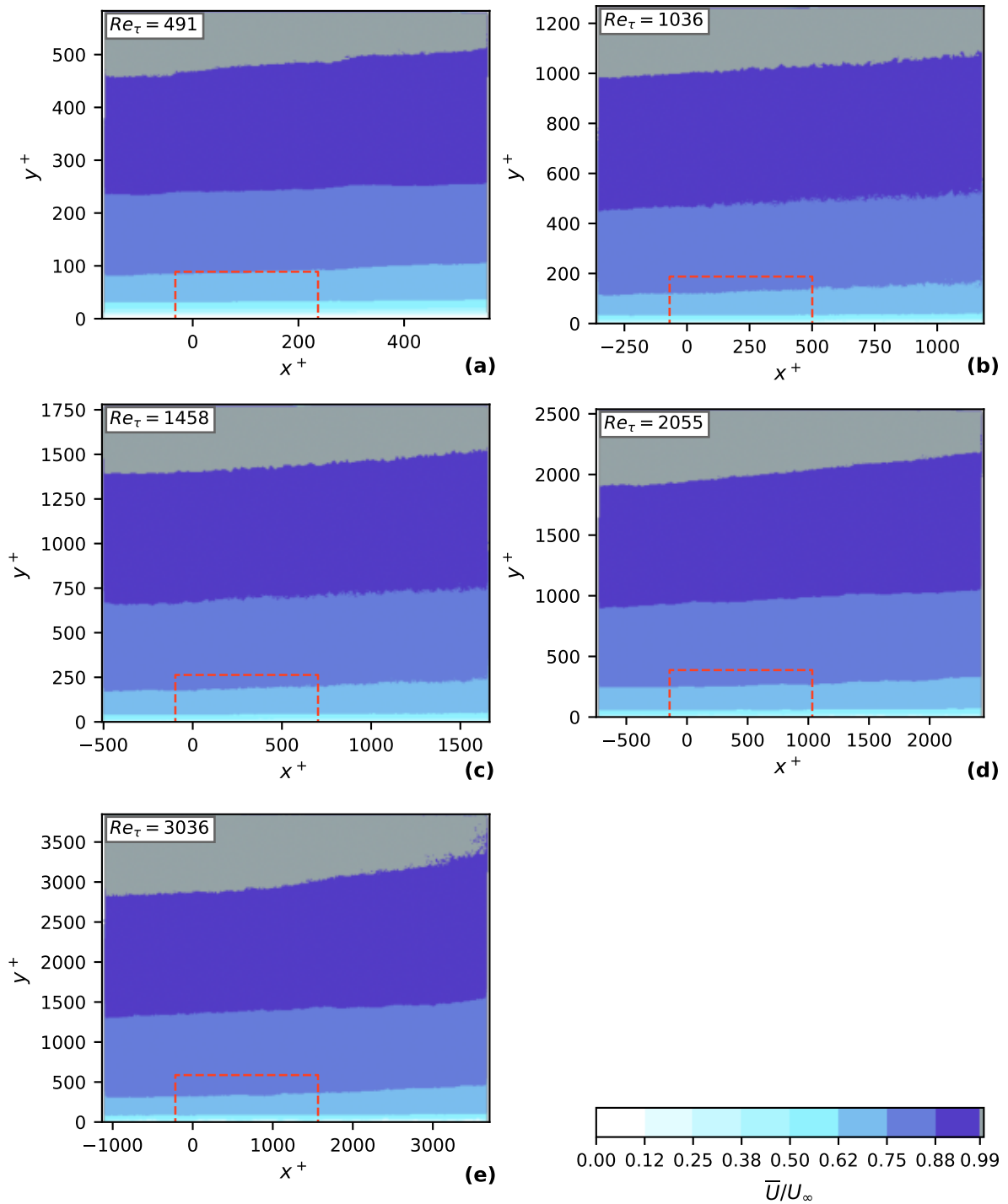
Figure C.6: Velocity magnitude for various Re_τ of the unforced boundary layer. The red dashed line marks the p5020 PIV plane FoV.
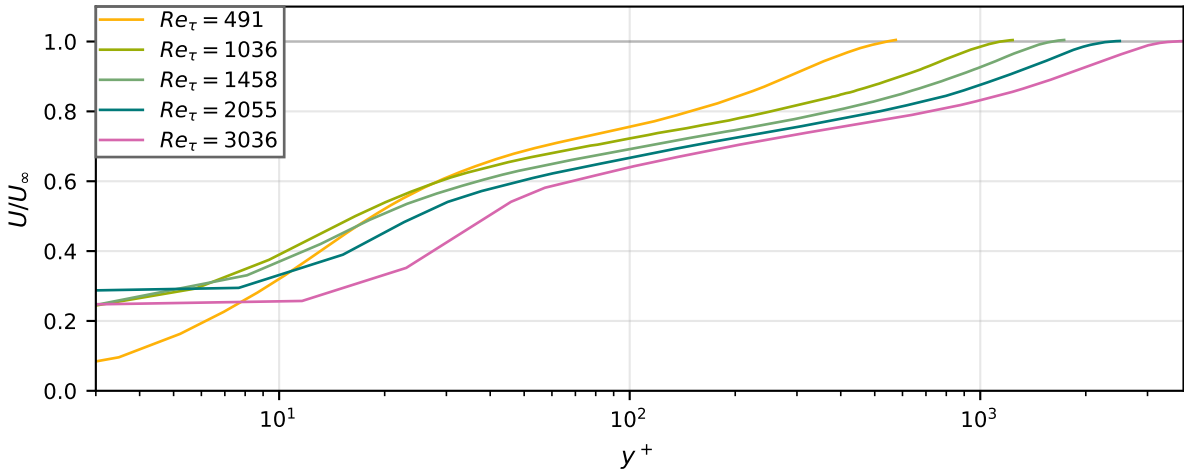
Figure C.7: Velocity profiles at various Re_τ of the unforced boundary layer.
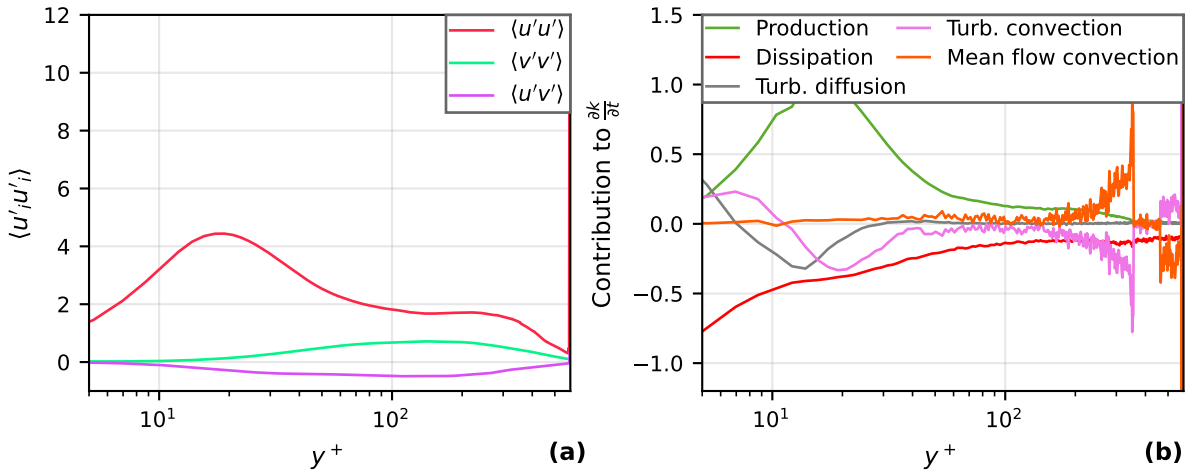
Figure C.8: (a) Reynolds stress tensor components in the wall normal direction for $Re_\tau = 491$. (b) Contribution to the time derivative of the turbulence kinetic energy.
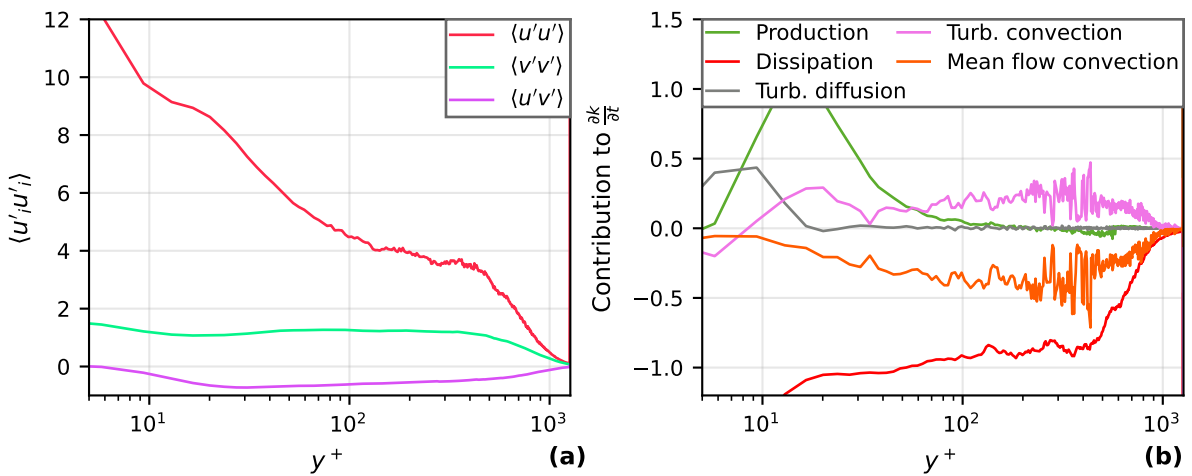
Figure C.9: (a) Reynolds stress tensor components in the wall normal direction for $Re_\tau = 1036$. (b) Contribution to the time derivative of the turbulence kinetic energy.
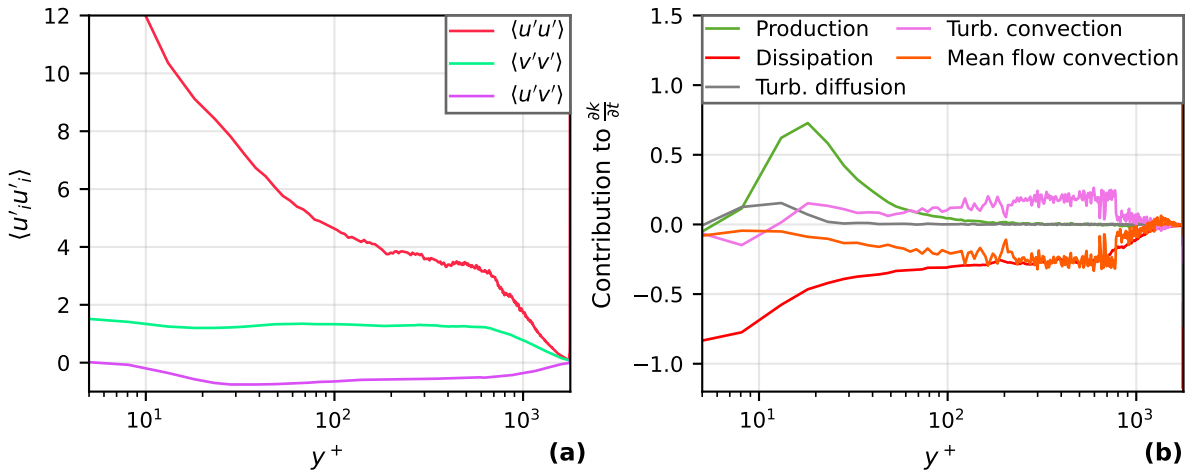
Figure C.10: (a) Reynolds stress tensor components in the wall normal direction for $Re_\tau = 1458$. (b) Contribution to the time derivative of the turbulence kinetic energy.

Figure C.11: (a) Reynolds stress tensor components in the wall normal direction for $Re_\tau = 2055$. (b) Contribution to the time derivative of the turbulence kinetic energy.

Figure C.12: (a) Reynolds stress tensor components in the wall normal direction for $Re_\tau = 3036$. (b) Contribution to the time derivative of the turbulence kinetic energy.

C.3. Drag reduction measurements

The results of the drag reduction measurements are discussed in Section 4.2. This section features additional velocity profile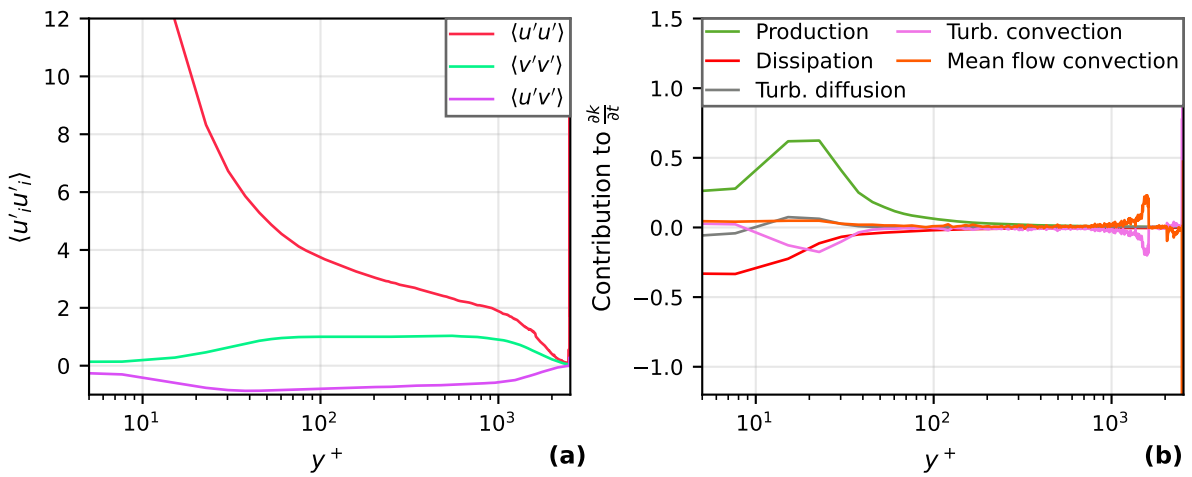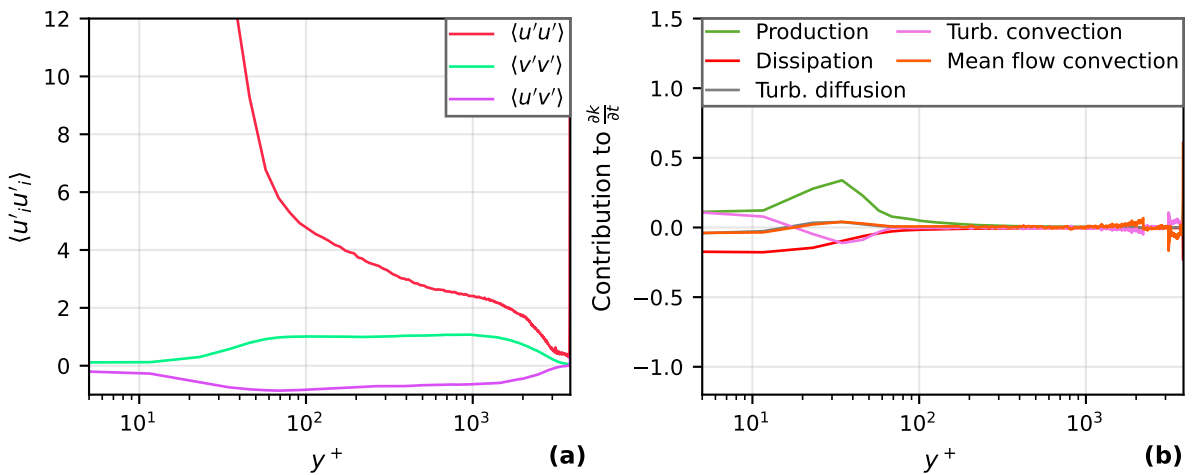s for all the measurements in Section C.3.1 for the streamwise direction and Section C.3.2 for the transverse direction. The turbulence statistics and their difference between the forced and unforced cases are shown in Section C.3.3.

C.3.1. Streamwise velocity profiles

The streamwise velocity profiles for all measurements are shown in this section. Figure C.13 shows the velocity profiles in the laminar sublayer with the slope used to calculate the friction velocity u_τ for the measurements with $T^+ \approx 100$. The full streamwise velocity profiles and their evolution over the phase of the forcing wave can be found in Figures C.16, C.17, C.18, C.19, C.20 and C.21. The profiles at higher Re_τ feature a discontinuity in the velocity, this is attributed to the processing of the PIV data. The near wall region was processed using a small interrogation window for improved accuracy, while the rest of the domain was processed with a courser window to speed up processing time. The course window calculates the average velocity in the entire window, and due to the non-linear gradient in the wall-normal direction this average is slightly higher with a larger window. The calculated forcing parameters, atmospheric conditions and drag reduction are found in Tables C.1, C.2, C.3, C.4, C.5 and C.6.

Figure C.14 shows the velocity profiles in the laminar sublayer with the slope used to calculate the friction velocity u_τ for the measurements with $T^+ \approx 120$. The full streamwise velocity profiles and their evolution over the phase of the forcing wave can be found in Figures C.22, C.23, C.24 and C.25. The calculated forcing parameters, atmospheric conditions and drag reduction are found in Tables C.7, C.8, C.9 and C.10.

Figure C.15 shows the velocity profiles in the laminar sublayer with the slope used to calculate the friction velocity u_τ for the measurements with $T^+ \approx 120$ and $W_m^+ \approx 0.70$. The full streamwise velocity profiles and their evolution over the phase of the forcing wave can be found in Figures C.26, C.27, C.28 and C.29. The calculated forcing parameters, atmospheric conditions and drag reduction are found in Tables C.11, C.12, C.13 and C.14.

Figure C.13: Detail of the streamwise velocity profiles in the laminar sublayer for the measurements with $T^+ \approx 100$, with their drag reduction shown in Figure 4.5. The ● indicating the unforced case and ▲ the forced case, the dashed lines indicate the measured slope used to calculate u_τ and the shaded area shows the standard error.
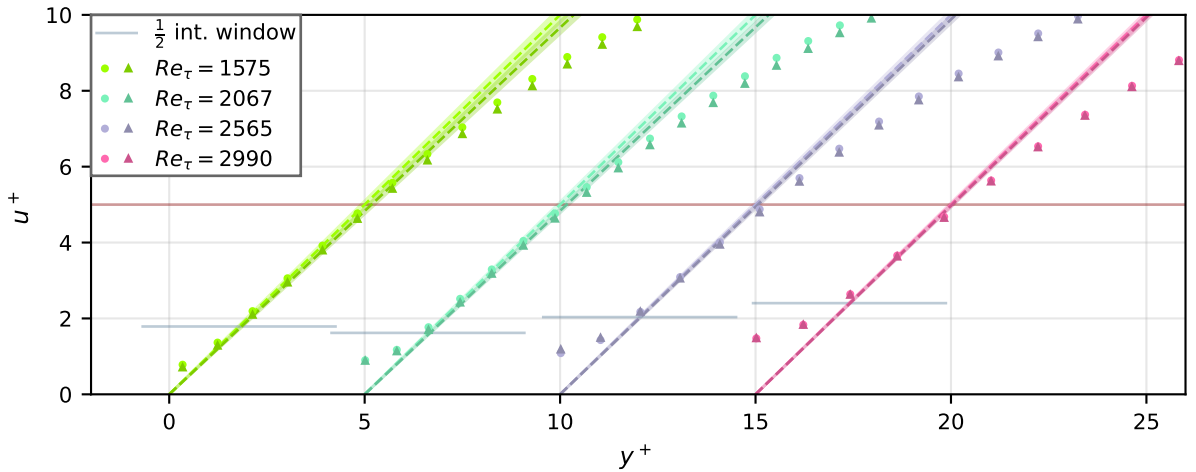
Figure C.14: Detail of the streamwise velocity profiles in the laminar sublayer for the measurements with $T^+ \approx 120$, with their drag reduction shown in Figure 4.6. The ● indicating the unforced case and ▲ the forced case, the dashed lines indicate the measured slope used to calculate u_τ and the shaded area shows the standard error.

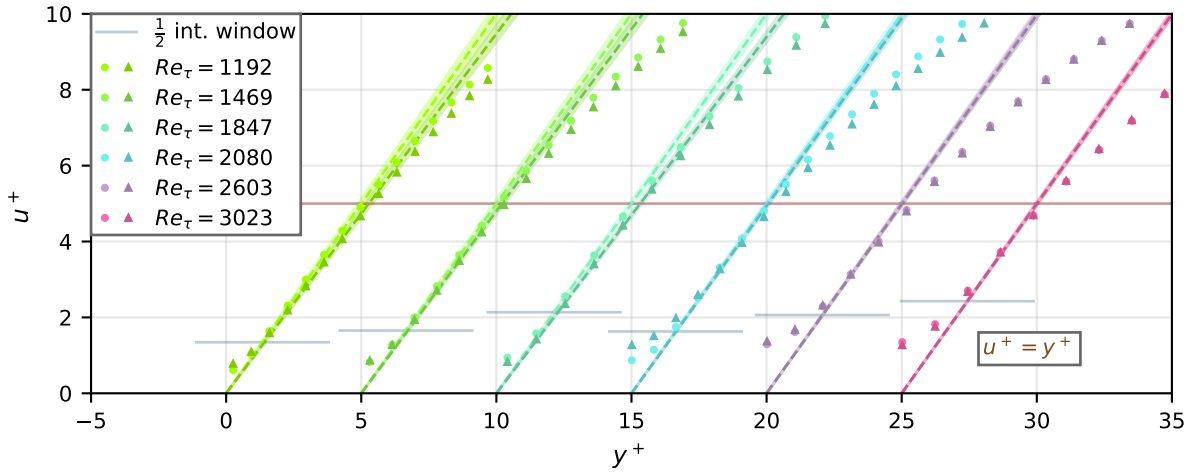**Figure C.15:** Detail of the streamwise velocity profiles in the laminar sublayer for the measurements with $T^+ \approx 120$ and $W_m^+ \approx 0.7$, with their drag reduction shown in Figure 4.7. The ● indicating the unforced case and ▲ the forced case, the dashed lines indicate the measured slope used to calculate u_τ and the shaded area shows the standard error.
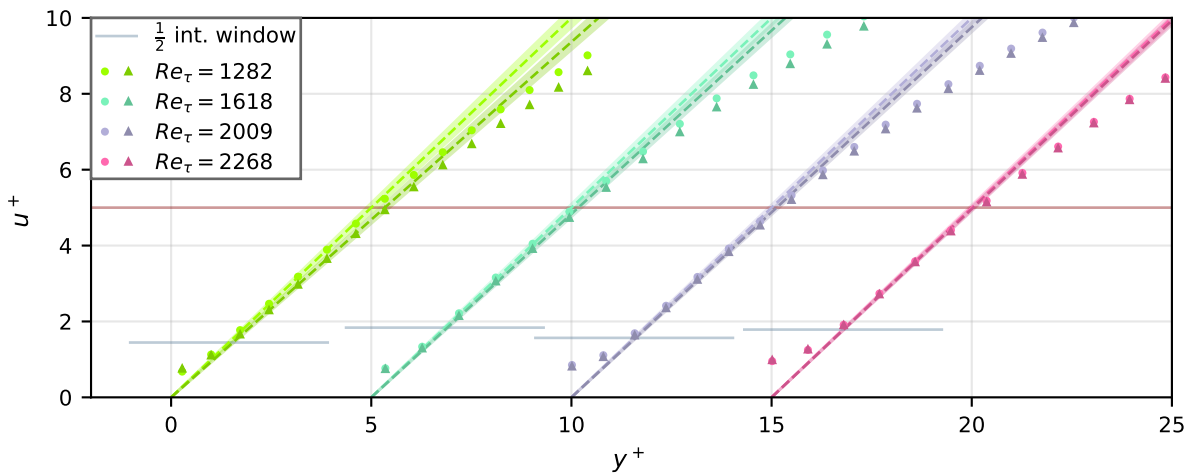
N	Re_τ	$\mathcal{R}$	C_f	T^+	W_m^+	u_τ
14	1192		$3.3433e-03$			0.174
15	1161	0.0579	$3.1497e-03$	95.3	1.18	0.169

N	U_∞	ν	T	p_a	ρ	int. win
14	4.26	$1.507e-05$	21.10	1020.8	1.2065	$12 \times 12\ 75\%ov$
15	4.27	$1.507e-05$	21.07	1020.7	1.2065	$12 \times 12\ 75\%ov$

Table C.1: Test conditions and results for measurement the measurement pair at $Re_\tau = 1192$.

Figure C.16: (a) Streamwise velocity profile of the reference and forced measurement with $Re_\tau = 1192$. (b) Streamwise velocity profiles at various instances of the phase, the reference profile is shown with the dashed line.
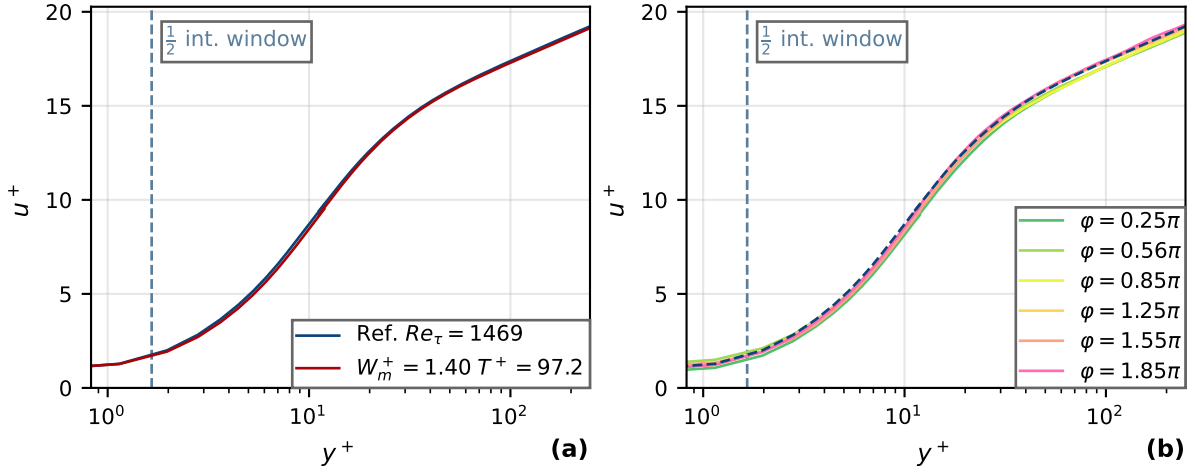
Figure C.17: (a) Streamwise velocity profile of the reference and forced measurement with $Re_\tau = 1469$. (b) Streamwise velocity profiles at various instances of the phase, the reference profile is shown with the dashed line.

N	Re_τ	$\mathcal{R}$	C_f	T^+	W_m^+	u_τ
16	1469		$3.1201e-03$			0.214
17	1439	0.0477	$2.9713e-03$	97.2	1.40	0.210

N	U_∞	ν	T	p_a	ρ	int. win
16	5.42	$1.507e-05$	21.07	1020.6	1.2064	$12 \times 12\ 75\%ov$
17	5.44	$1.507e-05$	21.07	1020.6	1.2064	$12 \times 12\ 75\%ov$

Table C.2: Test conditions and results for measurement the measurement pair at $Re_\tau = 1469$.

Figure C.18: (a) Streamwise velocity profile of the reference and forced measurement with $Re_\tau = 1847$. (b) Streamwise velocity profiles at various instances of the phase, the reference profile is shown with the dashed line.

N	Re_τ	$\mathcal{R}$	C_f	T^+	W_m^+	u_τ
18	1847		$2.8888e-03$			0.276
19	1790	0.0602	$2.7149e-03$	95.2	1.10	0.268

N	U_∞	ν	T	p_a	ρ	int. win
18	7.27	$1.508e-05$	21.07	1020.5	1.2063	12×12 75%ov
19	7.27	$1.508e-05$	21.09	1020.5	1.2062	12×12 75%ov

Table C.3: Test conditions and results for measurement the measurement pair at $Re_\tau = 1847$.
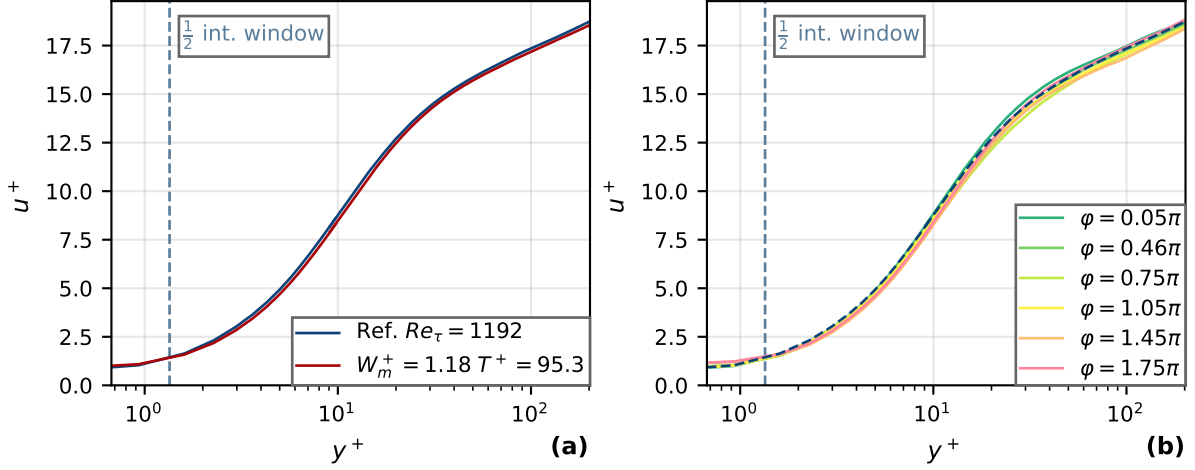

Figure C.19: (a) Streamwise velocity profile of the reference and forced measurement with $Re_\tau = 2080$. (b) Streamwise velocity profiles at various instances of the phase, the reference profile is shown with the dashed line.

N	Re_τ	$\mathcal{R}$	C_f	T^+	W_m^+	u_τ
20	2080		$2.8132e-03$			0.317
21	2067	0.0132	$2.7762e-03$	100.9	0.87	0.315

N	U_∞	ν	T	p_a	ρ	int. win
20	8.44	$1.508e-05$	21.11	1020.3	1.2059	8×8 75%ov
21	8.44	$1.508e-05$	21.11	1020.3	1.2059	8×8 75%ov

Table C.4: Test conditions and results for measurement the measurement pair at $Re_\tau = 2080$.
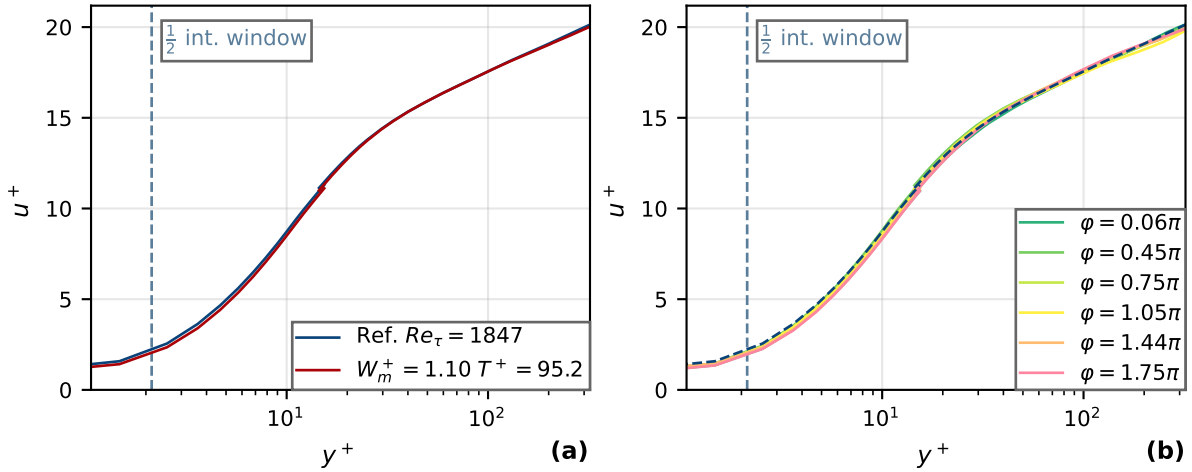
Figure C.20: (a) Streamwise velocity profile of the reference and forced measurement with $Re_\tau = 2603$. (b) Streamwise velocity profiles at various instances of the phase, the reference profile is shown with the dashed line.

N	Re_τ	$\mathcal{R}$	C_f	T^+	W_m^+	u_τ
22	2603		$2.8030e-03$			0.401
23	2597	0.0047	$2.7899e-03$	106.2	0.38	0.400

N	U_∞	ν	T	p_a	ρ	int. win
22	10.71	$1.508e-05$	21.13	1020.3	1.2058	$8 \times 8\ 75\%ov$
23	10.72	$1.509e-05$	21.17	1020.3	1.2056	$8 \times 8\ 75\%ov$

Table C.5: Test conditions and results for measurement the measurement pair at $Re_\tau = 2603$.
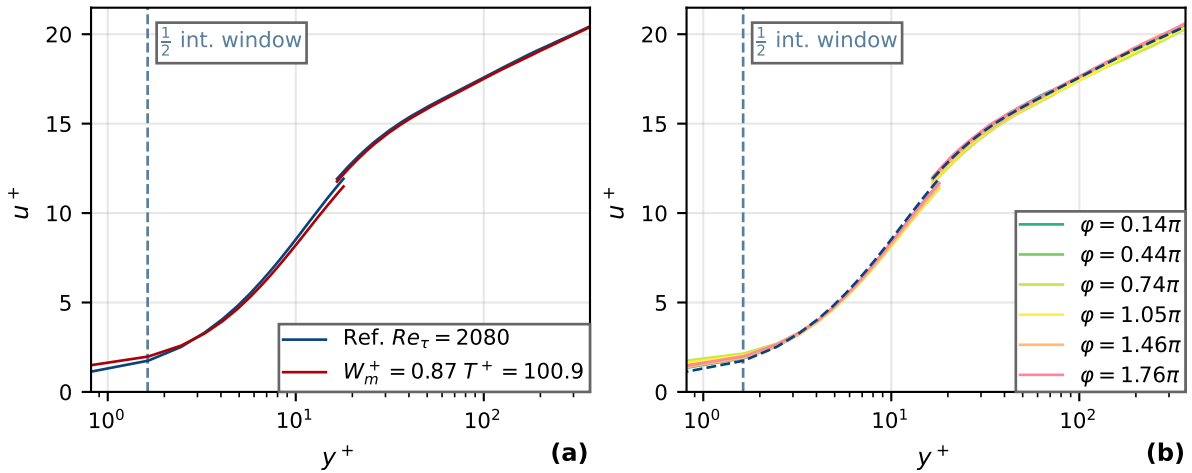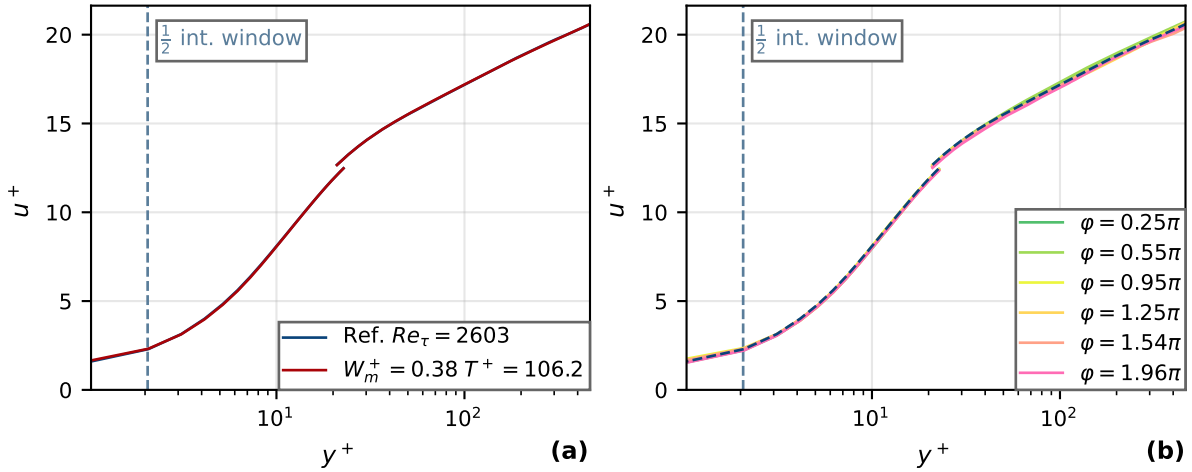

Figure C.21: (a) Streamwise velocity profile of the reference and forced measurement with $Re_\tau = 3023$. (b) Streamwise velocity profiles at various instances of the phase, the reference profile is shown with the dashed line.

N	Re_τ	$\mathcal{R}$	C_f	T^+	W_m^+	u_τ
24	3023		$2.6046e-03$			0.474
25	3017	-0.0040	$2.6149e-03$	101.3	0.32	0.474

N	U_∞	ν	T	p_a	ρ	int. win
24	13.14	$1.517e-05$	20.99	1013.9	1.1988	$8 \times 8\ 75\%ov$
25	13.11	$1.518e-05$	21.14	1013.6	1.1979	$8 \times 8\ 75\%ov$

Table C.6: Test conditions and results for measurement the measurement pair at $Re_\tau = 3023$.
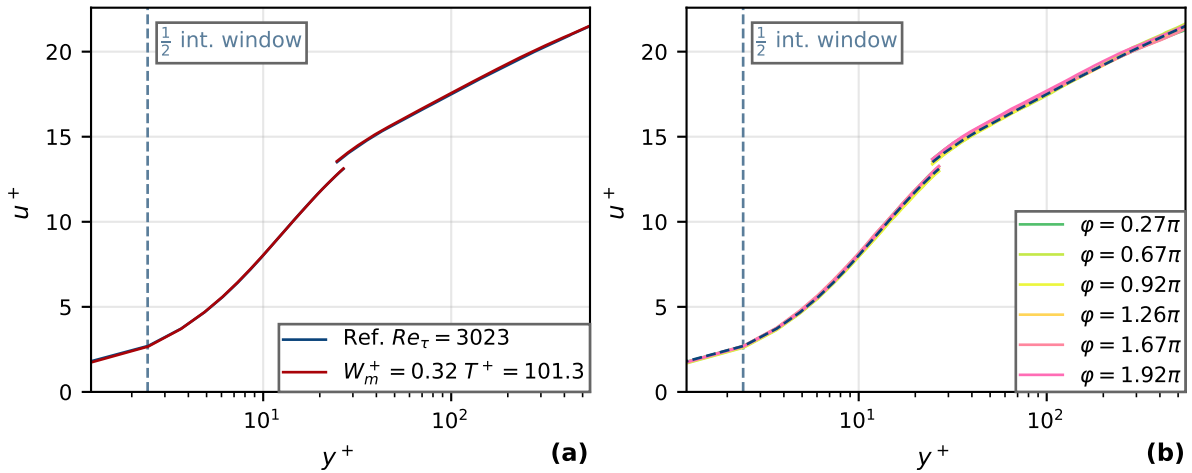
Figure C.22: (a) Streamwise velocity profile of the reference and forced measurement with $Re_\tau = 1575$. (b) Streamwise velocity profiles at various instances of the phase, the reference profile is shown with the dashed line.

N	Re_τ	$\mathcal{R}$	C_f	T^+	W_m^+	u_τ
46	1575		$3.0431e-03$			0.235
47	1548	0.0280	$2.9580e-03$	117.3	1.26	0.231

N	U_∞	ν	T	p_a	ρ	int. win
46	6.02	$1.531e-05$	21.72	1009.1	1.1901	12×12 75%ov
47	6.00	$1.530e-05$	21.68	1008.9	1.1901	12×12 75%ov

Table C.7: Test conditions and results for measurement the measurement pair at $Re_\tau = 1575$.
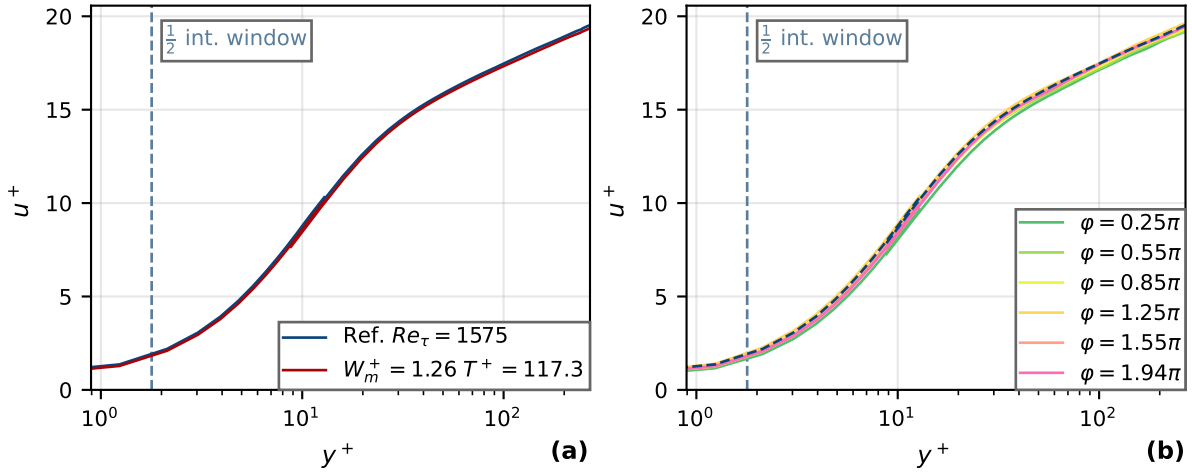

Figure C.23: (a) Streamwise velocity profile of the reference and forced measurement with $Re_\tau = 2067$. (b) Streamwise velocity profiles at various instances of the phase, the reference profile is shown with the dashed line.

N	Re_τ	$\mathcal{R}$	C_f	T^+	W_m^+	u_τ
48	2067		$2.8772e-03$			0.319
49	2033	0.0273	$2.7987e-03$	120.5	0.97	0.314

N	U_∞	ν	T	p_a	ρ	int. win
48	8.41	$1.531e-05$	21.67	1008.7	1.1900	8×8 75%ov
49	8.39	$1.531e-05$	21.68	1008.6	1.1897	8×8 75%ov

Table C.8: Test conditions and results for measurement the measurement pair at $Re_\tau = 2067$.
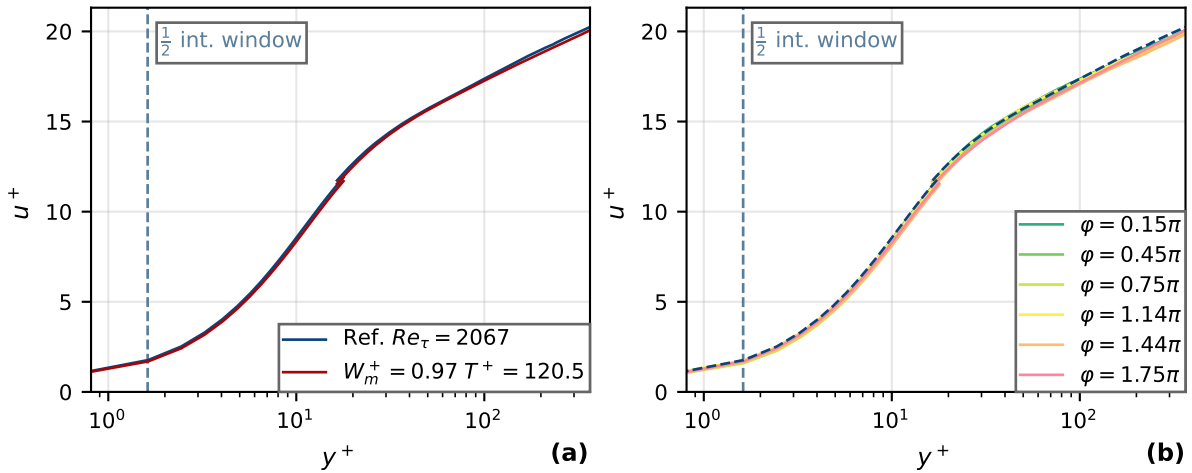
Figure C.24: (a) Streamwise velocity profile of the reference and forced measurement with $Re_\tau = 2565$. (b) Streamwise velocity profiles at various instances of the phase, the reference profile is shown with the dashed line.

N	Re_τ	$\mathcal{R}$	C_f	T^+	W_m^+	u_τ
50	2565		$2.7729e-03$			0.401
51	2549	0.0098	$2.7456e-03$	123.7	0.48	0.399

N	U_∞	ν	T	p_a	ρ	int. win
50	10.78	$1.532e-05$	21.73	1008.5	1.1894	8×8 75%ov
51	10.77	$1.532e-05$	21.77	1008.4	1.1892	8×8 75%ov

Table C.9: Test conditions and results for measurement the measurement pair at $Re_\tau = 2565$.
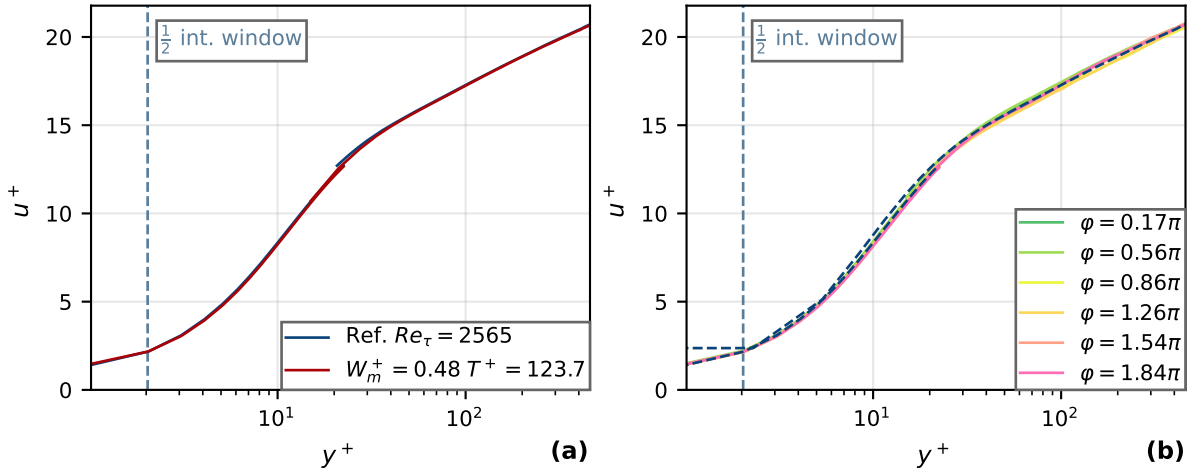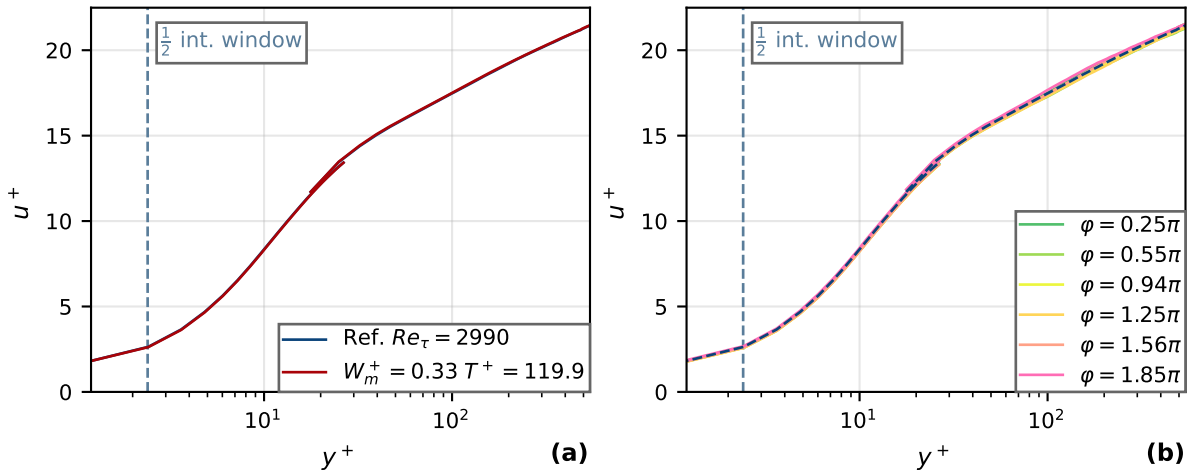

Figure C.25: (a) Streamwise velocity profile of the reference and forced measurement with $Re_\tau = 2990$. (b) Streamwise velocity profiles at various instances of the phase, the reference profile is shown with the dashed line.

N	Re_τ	$\mathcal{R}$	C_f	T^+	W_m^+	u_τ
52	2990		$2.6147e-03$			0.474
53	2980	0.0078	$2.5943e-03$	119.9	0.33	0.473

N	U_∞	ν	T	p_a	ρ	int. win
52	13.12	$1.533e-05$	21.82	1008.3	1.1889	8×8 75%ov
53	13.13	$1.533e-05$	21.88	1008.3	1.1886	8×8 75%ov

Table C.10: Test conditions and results for measurement the measurement pair at $Re_\tau = 2990$.
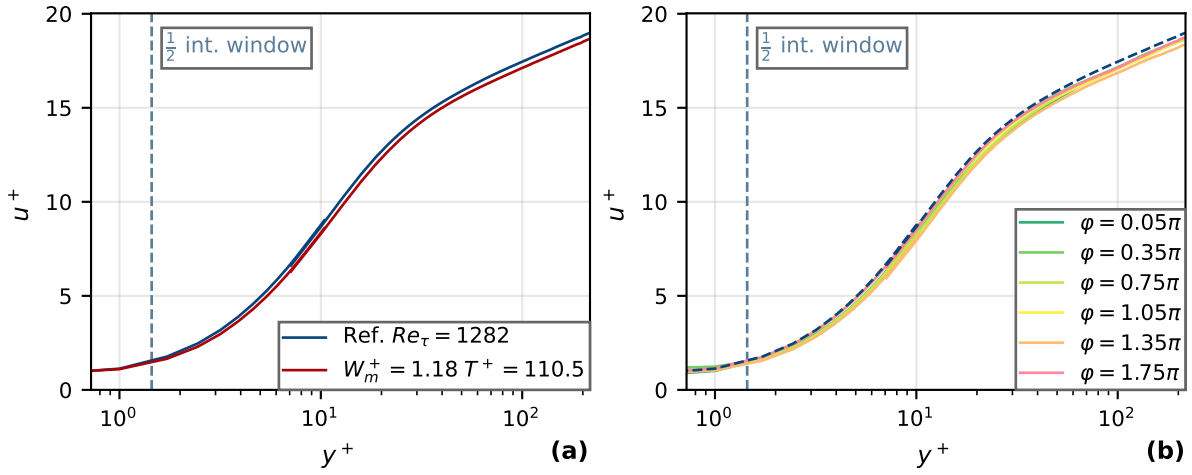
Figure C.26: (a) Streamwise velocity profile of the reference and forced measurement with $Re_\tau = 1282$. (b) Streamwise velocity profiles at various instances of the phase, the reference profile is shown with the dashed line.

N	Re_τ	$\mathcal{R}$	C_f	T^+	W_m^+	u_τ
58	1282		$3.1968e-03$			0.190
59	1241	0.0683	$2.9786e-03$	110.5	1.18	0.184

N	U_∞	ν	T	p_a	ρ	int. win
58	4.76	$1.533e-05$	21.87	1008.1	1.1885	$12 \times 12\ 75\%ov$
59	4.77	$1.533e-05$	21.82	1008.0	1.1885	$12 \times 12\ 75\%ov$

Table C.11: Test conditions and results for measurement the measurement pair at $Re_\tau = 1282$.
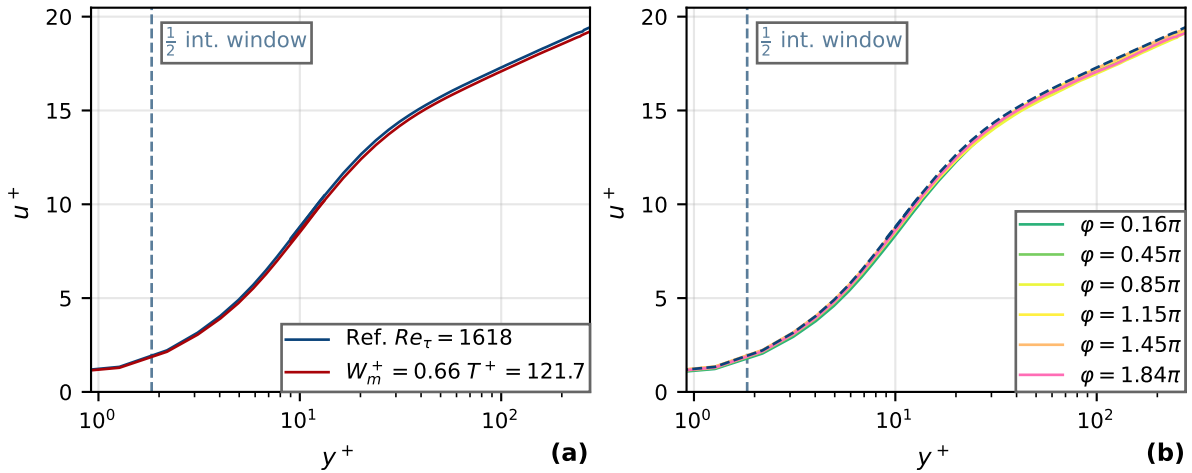

Figure C.27: (a) Streamwise velocity profile of the reference and forced measurement with $Re_\tau = 1618$. (b) Streamwise velocity profiles at various instances of the phase, the reference profile is shown with the dashed line.

N	Re_τ	$\mathcal{R}$	C_f	T^+	W_m^+	u_τ
60	1618		$3.1314e-03$			0.240
61	1590	0.0311	$3.0340e-03$	121.7	0.66	0.236

N	U_∞	ν	T	p_a	ρ	int. win
60	6.06	$1.519e-05$	21.55	1015.5	1.1984	$12 \times 12\ 75\%ov$
61	6.05	$1.520e-05$	21.58	1015.6	1.1983	$12 \times 12\ 75\%ov$

Table C.12: Test conditions and results for measurement the measurement pair at $Re_\tau = 1618$.
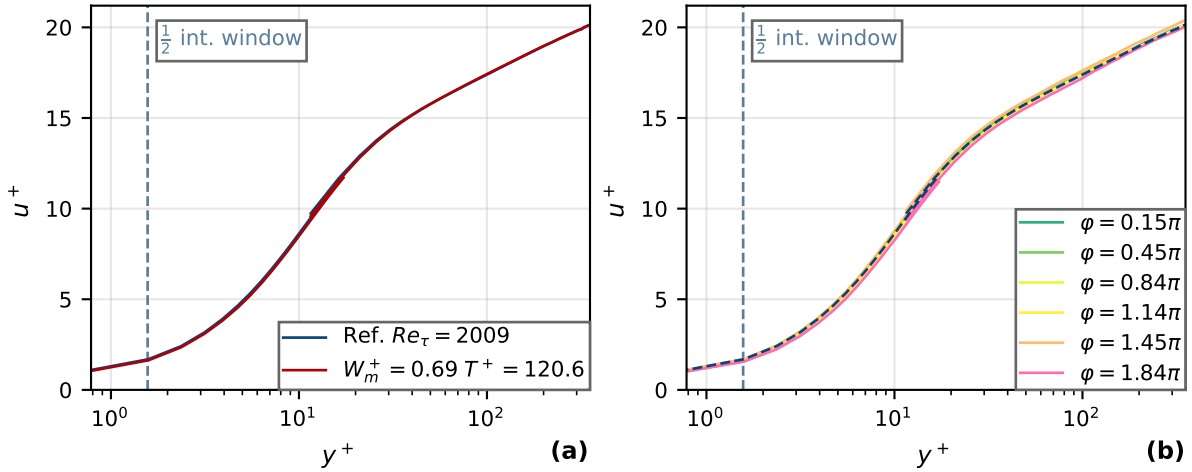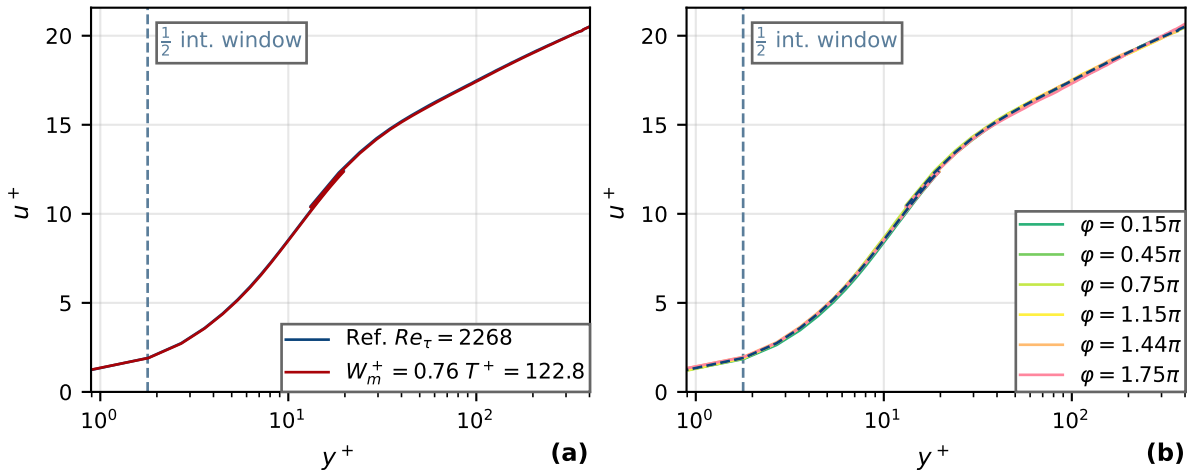
Figure C.28: (a) Streamwise velocity profile of the reference and forced measurement with $Re_\tau = 2009$. (b) Streamwise velocity profiles at various instances of the phase, the reference profile is shown with the dashed line.

N	Re_τ	$\mathcal{R}$	C_f	T^+	W_m^+	u_τ
62	2009		$2.8835e-03$			0.307
63	1984	0.0251	$2.8112e-03$	120.6	0.69	0.303

N	U_∞	ν	T	p_a	ρ	int. win
62	8.08	$1.520e-05$	21.61	1015.7	1.1983	$8 \times 8\ 75\%ov$
63	8.08	$1.520e-05$	21.66	1015.7	1.1982	$8 \times 8\ 75\%ov$

Table C.13: Test conditions and results for measurement the measurement pair at $Re_\tau = 2009$.

Figure C.29: (a) Streamwise velocity profile of the reference and forced measurement with $Re_\tau = 2268$. (b) Streamwise velocity profiles at various instances of the phase, the reference profile is shown with the dashed line.

N	Re_τ	$\mathcal{R}$	C_f	T^+	W_m^+	u_τ
64	2268		$2.8101e-03$			0.350
65	2259	0.0122	$2.7759e-03$	122.8	0.76	0.348

N	U_∞	ν	T	p_a	ρ	int. win
64	9.33	$1.521e-05$	21.73	1015.8	1.1980	$8 \times 8\ 75\%ov$
65	9.35	$1.521e-05$	21.78	1015.8	1.1979	$8 \times 8\ 75\%ov$

Table C.14: Test conditions and results for measurement the measurement pair at $Re_\tau = 2268$.

C.3.2. Transverse velocity profiles

The transverse velocity component w was extracted using the out-of-plane velocity from the Stereoscopic PIV measurements. This section shows the w-profiles and the phase averaged w for each measurement. The profiles corresponding to the drag reduction measurements with $T^+ \approx 100$, summarised in Figure 4.5, are shown in Figures C.30, C.31, C.32, C.33, C.34 and C.35. The measurements with $T^+ \approx 120$, summarised in Figure 4.6, are shown in Figures C.36, C.37, C.38 and C.39. Finally the measurements with $T^+ \approx 120$ and $W_m^+ \approx 0.70$, summarised in Figure 4.7, are shown in Figures C.40, C.41, C.42 and C.43. Some profiles show non-zero w velocity in the near wall region, this is because the streamwise velocity is low in this region, reducing the accuracy of the PIV cross-correlation algorithm.
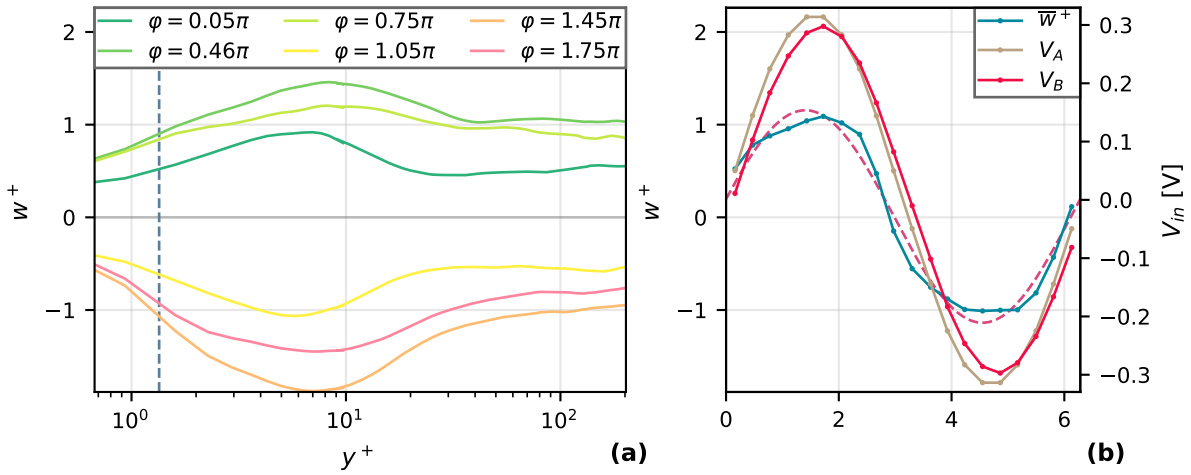
Figure C.30: (a) transverse velocity profiles at various instances of the phase with $Re_\tau = 1192$. (b) The average transverse velocity over the phase. The dashed line marks the sinusoidal fit used to extract $W_m^+ = 1.18$. The voltage signal to the speakers is also shown.
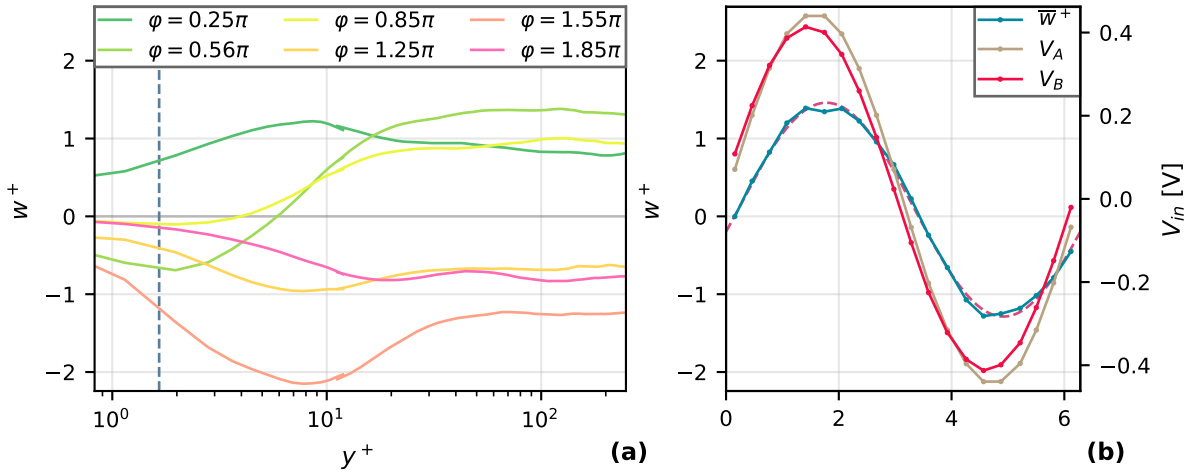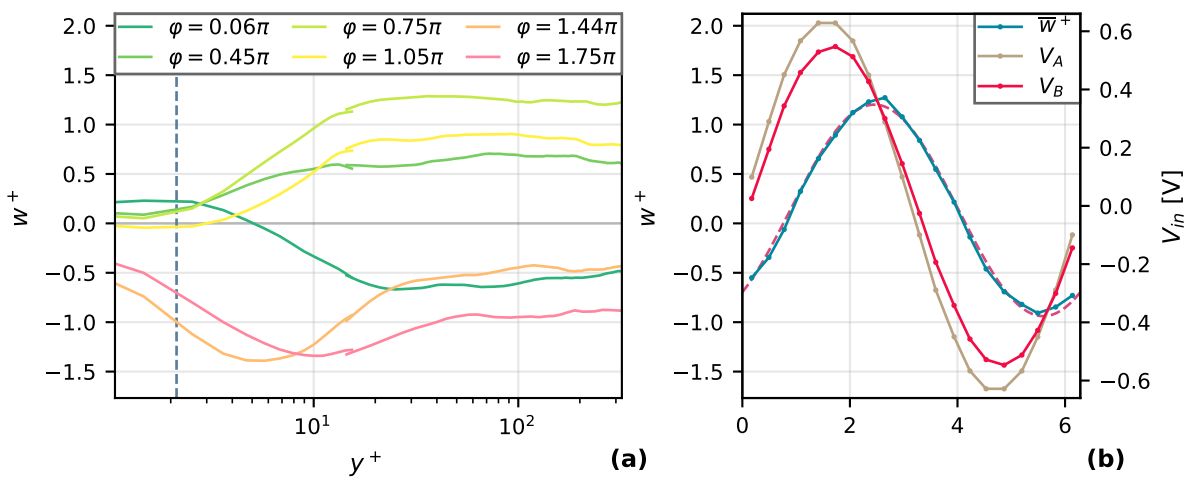

Figure C.31: (a) transverse velocity profiles at various instances of the phase with $Re_\tau = 1469$. (b) The average transverse velocity over the phase. The dashed line marks the sinusoidal fit used to extract $W_m^+ = 1.40$. The voltage signal to the speakers is also shown.
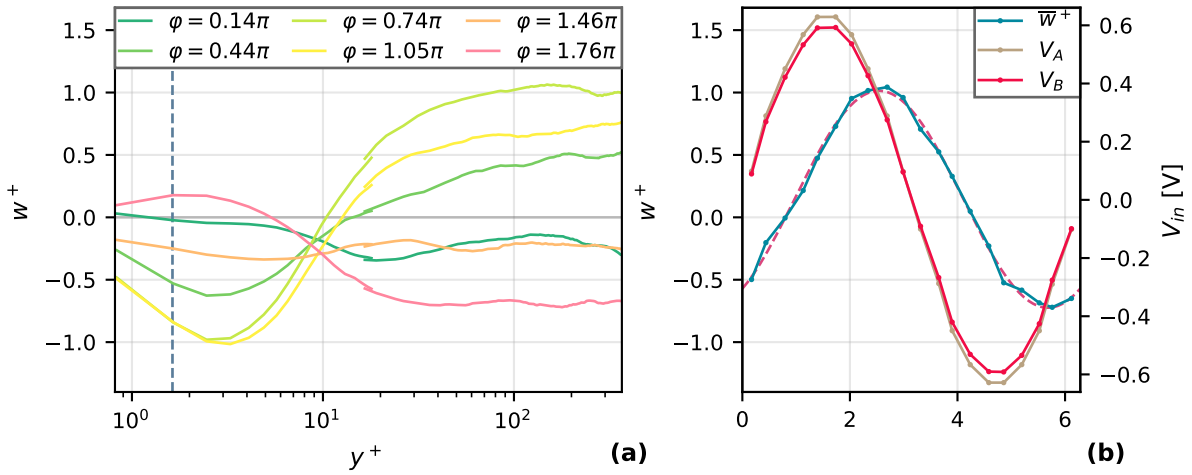

Figure C.32: (a) transverse velocity profiles at various instances of the phase with $Re_\tau = 1847$. (b) The average transverse velocity over the phase. The dashed line marks the sinusoidal fit used to extract $W_m^+ = 1.10$. The voltage signal to the speakers is also shown.
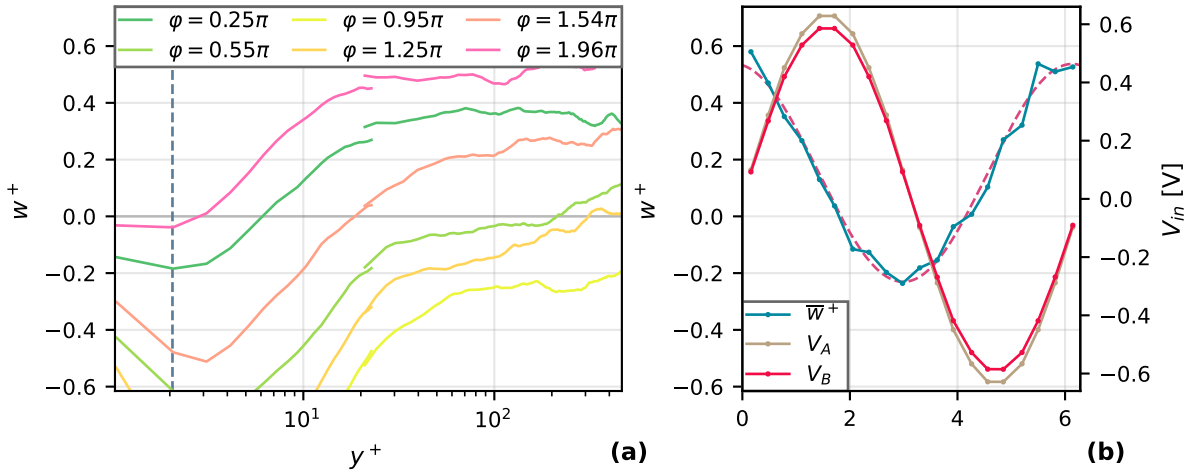
Figure C.33: (a) transverse velocity profiles at various instances of the phase with $Re_\tau = 2080$. (b) The average transverse velocity over the phase. The dashed line marks the sinusoidal fit used to extract $W_m^+ = 0.87$. The voltage signal to the speakers is also shown.
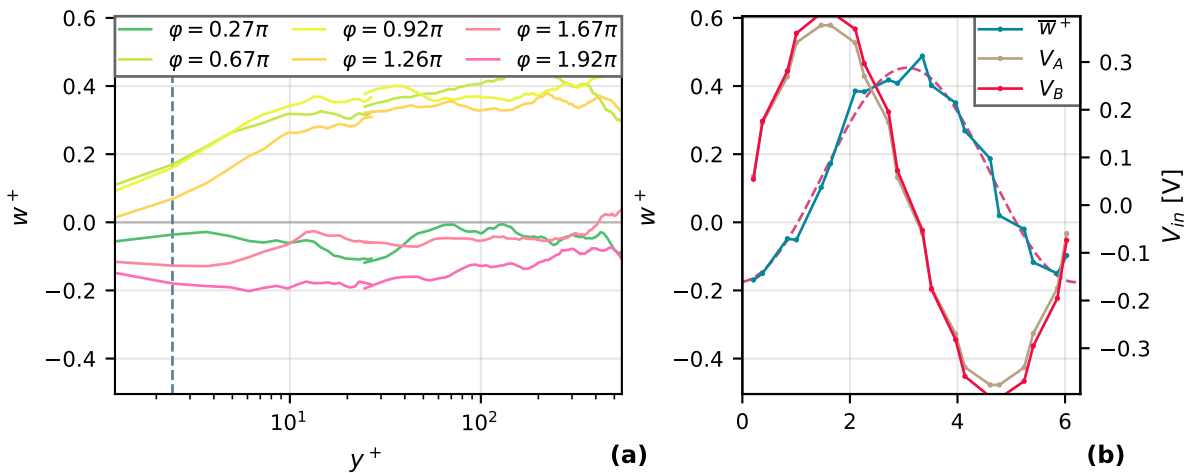

Figure C.34: (a) transverse velocity profiles at various instances of the phase with $Re_\tau = 2603$. (b) The average transverse velocity over the phase. The dashed line marks the sinusoidal fit used to extract $W_m^+ = 0.38$. The voltage signal to the speakers is also shown.

Figure C.35: (a) transverse velocity profiles at various instances of the phase with $Re_\tau = 3023$. (b) The average transverse velocity over the phase. The dashed line marks the sinusoidal fit used to extract $W_m^+ = 0.32$. The voltage signal to the speakers is also shown.
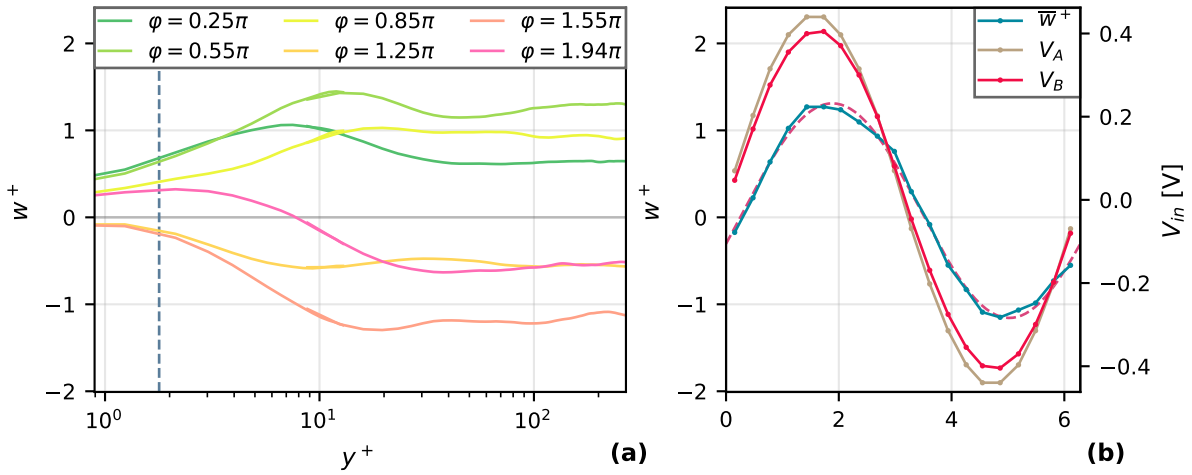
Figure C.36: (a) transverse velocity profiles at various instances of the phase with $Re_\tau = 1575$. (b) The average transverse velocity over the phase. The dashed line marks the sinusoidal fit used to extract $W_m^+ = 1.26$. The voltage signal to the speakers is also shown.
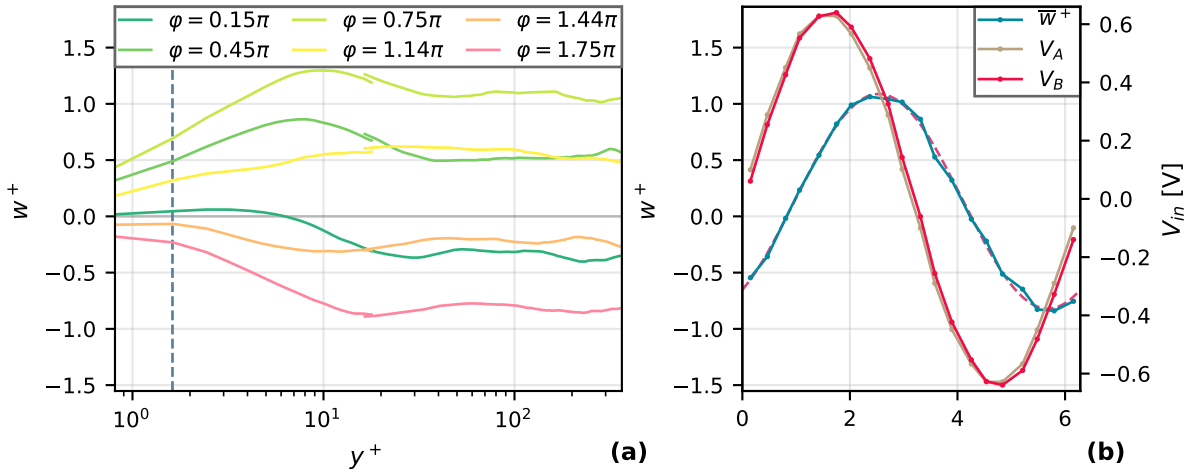

Figure C.37: (a) transverse velocity profiles at various instances of the phase with $Re_\tau = 2067$. (b) The average transverse velocity over the phase. The dashed line marks the sinusoidal fit used to extract $W_m^+ = 0.97$. The voltage signal to the speakers is also shown.
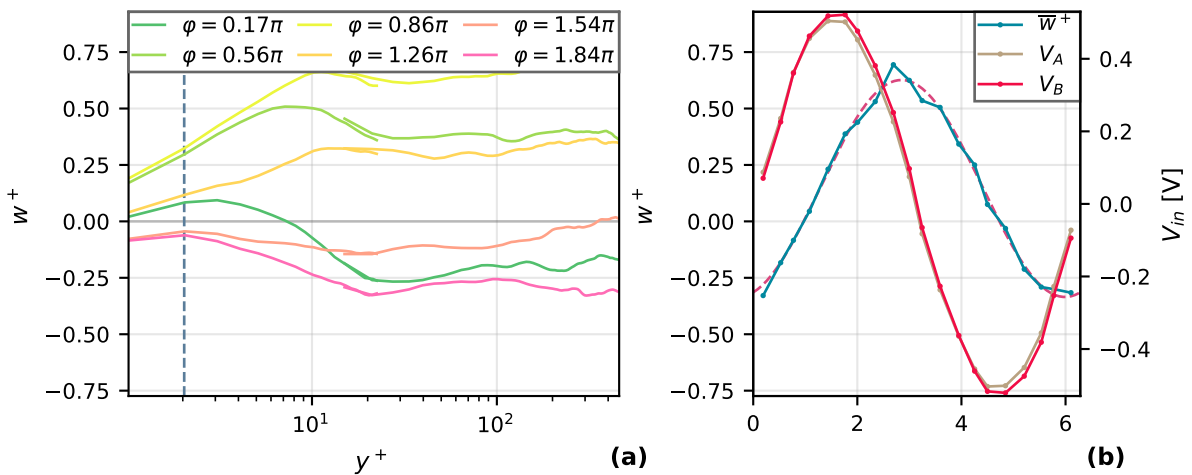

Figure C.38: (a) transverse velocity profiles at various instances of the phase with $Re_\tau = 2565$. (b) The average transverse velocity over the phase. The dashed line marks the sinusoidal fit used to extract $W_m^+ = 0.48$. The voltage signal to the speakers is also shown.
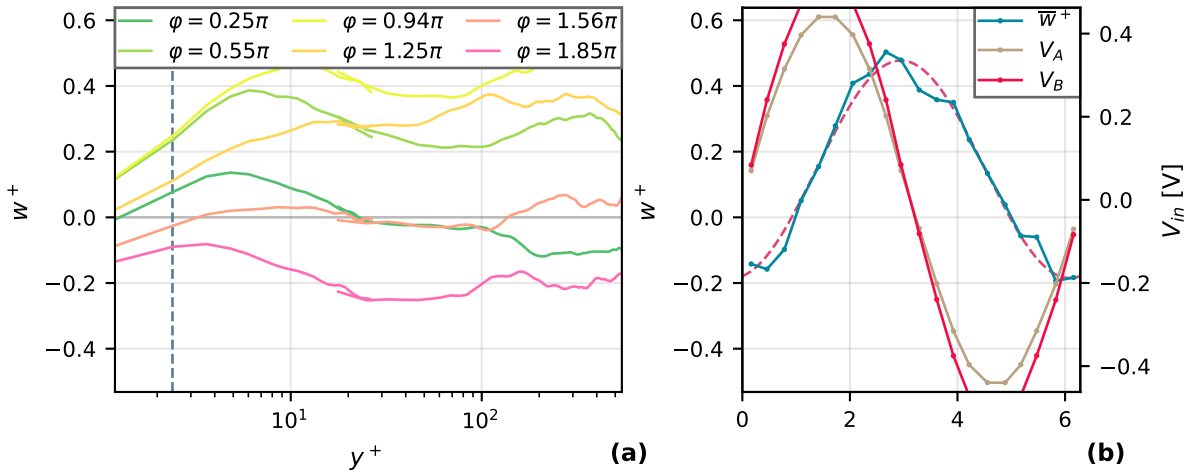
Figure C.39: (a) transverse velocity profiles at various instances of the phase with $Re_\tau = 2990$. (b) The average transverse velocity over the phase. The dashed line marks the sinusoidal fit used to extract $W_m^+ = 0.33$. The voltage signal to the speakers is also shown.

Figure C.40: (a) transverse velocity profiles at various instances of the phase with $Re_\tau = 1282$. (b) The average transverse velocity over the phase. The dashed line marks the sinusoidal fit used to extract $W_m^+ = 1.18$. The voltage signal to the speakers is also shown.
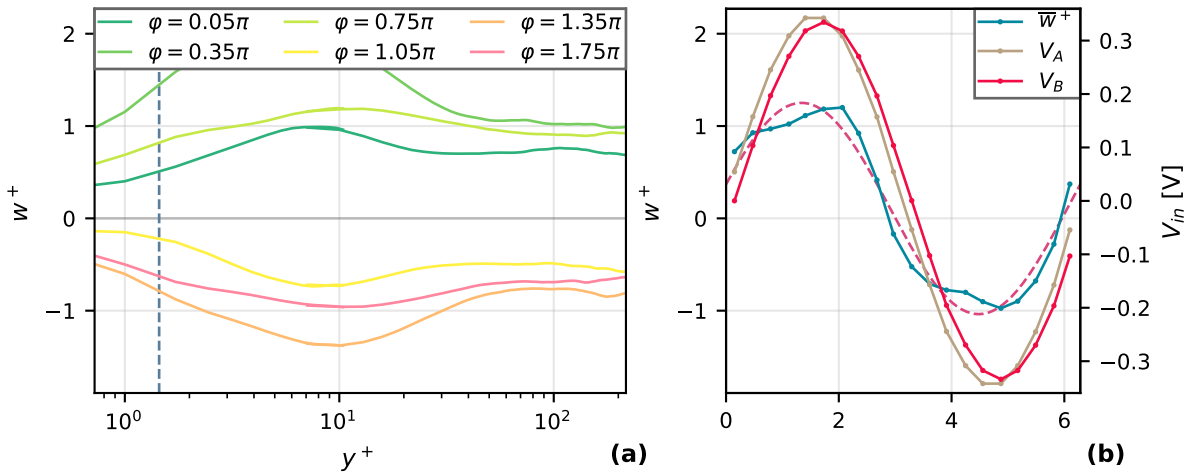

Figure C.41: (a) transverse velocity profiles at various instances of the phase with $Re_\tau = 1618$. (b) The average transverse velocity over the phase. The dashed line marks the sinusoidal fit used to extract $W_m^+ = 0.66$. The voltage signal to the speakers is also shown.
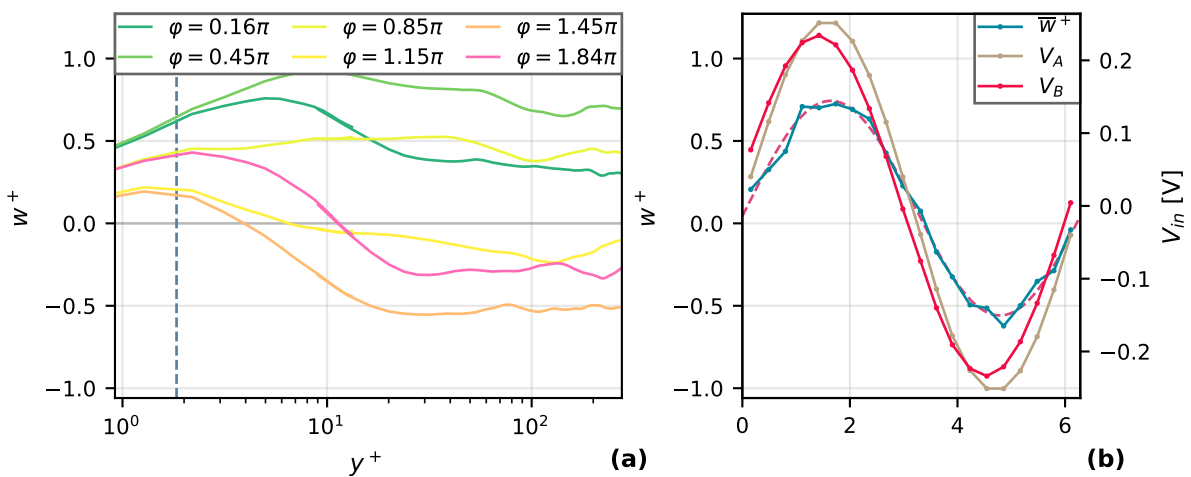
Figure C.42: (a) transverse velocity profiles at various instances of the phase with $Re_\tau = 2009$. (b) The average transverse velocity over the phase. The dashed line marks the sinusoidal fit used to extract $W_m^+ = 0.69$. The voltage signal to the speakers is also shown.

Figure C.43: (a) transverse velocity profiles at various instances of the phase with $Re_\tau = 2268$. (b) The average transverse velocity over the phase. The dashed line marks the sinusoidal fit used to extract $W_m^+ = 0.76$. The voltage signal to the speakers is also shown.
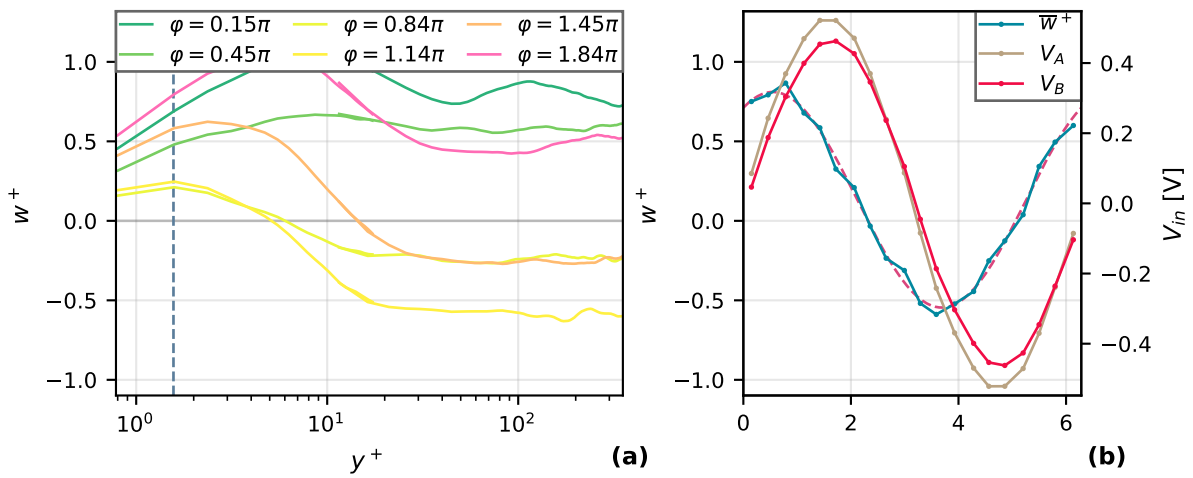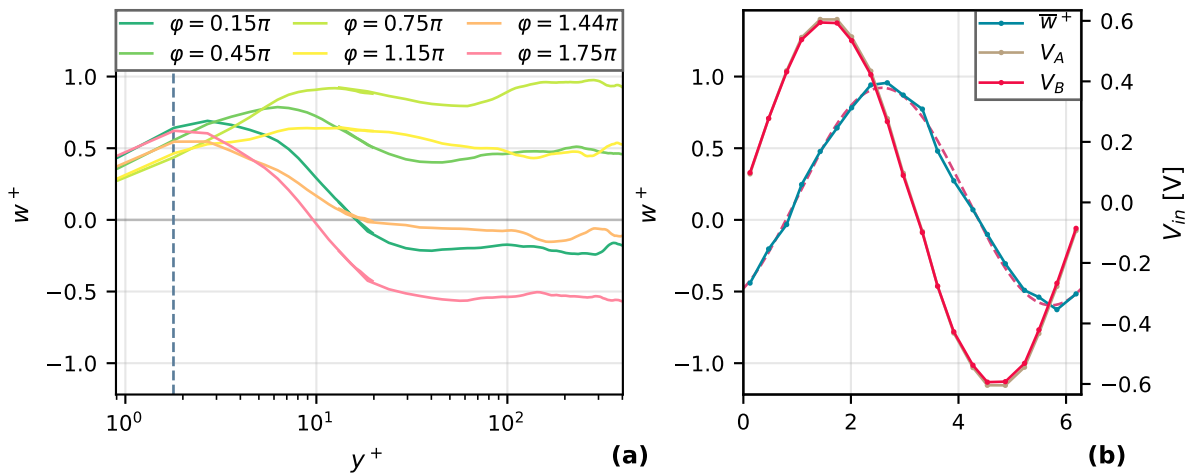
C.3.3. Turbulence statistics

The Reynolds stress tensor component profiles and the contributions to the TKE transport equation are calculated for each measurement and presented in this section. The profiles corresponding to the drag reduction measurements with $T^+ \approx 100$, summarised in Figure 4.5, are shown in Figures C.44, C.45, C.46, C.47, C.48 and C.49. The measurements with $T^+ \approx 120$, summarised in Figure 4.6, are shown in Figures C.50, C.51, C.52 and C.53. Finally the measurements with $T^+ \approx 120$ and $W_m^+ \approx 0.70$, summarised in Figure 4.7, are shown in Figures C.54, C.55, C.56 and C.57.
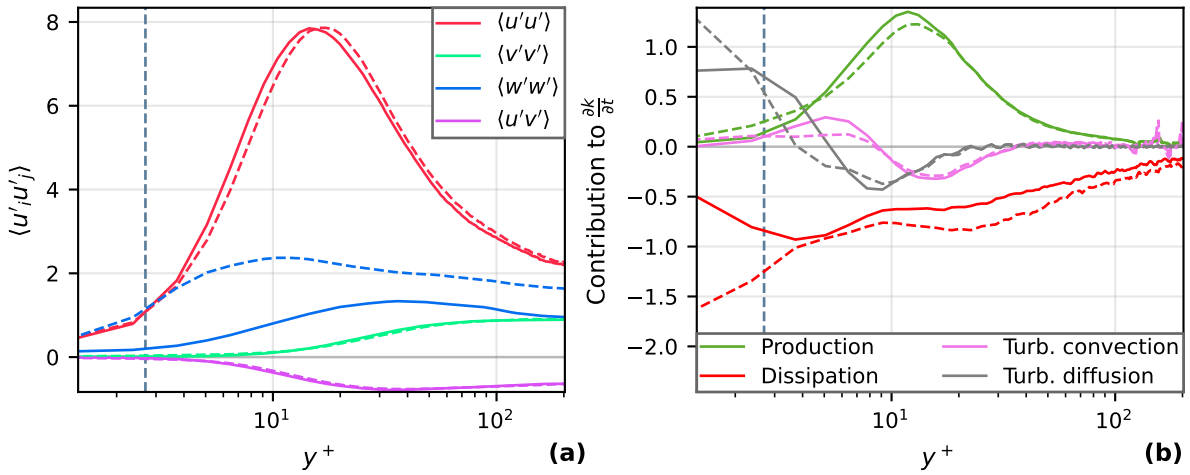
Figure C.44: (a) Reynolds stresses for the measurement with $Re_\tau = 1192$, the solid and dashed lines represent the reference and forced case respectively. (b) Selected contribution to the turbulence kinetic energy budget, the solid and dashed lines represent the reference and forced case respectively.

Figure C.45: (a) Reynolds stresses for the measurement with $Re_\tau = 1469$, the solid and dashed lines represent the reference and forced case respectively. (b) Selected contribution to the turbulence kinetic energy budget, the solid and dashed lines represent the reference and forced case respectively.

Figure C.46: (a) Reynolds stresses for the measurement with $Re_\tau = 1847$, the solid and dashed lines represent the reference and forced case respectively. (b) Selected contribution to the turbulence kinetic energy budget, the solid and dashed lines represent the reference and forced case respectively.
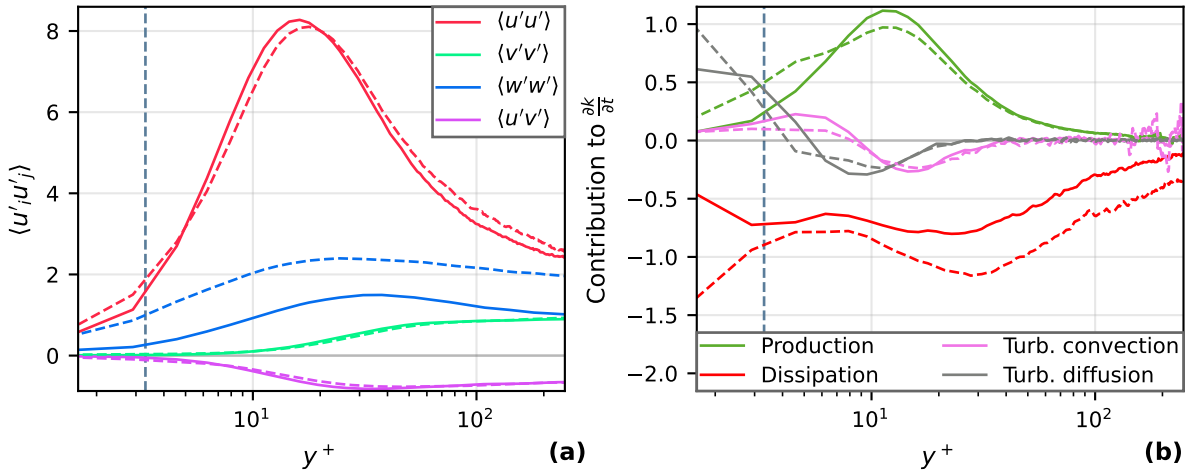
Figure C.47: (a) Reynolds stresses for the measurement with $Re_\tau = 2080$, the solid and dashed lines represent the reference and forced case respectively. (b) Selected contribution to the turbulence kinetic energy budget, the solid and dashed lines represent the reference and forced case respectively.
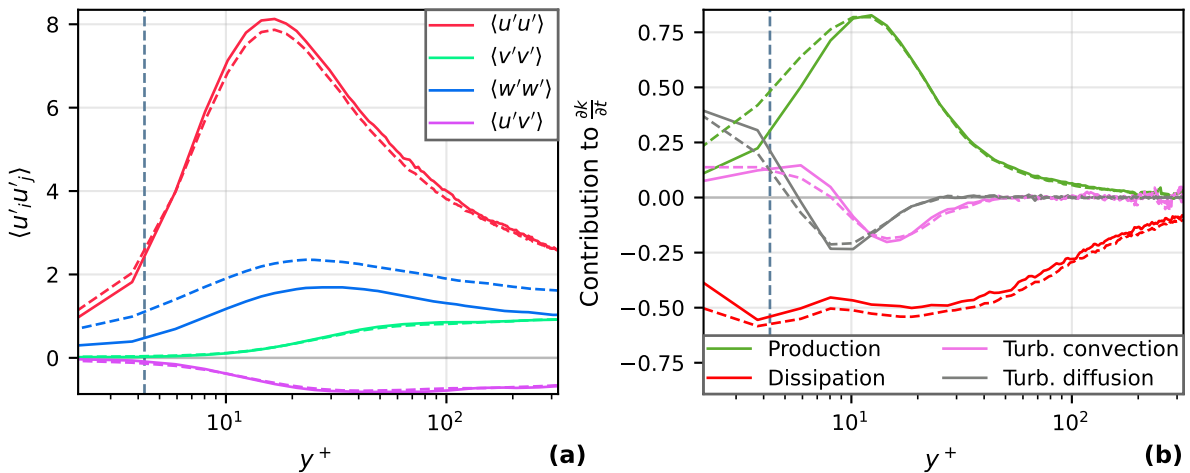

Figure C.48: (a) Reynolds stresses for the measurement with $Re_\tau = 2603$, the solid and dashed lines represent the reference and forced case respectively. (b) Selected contribution to the turbulence kinetic energy budget, the solid and dashed lines represent the reference and forced case respectively.

Figure C.49: (a) Reynolds stresses for the measurement with $Re_\tau = 3023$, the solid and dashed lines represent the reference and forced case respectively. (b) Selected contribution to the turbulence kinetic energy budget, the solid and dashed lines represent the reference and forced case respectively.
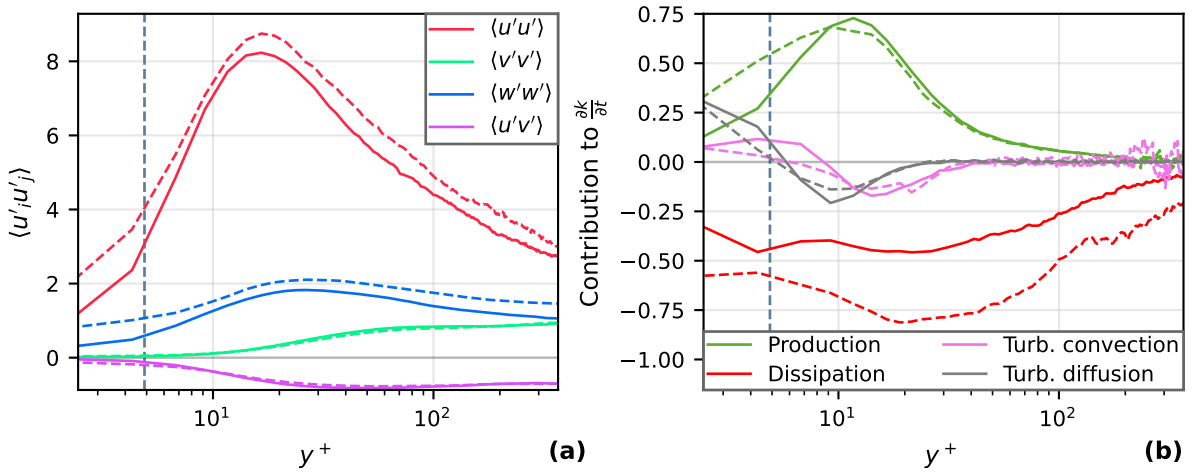
Figure C.50: (a) Reynolds stresses for the measurement with $Re_\tau = 1575$, the solid and dashed lines represent the reference and forced case respectively. (b) Selected contribution to the turbulence kinetic energy budget, the solid and dashed lines represent the reference and forced case respectively.
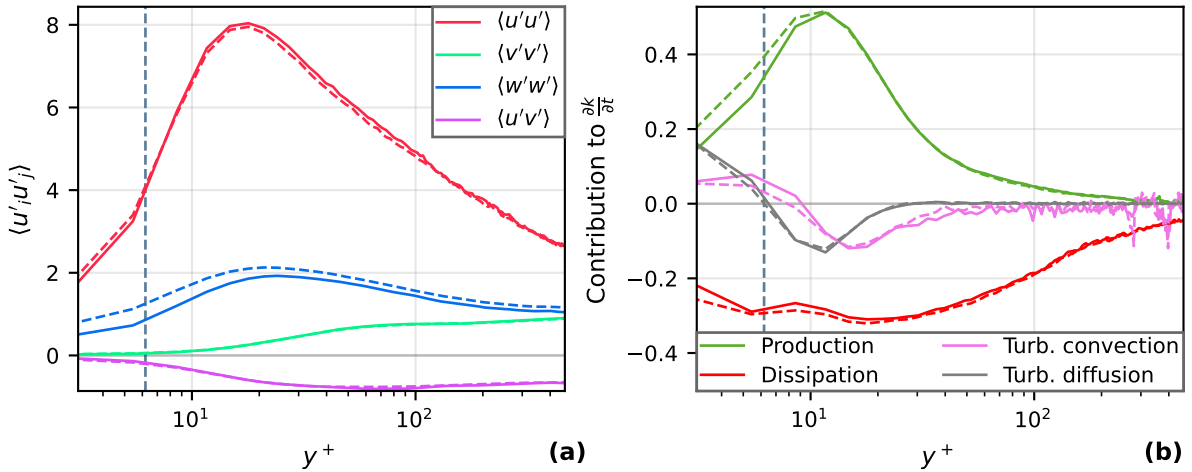

Figure C.51: (a) Reynolds stresses for the measurement with $Re_\tau = 2067$, the solid and dashed lines represent the reference and forced case respectively. (b) Selected contribution to the turbulence kinetic energy budget, the solid and dashed lines represent the reference and forced case respectively.
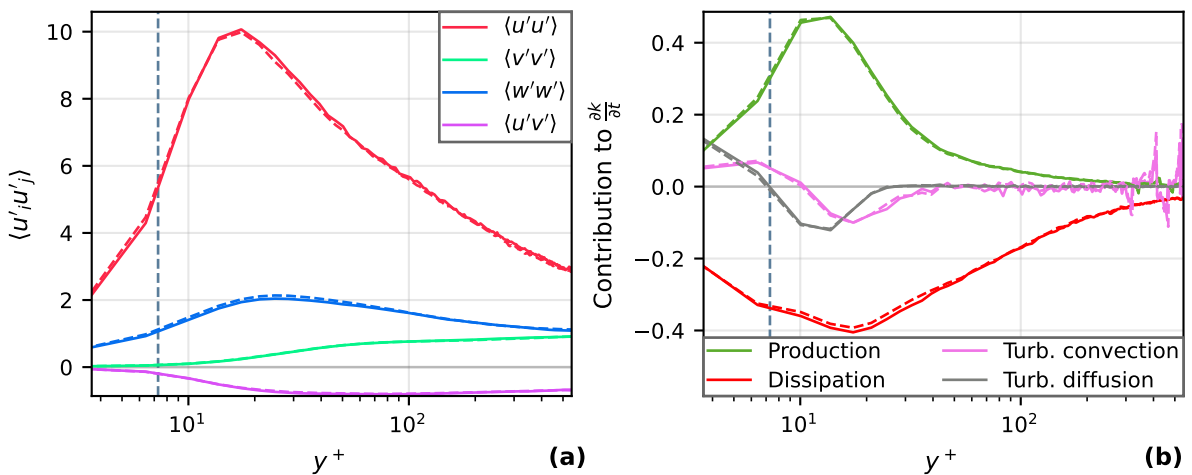

Figure C.52: (a) Reynolds stresses for the measurement with $Re_\tau = 2565$, the solid and dashed lines represent the reference and forced case respectively. (b) Selected contribution to the turbulence kinetic energy budget, the solid and dashed lines represent the reference and forced case respectively.
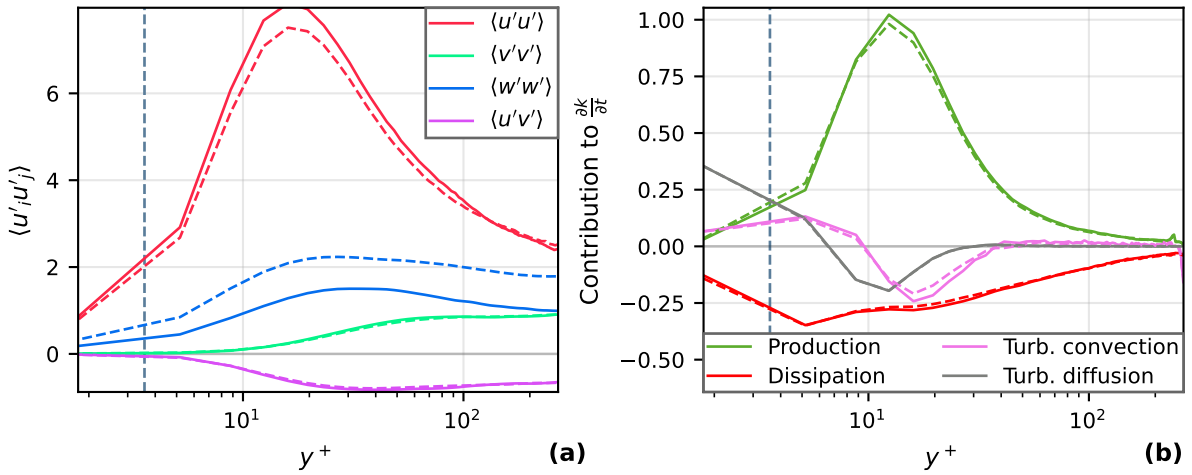
Figure C.53: (a) Reynolds stresses for the measurement with $Re_\tau = 2990$, the solid and dashed lines represent the reference and forced case respectively. (b) Selected contribution to the turbulence kinetic energy budget, the solid and dashed lines represent the reference and forced case respectively.
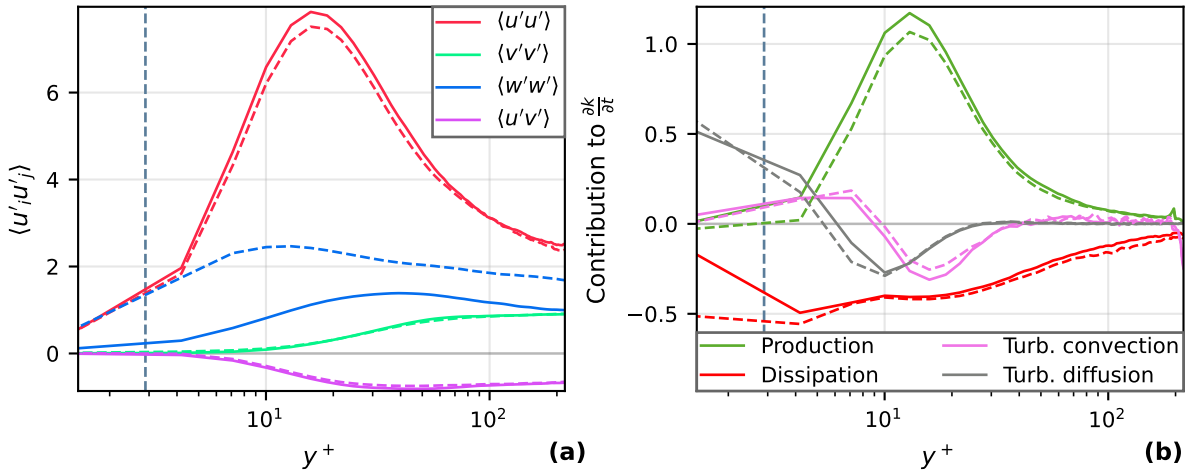
Figure C.54: (a) Reynolds stresses for the measurement with $Re_\tau = 1282$, the solid and dashed lines represent the reference and forced case respectively. (b) Selected contribution to the turbulence kinetic energy budget, the solid and dashed lines represent the reference and forced case respectively.
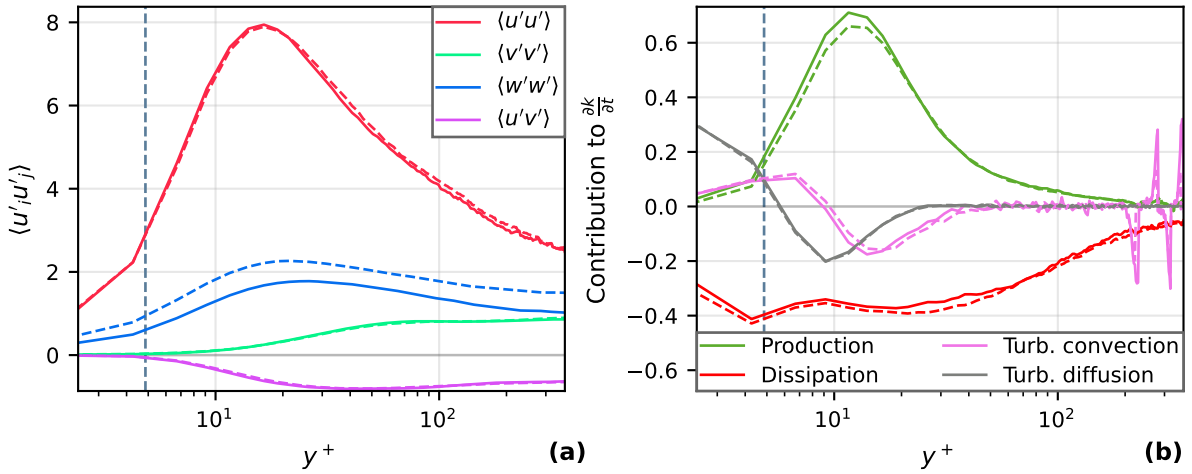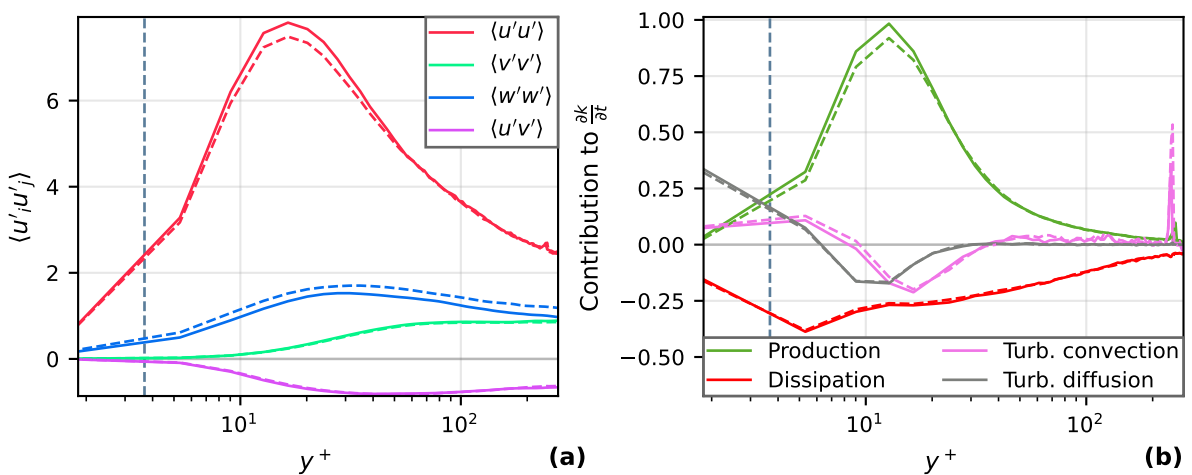

Figure C.55: (a) Reynolds stresses for the measurement with $Re_\tau = 1618$, the solid and dashed lines represent the reference and forced case respectively. (b) Selected contribution to the turbulence kinetic energy budget, the solid and dashed lines represent the reference and forced case respectively.
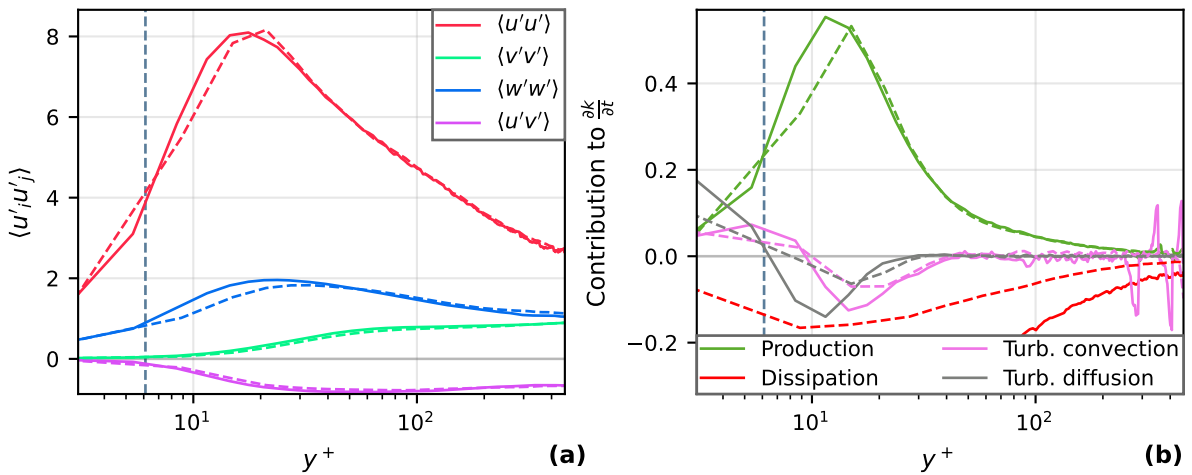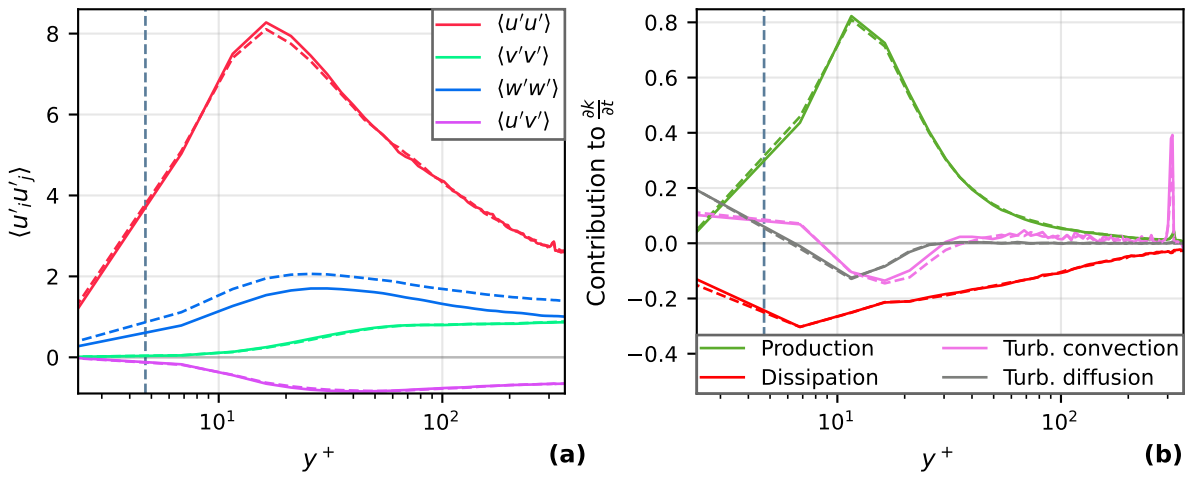
Figure C.56: (a) Reynolds stresses for the measurement with $Re_\tau = 2009$, the solid and dashed lines represent the reference and forced case respectively. (b) Selected contribution to the turbulence kinetic energy budget, the solid and dashed lines represent the reference and forced case respectively.
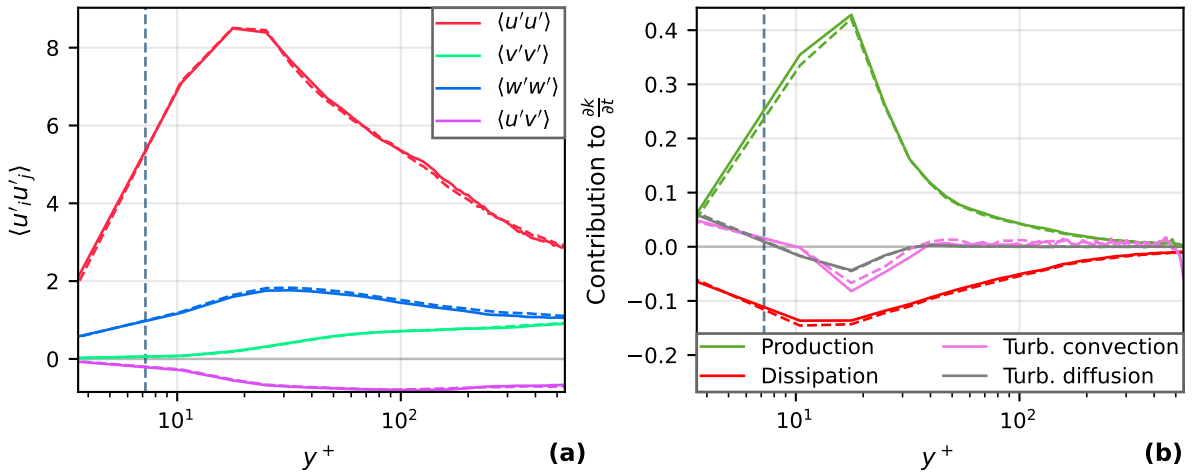

Figure C.57: (a) Reynolds stresses for the measurement with $Re_\tau = 2268$, the solid and dashed lines represent the reference and forced case respectively. (b) Selected contribution to the turbulence kinetic energy budget, the solid and dashed lines represent the reference and forced case respectively.
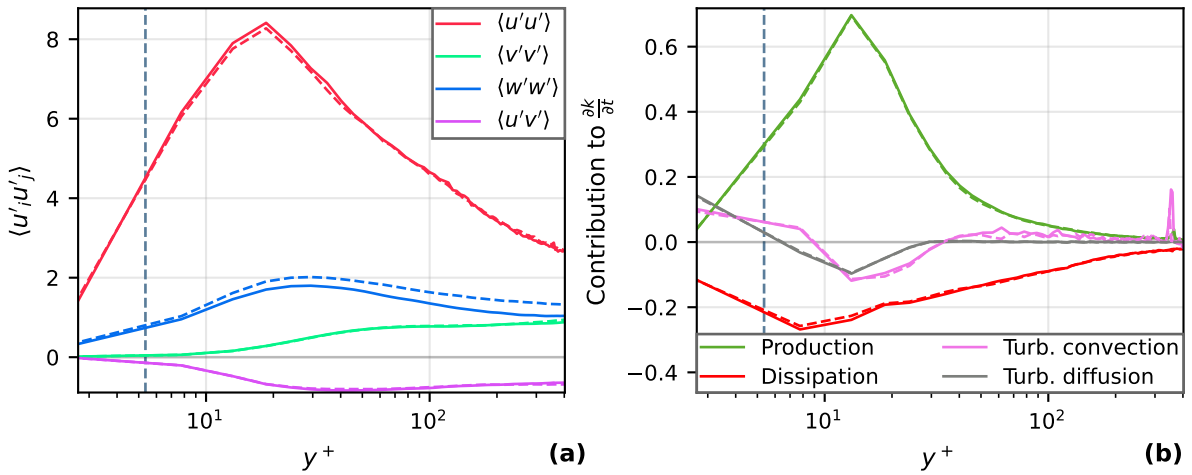
D

Speaker Selection

As the main actuator in the test setup the speaker driver selection needed careful consideration. The selection process was done using the method described in Section 3.1.3. The full list of speakers considered with their manufacturers and price at time of writing is found in Table D.1. Their T/S parameters are found in Table D.2.

Figure D.1 shows the calculated capability of each speaker. At low frequencies the maximum velocity amplitude W_m at the centerline of the test section is limited by the maximum displacement x_{max} of the speaker. This is under the assumption that the moving mass M_{ms} is increased to lower the resonant frequency f_s, taking into account that the efficiency η_0 also decreases. However, available power is not an issue at low frequencies. With increasing frequency each speaker has a cross over point where it start to be limited by the maximum available power P_{max}, this is denoted by the second part of the curve. The selected operating point is marked, as well as the same oscillation parameters at $Re_\tau = 2000$ and $Re_\tau = 3000$.

It was found that most of the selected speakers are capable to achieve the required operating conditions. Therefore the focus was shifted to finding a speaker with the greatest extra margin on its capability. Figure D.2 shows for each speaker the margin to P_{max}, the extra M_{ms} needed to lower the f_s to the selected operating point and the price of the speaker. The B&C 18TBX100 was eventually selected because of the good balance between price and having a sufficient power margin. The downside of this speaker is the relatively high f_s but this was considered of minor importance, as the high power margin enables this and future research to explore a larger part of the parameter space given in Equation 2.9.

Name	Manufacturer	Price [EUR]	
21SW152	B&C Speakers	875	link
21SW115	B&C Speakers	747.78	link
21IPAL	B&C Speakers	1382	link
21DS115	B&C Speakers	769	link
18TBX100	B&C Speakers	286	link
15PLB76	B&C Speakers	241	link
15TBX100	B&C Speakers	315	link
HT-18 v3	Stereo Integrity	200	link
RSS460HO-4	Dayton Audio	559	link
DCS385-4	Dayton Audio	200	link
RSS390HF-4	Dayton Audio	390	link
18SW500	SB Audience	240	link
18SW650	SB Audience	290	link
18SW800	SB Audience	300	link
18SW750	SB Audience	325	link
18SW1000D	SB Audience	370	link

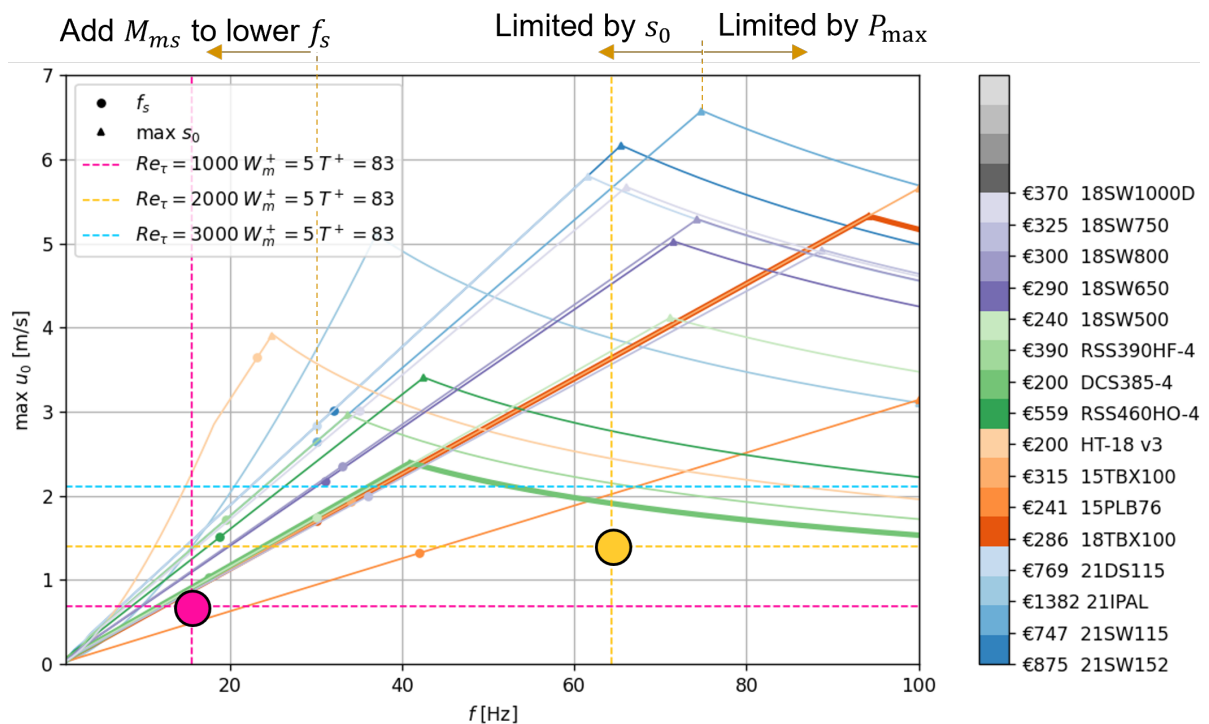**Table D.1:** List of speakers considered in this research, with their manufacturers and price at time of writing.

Figure D.1: Calculated limit of all considered speakers, each speaker can reach any point under their respective curve.

Name	D $[mm]$	P_{nom} $[W]$	P_{max} $[W]$	d_{gap} $[mm]$	x_{max} $[mm]$	Z_{nom} $[\Omega]$	R_e $[\Omega]$	Q_{es}
21SW152	533.4	2000	4000	12	15	4	3.3	0.31
21SW115	530	1700	3400	14	14	8	5.4	0.39
21IPAL	547	2500	5000	18	22	1	0.7	0.22
21DS115	530	1700	3400	14	15	4	2.2	0.2
18TBX100	460	1200	2400	12	9	4	3.7	0.33
15PLB76	380	400	800	11	5	8	5	0.26
15TBX100	380	1000	2000	12	9	4	3.7	0.28
HT-18 v3	457	750	1500	0	25	4	4.2	0.69
RSS460HO-4	457	900	1800	0	12.75	4	3.2	0.35
DCS385-4	381	300	600	0	9.3	4	3.3	0.42
RSS390HF-4	305	500	1000	0	14	4	3	0.5
18SW500	457	500	1000	24	9.21	8	5.7	0.53
18SW650	457	650	1300	22	11.18	8	5	0.44
18SW800	457	800	1600	23	11.33	8	5.1	0.48
18SW750	457	750	1500	20	8.82	8	5.1	0.45
18SW1000D	457	1000	2000	25	13.67	8	5.3	0.49
Name	Q_{ms}	V_{as} $[m^3]$	S_d $[m^2]$	η_0	M_{ms} $[kg]$	Bl $[Tm]$	L_e $[mH]$	f_s $[Hz]$
21SW152	7	0.2	0.168	2.2	0.46	32.5	1.5	32
21SW115	10.9	0.318	0.168	2.2	0.342	30.1	2.1	30
21IPAL	4.9	0.155	0.168	3.2	0.487	19.1	0.5	37
21DS115	11	0.274	0.168	3.4	0.412	28.8	2.4	30
18TBX100	7	0.256	0.121	1.96	0.23	22	1.73	30
15PLB76	5.9	0.164	0.0855	4.5	0.088	22.1	1.3	42
15TBX100	5.73	0.13	0.0855	1.74	0.173	22.13	1.49	34
HT-18 v3	4.11	0.22	0.119	0	0.4341	19.7	4.7	23.1
RSS460HO-4	4.05	0.272	0.1164	0	0.499	23.4	2.24	18.8
DCS385-4	5.27	0.311	0.08501	0	0.273	15.4	2.2	17.5
RSS390HF-4	3.02	0.212	0.08296	0	0.306	15	0.92	19.5
18SW500	19.04	0.3348	0.12692	1.6	0.1952	19.8	1.64	30
18SW650	8.32	0.3043	0.12441	2	0.1897	20.6	1.4	31
18SW800	9.09	0.2581	0.12566	1.86	0.2006	21	1.25	33
18SW750	10.5	0.2069	0.12566	2.03	0.2124	23.3	1.59	36
18SW1000D	10.13	0.1643	0.12566	1.44	0.276	25.8	1.64	35

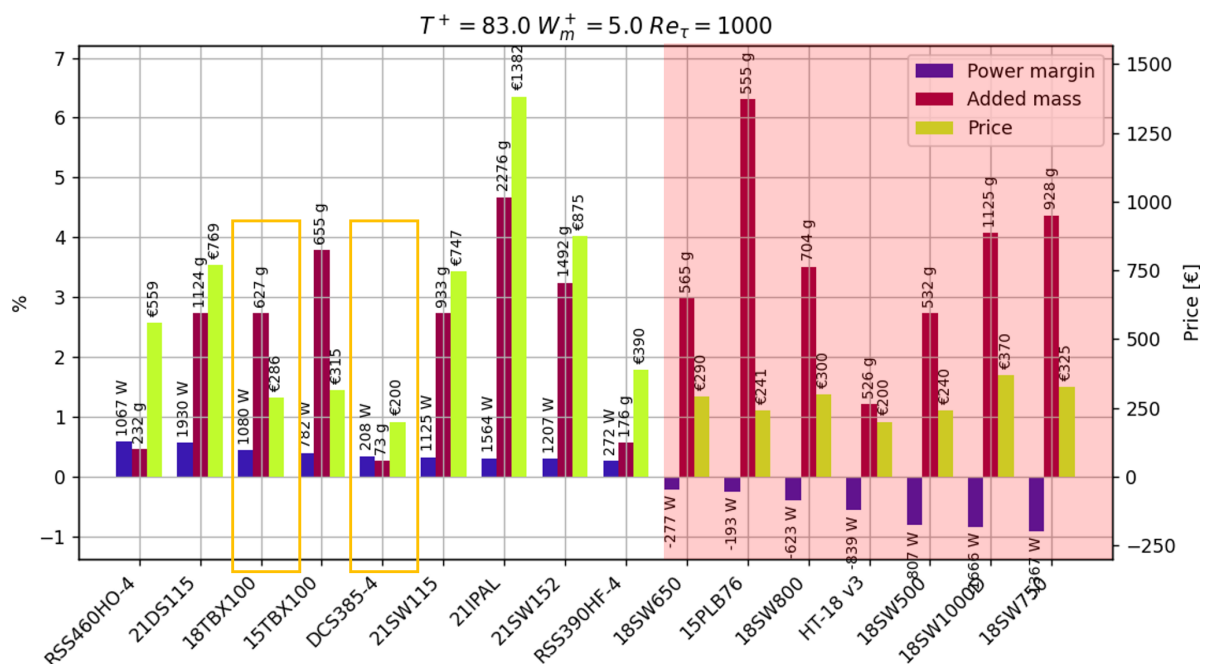**Table D.2:** Thiele/Small Parameters for the speakers listed in Table D.1.

Figure D.2: Capability comparison between all speakers, sorted on the margin in available speaker power P_s at the selected operating point.